

SULFIDE INCLUSIONS IN STEEL

by

LOUIS KIMBALL BIGELOW, Jr.

B.A. Harvard University 1962

B.S. Harvard University 1964

Presented in Partial Fulfillment of the Requirements

for the Degree of

DOCTOR OF SCIENCE

at the

Massachusetts Institute of Technology

1970

Signature of Author  
Department of Metallurgy

Signature of the Professor  
Director of Research

Signature of Chairman of  
Graduate Research  
Committee

Science



# SULFIDE INCLUSIONS IN STEEL

by

LOUIS KIMBALL BIGELOW, Jr.

Submitted to the Department of Metallurgy on February 28, 1970, in partial fulfillment of the requirements for the degree of Doctor of Science.

---

## ABSTRACT

The formation of sulfide inclusions in the Fe-Mn-S system was studied using high purity materials. Modifications of this basic system by controlled additions of oxygen, aluminum, carbon, and silicon were made in order to study the factors causing the various inclusion morphologies observed in commercial alloys. The effect of cooling rate on inclusion morphology was studied over the range of 0.5°C/sec. to greater than 100°C/sec.

New experimental data on the Fe-Mn-S ternary were obtained. The commonly presented phase diagram was shown to be incorrect in one region. Qualitative isothermal sections of the Fe-Mn-S-O quaternary system were derived. These were used to explain the transformation from spherical oxy-sulfides (commonly known as Type I) to rod-like or sheet-like inclusions which have been associated in commercial practice with reduced impact strength. This undesirable transformation results from the addition of a deoxidizer. The rod and sheet inclusions, known jointly as Type II in the literature, have been separately designed Type II R and II S here. Their different modes of formation are explained on the basis of the Fe-Mn-S ternary.

Faceted inclusions associated in the literature with excess additions of aluminum and known as Type III are shown not to form in the pure Fe-Mn-S system, even with very large aluminum additions. The formation of Type III inclusions was found to require the presence of an element in the melt which strongly increases the activity coefficient of sulfur. Two such elements which were studied are carbon and silicon. A new finding of this work is that Type III inclusions do not form as the primary phase, except in highly alloyed, non-commercial specimens. In the range of commercial compositions

Type III inclusions form as a divorced eutectic of MnS and Fe, generally late in solidification and with a faceted morphology because the liquid is still dilute with respect to sulfur. The particles are frequently entrapped by advancing dendrite arms.

Increasing cooling rates decrease the size of all inclusions observed (except for primary slag inclusions). The higher cooling rates also favor formation of rod-like Type II R eutectic inclusions over Type III, in alloys low in carbon and silicon. In alloys of higher carbon and silicon, high cooling rates favor a newly observed type of faceted eutectic inclusion designated herein Type II F.

Small test bars were machined from some of the ingots and fractured in order to study the behavior of the inclusions during deformation. Scanning electron microscope pictures of inclusions in the fracture surface are presented. Considerable solidification shrinkage occurs when Type I inclusions freeze, causing at least localized separation from the matrix. Pictures taken in the necked region of the test bars show formation of voids around the inclusions, fracture of some of the inclusions, and propagation of micro-cracks from one inclusion to another.

Thesis Supervisor: Merton C. Flemings  
Title: Professor of Metallurgy

## TABLE OF CONTENTS

<u>Chapter Number</u>		<u>Page Number</u>
	ABSTRACT	2
	LIST OF FIGURES	7
	INDEX OF TABLES - GLOSSARY OF TERMS	11
	ACKNOWLEDGEMENTS	12
I	INTRODUCTION	13
II	LITERATURE SURVEY	15
	A. Experimental Properties and Morphology Research	16
	B. Phase Diagram and Solubility Data	28
	C. Processing and Solid State Reactions	33
III	BASIC PHASE DIAGRAMS AND THEIR MODIFICATION BY ALLOYING ADDITIONS	38
	A. The Fe-Mn-S System	38
	B. The Fe-S-O System	47
	C. The Fe-Mn-S-O System	47
	D. The Fe-S-C System	52
	E. The Fe-Al-S System	53
	F. The Fe-Si-S System	56
	G. Complex Systems Involving Modification of the Fe-Mn-S System by Si, Al, and C.	57
IV	SOLIDIFICATION MODELS	59
	A. Introduction	59
	B. The Fe-Mn-S System	59
	C. The Fe-Mn-S-O System	76
	D. Models for Sulfide Formation in Systems Containing Carbon and Silicon	78
	1. Phase Relation Effects	78
	2. Growth Factors	91
V	EXPERIMENTAL PROCEDURE	93
	A. General Procedure	93
	B. Experimental Setup	93
	C. Materials Used	94
	D. Experimental Procedure	95
	E. Chemical Analysis	96
	F. Fractography	97



<u>Chapter Number</u>		<u>Page Number</u>
VI	EXPERIMENTAL RESULTS	98
	A. Introduction	98
	B. Chemical Effects	101
	1. The Fe-Mn-S-(Aluminum Deoxidized) System	101
	2. The Fe-Mn-S-(Vacuum-carbon Deoxidized) System	105
	3. The Fe-Mn-S-O System	109
	4. The Fe-Mn-S-C System	112
	5. The Fe-Mn-S-Si System	114
	6. The Fe-Mn-S-Al System	119
	7. The Fe-Mn-S-Si-C System	120
	C. Thermal Effects	120
	1. Introduction	120
	2. Effect of Cooling Rate on Sulfide Morphology	122
	3. Effect of Undercooling of Metal Phase on Sulfide Morphology	126
	4. Effect of Temperature of Addition of Manganese to the Melt	130
	5. The Effect of Solid-State Trans- formations	131
VII	INTERPRETATION OF EXPERIMENTAL RESULTS. EVALUATION OF SOLIDIFICATION MODELS. FRACTURE.	133
	A. Introduction	133
	B. The Systems Fe-Mn-S, Fe-Mn-S-O, and Fe-Mn-S-Al	133
	1. The Fe-Mn-S System	133
	2. The Fe-Mn-S-O System	146
	3. The Fe-Mn-S-Al System	150
	4. Additional Observations on the Fe-Mn-S, Fe-Mn-S-O, and Fe-Mn-S-Al Systems	151
	C. Type III Inclusions	152
	D. Fracture Research	166
	1. Effect of Morphology on Physical Pro- perties	166
	2. Inclusion Shrinkage	170
	3. Eutectic Formation	178
	4. Deformation and Fracture of Inclusions. Crack Propagation	178
VIII	DISCUSSION	181
	A. Inclusion Formation	181
	1. Type I Inclusions	181
	2. Type II R Inclusions	183
	3. Type II S Inclusions	185

<u>Chapter Numbers</u>		<u>Page Number</u>
	4. Type II F Inclusions	187
	5. Type III Inclusions	188
	6. Type D Inclusions	192
	B. Fracture	194
IX	SUMMARY AND CONCLUSIONS	195
X	SUGGESTIONS FOR FUTURE WORK	200
	BIBLIOGRAPHY	201
	APPENDICES	
	A. Experiments on Fe-Mn-S Ternary	207
	B. The Fe-Mn-O-S System	212
	C. Lot Analysis of Ferrovac-E Iron	228
	BIOGRAPHICAL NOTE	229

## LIST OF FIGURES

<u>Figure Number</u>		<u>Page Number</u>
1	Qualitative projection of Fe-Mn-S phase diagram according to Wentrup <sup>25</sup> , Schurmann <sup>27</sup> , and others. Arrows point in the direction of falling temperature.	40
2	Qualitative projection of Fe-Mn-S phase diagram according to Vogel <sup>26</sup> .	41
3	Actual Fe-Mn-S ternary.	46
4	Appearance of Fe-Mn-S ternary, qualitatively represented. Temperatures in °C.	48
5	Qualitative isopleth of the Fe-Mn-S-O quaternary at 1500°C and 1% Mn. The isopleth is a plane of constant composition intersecting the isothermal quaternary tetrahedron.	49
6	Qualitative isopleth of the Fe-Mn-S-O quaternary at 1490°C and 1% Mn.	50
7	Qualitative isopleth of Fe-Mn-O-S quaternary system at 1475°C and 1% Mn.	51
8	Solidification path of a typical high-manganese steel. Miscibility gap not shown.	61
9	Solidification path if initial composition is between the miscibility gap and the eutectic valley.	64
10	Course of solidification in an alloy of initial composition in the miscibility gap.	67
11	Solidification paths of three specimens with initial compositions 1, 2 and 3.	70
12	Course of solidification of an alloy with initial composition on the eutectic, according to Wentrup's phase diagram.	71

<u>Figure Number</u>		<u>Page Number</u>
13	Four-phase reaction plane, isolating the phases which are in equilibrium in Figure 12.	73
14	Derived from Schurmann <sup>27</sup> .	81
15	Pseudo-binary cuts between Fe and MnS for pure system (dashed lines), and for carbon saturated system.	84
16	Photomicrographs of sulfide inclusions found in the aluminum deoxidized Fe-Mn-S system.	103
17	Photomicrographs of sulfide inclusions found in the aluminum deoxidized Fe-Mn-S system.	104
18	Photomicrographs of sulfide inclusions found in the aluminum deoxidized Fe-Mn-S system.	106
19	Photomicrographs of sulfide inclusions found in the vacuum-carbon deoxidized Fe-Mn-S system.	107
20	Photomicrographs of sulfide inclusions found in the vacuum-carbon deoxidized Fe-Mn-S system.	108
21	Photomicrographs of inclusions from the Fe-Mn-O-S system.	110
22	Photomicrographs of inclusions from the Fe-Mn-O-S system.	111
23	Photomicrographs of inclusions in the Fe-Mn-S-C system.	113
24	Photomicrographs of inclusions from the Fe-Mn-S-Si system.	116
25	Photomicrographs of inclusions from the Fe-Mn-S-Si system.	117
26	Photomicrographs of inclusions from the Fe-Mn-S-Si system, and from the Fe-Mn-S-Al system.	118
27	Photomicrographs of specimens in the Fe-Mn-S-Si-C system.	121

<u>Figure Number</u>		<u>Page Number</u>
28	Photomicrographs of Type I inclusions showing effect of cooling rate.	124
29	Photomicrographs of Type D inclusions showing effect of cooling rate.	125
30	Photomicrographs showing the effect of cooling rate on Type II R and II S inclusions.	127
31	Photomicrographs showing effect of cooling rate on Type III inclusions.	128
32	Schematic illustration of the formation of Type II R rod eutectic.	136
33	Structures observed on the Fe-FeS side of the Fe-Mn-S diagram.	148
34	Photomicrographs of Alloy 25-1 showing the relative positions of sulfide inclusions and the iron dendrites. Light etch with 1% Nital.	157
35	Formation modes of Type I, D, III and II F inclusions in high carbon or high silicon melt.	158
36	Model for solidification in high carbon or high silicon alloys where primary MnS dendrites form.	160
37	Type III inclusions found in alloys of the compositions used as examples in Table 1.	164
38	Alloy 28-2 showing angular-irregular rod Type II R inclusions coexisting.	165
39	Type III inclusions in Alloy 25-2.	167
40	Scanning electron microscope pictures of Type I inclusions in fracture surface of Alloys 5-5 and 5-6.	171
41	Scanning electron microscope pictures of fracture surface of Alloy 5-25, containing Type II R inclusions.	172

<u>Figure Number</u>		<u>Page Number</u>
42	Inclusion morphology in Alloy 15-1.	173
43	Scanning electron microscope pictures of inclusion morphology in fracture surface of Alloy 28-2.	174
44	Scanning electron microscope pictures of polished surface of Alloy 5-6.	175
45	Fracture mode caused by Type II R inclusions in Alloy 5-25.	176
A-1	Liquidus isotherms and eutectic plotted from data in Table A-1.	209
B-1	Fe-Mn-O-S phase diagram for 1600°C.	213
B-2	Qualitative isopleth of the Fe-Mn-S system at 0.2% Mn.	218
B-3	Qualitative isopleth of the Fe-Mn-S system at 1% Mn.	219
B-4	Qualitative isopleth through the Fe-Mn-S system.	221
B-5	Qualitative isopleth through the Fe-Mn-O system at a level of 0.2% Mn.	223
B-6	Qualitative isopleth of the Fe-Mn-O ternary at .1% Mn.	224

## INDEX OF TABLES

<u>Table Number</u>		<u>Page Number</u>
1	Predicted fraction solid at which solid MnS precipitates	86
2	Compositions and inclusion types in Fe-Mn-S- (Al. deoxidized) systems	102
3	Compositions and inclusion types in Fe-Mn-S- (Vacuum-carbon deoxidized) system	109
4	Compositions and inclusion types in the Fe-Mn- O-S system	112
5	Compositions in the Fe-Mn-S-C system	112
6	Compositions and inclusion types in the Fe-Mn-S-Si system	114
7	Compositions and inclusion types in the Fe-Mn-S-Al system	119
8	Compositions and inclusion types in the Fe-Mn-S-Si-C system	120
9	Mechanical properties of test bar specimens	169
A-1	Liquidus temperatures as a function of composition	211
C-1	Lot analysis of Ferrovac-E iron	228

## GLOSSARY OF TERMS

- Type I inclusions - globular sulfides or oxy-sulfides:  
examples, Figures 16d, 21, 22c.
- Type II R inclusions - rod-like sulfides in eutectic  
colonies: examples, Figures 19d, 30a and b.
- Type II S inclusions - irregular interdendritic or inter-  
granular sheets consisting primarily of FeS:  
examples, Figures 20a, 30d.
- Type II F inclusions - groups of sulfide platelets and  
rods which appear to be crystallographically  
related: examples, Figures 23c and 26b.
- Type D inclusions - MnS dendrites: examples, Figures  
16c, 20b and c.

## ACKNOWLEDGEMENTS

The author wishes to express his sincere appreciation to Professor Merton C. Flemings for his encouragement and guidance throughout the course of this work.

Thanks are also due to Dr. Shri Singh for his help in preparing some of the test bars and for taking some of the scanning electron microscope pictures. His comments and discussions on fracture behavior in these specimens are greatly appreciated.

The advice and help of Ed Backman and Richard Berry in performing some of the experiments is also sincerely appreciated.

Special gratitude is also due to my wife, Helen, for typing the thesis, for help in assembling the figures, and for her encouragement throughout.



## I. INTRODUCTION

The formation of sulfide inclusions in steel has been a subject of concern to steelmakers because of the effect of sulfide morphology on impact properties. Certain types cause a drastic reduction in impact strength. Unfortunately these types are produced by steps which are taken to prevent another undesirable metal flaw, microporosity and blowholes. These latter flaws are produced by the formation of CO gas bubbles in commercial heats containing carbon. In order to prevent them the melt must be deoxidized prior to pouring. When a strong and effective deoxidizer such as aluminum was used, however, it was found that a transformation occurred in the sulfide inclusion morphology, from desirable spherical inclusions to rows of rods or sheets with a simultaneous reduction in impact strength. Sims and Dahle<sup>5</sup> called the spherical inclusions Type I, and the deoxidized version causing reduced properties, Type II. An angular morphology associated with excess additions of aluminum and a partial recovery of ductility was designated Type III by Sims. These basic classifications have persisted in the literature, and are used here in a somewhat modified form.

Considerable research has been conducted in an attempt to understand the reasons for the transformations discussed above, with the ultimate goal of being able to control sulfide morphology to improve properties. Progress has been

made in understanding some of the factors which control sulfide morphology. However, most of the research has been performed on complicated alloy systems where isolation and control of all the variables is very difficult.

The present research attempts to isolate the variables by starting with the simplest system, the Fe-Mn-S ternary. When sulfide formation in this system is understood, controlled amounts of additional elements found in commercial alloys are added and the effect observed. Vacuum-induction melting is used to eliminate contamination from atmospheric oxygen. Effects of cooling rate and quench temperature are monitored and controlled. Materials used are of the highest purity commercially available. An understanding of sulfide formation in steel is developed in this way.

## II. LITERATURE SURVEY

A very large number of references have appeared in the literature dealing with the problem of sulfide inclusions in steel. These are best considered by separating them into several categories based on the particular aspect of the problem on which they concentrate.

### A. Experimental Properties and Morphology Research

The first group of references are those that concentrate on the effects of composition, foundry practice, deoxidizer, and cooling rate on inclusion morphology and mechanical properties. These references are concerned primarily with as-cast structures.

A summary of the appearance of many types of inclusions (not just sulfides) on a polished section is given by Kiessling and Lange.<sup>1</sup>

Among the first systematic studies of sulfide inclusions and their effects were those presented by Sims and Lilliequist<sup>2</sup>, and by Benedicks and Lofquist<sup>3</sup>. They observed, among other findings, that sulfides tend to precipitate at grain boundaries or in interdendritic fillings. Sims gave evidence substantiating an earlier report of Comstock<sup>4</sup> describing a chain type of sulfide which was produced by aluminum additions and resulted in low ductility.

Sims and Dahle<sup>5</sup> performed experiments on a large number of heats to determine the effect of aluminum on the properties of medium carbon cast steels. Tensile strength, yield strength, elongation, reduction of area, and Izod impact strength were measured as a function of composition and deoxidizing practice. They found that the ductility of sulfur bearing steels decreased when aluminum was added, then passed through a minimum and began to increase again, although not to the undeoxidized values. The sulfur levels investigated were in the range 0.02-0.06%, and aluminum additions varied up to 0.25%. Ductility decreased with increasing sulfur levels. The addition of aluminum at higher sulfur contents produced a sharper and deeper decline in ductility than at lower contents, as well as a faster recovery of ductility when the minimum was passed. Sims and Dahle found that although the overall sulfur level was important, the morphology and distribution also had a strong effect. For example, a steel containing 0.05% S and 0.025% Al might have, depending somewhat on the other elements present, a lower value of Izod impact strength than an otherwise identical one with 0.06% S but deoxidized with sufficient aluminum (0.06%) to exceed the ductility minimum. Sims and Dahle associated the change in ductility with changes in sulfide morphology and distribution which were apparently caused by the addition of aluminum. Similar

effects were also observed with other deoxidizers such as titanium and zirconium. The sulfide inclusions associated with low aluminum additions and high ductility were observed to be globular silicates and sulfides of a wide range of sizes and an apparently random dispersion. Sims designated these Type I inclusions. When critical amounts of aluminum were added, generally in the 0.015-0.025% Al range, a eutectic type of sulfide appeared which was distributed in the primary grain boundaries. The silicates had disappeared and were replaced by isolated clusters of alumina. These eutectic, or chain-like sulfides associated with low ductility and the disappearance of silicates were called Type II by Sims. When more aluminum was added a recovery of ductility occurred concurrently with another change in morphology. The silicates did not reappear, but the sulfides became larger, angular, and were apparently duplex in nature. They still appeared to occur in the grain boundaries, according to Sims. Alumina clusters were less often seen than when Type II inclusions are present. Sims concluded that this was because some of the aluminum was present in the inclusions as  $Al_2S_3$ . At 0.04% S and 0.25% Al, the inclusions became dark and round. This new irregular inclusion morphology was designated as Type III. The improvement in ductility was attributed to the fact that Type III

inclusions were larger and further apart and did not form continuous zones of weakness.

Sims and Dahle attributed the changes in morphology to changes in solubility of the sulfides in the melt which governs the stage at which they will precipitate. Segregation of sulfur during freezing until the eutectic composition is reached was said by Sims to be responsible for the formation of sulfide films at the grain boundaries and interstices of primary dendrite branches. When sufficient oxygen is present, an iron manganese silicate liquid containing sulfur can form fairly early in the process of solidification and appears as relatively large globular sulfides. Sims believed that the solubility of MnS in liquid steel is strongly dependent upon the composition. He said that sulfur solubility is increased by lowering the oxygen content of the melt. The effect of aluminum is to lower the oxygen level, thus enabling the sulfur to remain in solution longer and finally to precipitate in narrow segregation zones as a eutectic. Sims concluded that addition of excess aluminum caused the formation of mixed sulfides which precipitate earlier in solidification because of their reduced solubility, forming larger and more widely spaced duplex inclusions. Some of Sims' photomicrographs show rod-like MnS eutectic as well as the duplex  $\text{Al}_2\text{S}_3$  - FeS inclusions which he calls Type III. Types II

and III were found to coexist in some alloys.

Sims reported a similar ability of other strong deoxidizers to form Type II inclusions. He also mentioned a paper by Urban and Chipman<sup>6</sup> which describes sulfides similar to Type III.

Gagnebin<sup>7</sup> reported on research conducted simultaneously with Sims'. He came to similar conclusions about the formation of Type II inclusions and their effect on ductility. He proposed that a strong sulfide forming element, such as calcium, in the presence of sufficient oxygen should be able to form dispersed sulfides in the melt which would remain dispersed when aluminum is added to deoxidize.

Crafts, Egan, and Forger<sup>8</sup> were among the first to consider the relationship of the appropriate phase diagram to the observed sulfide morphology. They studied, on a qualitative basis, the expected effects of various alloying additions on the Fe-Mn-S phase diagram and described the morphologies they expected to result.

Sims, Saller, and Boulger<sup>9,10</sup> later reported the results of additional experiments on deoxidation of steel and the resulting morphologies. They reported that the transition between Types II and III is far less sharp than the I to II transition. They mentioned that the formation of Type III is apparently not a deoxidation phenomena.

Boron, magnesium, titanium, zirconium, and aluminum were

among the deoxidizers studied which were able to effect the Type I to Type II transition. Aluminum contents of about 0.015% were sufficient to give Type III except in steels with very low silicon or carbon. Another finding was that excess zirconium could also produce Type III morphology, but titanium and the other deoxidizers could not. However, they now felt that earlier explanations of Type III based on the formation of duplex sulfides with the deoxidizer were not adequate in view of the fact that Type III were not obtainable in low carbon or low silicon steels. They proposed instead a model in which Type III inclusions were the result of surface tension pulling the inclusions into the line of intersection between three grains of the metal. If the surface tension of the included sulfide liquid is low it will tend to spread out between the grains resulting in the sheet-like Type II morphology. This implied that excess aluminum or zirconium increases the surface tension of the liquid. Sims proposed that more research be done to determine the conditions under which this might be a valid explanation. In a later report, Sims<sup>11</sup> discussed the surface tension concept further. He summarized the effects of various deoxidizers, including mischmetal, and stated that Types I and III inclusions cannot be found together.

Crafts and Hilty<sup>12</sup> expanded their earlier considerations of the importance of phase diagram modifications to



among the deoxidizers studied which were able to effect the Type I to Type II transition. Aluminum contents of about 0.015% were sufficient to give Type III except in steels with very low silicon or carbon. Another finding was that excess zirconium could also produce Type III morphology, but titanium and the other deoxidizers could not. However, they now felt that earlier explanations of Type III based on the formation of duplex sulfides with the deoxidizer were not adequate in view of the fact that Type III were not obtainable in low carbon or low silicon steels. They proposed instead a model in which Type III inclusions were the result of surface tension pulling the inclusions into the line of intersection between three grains of the metal. If the surface tension of the included sulfide liquid is low it will tend to spread out between the grains resulting in the sheet-like Type II morphology. This implied that excess aluminum or zirconium increases the surface tension of the liquid. Sims proposed that more research be done to determine the conditions under which this might be a valid explanation. In a later report, Sims<sup>11</sup> discussed the surface tension concept further. He summarized the effects of various deoxidizers, including mischmetal, and stated that Types I and III inclusions cannot be found together.

Crafts and Hilty<sup>12</sup> expanded their earlier considerations of the importance of phase diagram modifications to

include more quantitative data. They recognized the importance of the oxygen to sulfur ratios in determining morphology. They also discussed the displacement of the metal-sulfide eutectic to the metal corner by manganese and the effect of initial oxygen content.

Sims' 1959 Howe Memorial Lecture<sup>13</sup> on the "Non-metallic Constituents of Steel" includes a discussion of sulfides. In this paper he shows Type III inclusions which are decidedly more angular than those appearing in earlier reports. He gives data showing that the free energy of formation of  $\text{Al}_2\text{S}_3$  is substantially less than that of  $\text{MnS}$ . The fact that the melting point of  $\text{Al}_2\text{S}_3$  is only about  $1100^\circ\text{C}$  implies to Sims that it is probably not a constituent of this version of Type III inclusions. He takes their crystalline form as evidence that these inclusions precipitated as solids, or at least before the matrix steel. The inclusions are apparently located in intercrystalline locations and form where "the mother liquid breaks up into isolated pools, usually where three or more grains meet." Sims also discusses the effects of inclusions on the properties of steel. Sulfides have a marked effect on ductility, while oxides appear to have an important influence on fatigue failures. Additions of sulfur in the range of 0.10 to 0.25% markedly improve the machineability of a steel, although a law of diminishing returns sets in at higher levels.

Some research indicates that large inclusions which deform only small amounts during hot rolling have particularly beneficial effects. Aluminum additions appear to reduce machinability through their effect on sulfide morphology. The adverse effects of sulfides on hot shortness and hot tearing of steel are also mentioned by Sims.

A report by Sims and Briggs<sup>14</sup> considers further the effects of various deoxidizers on inclusion morphology. Deoxidation curves for the various elements are included. Differences between theoretical oxygen levels which should result from additions of deoxidizers and the actual experimental values are pointed out. Sharply angular Type III inclusions are again reported. The only effective desulfurizers are the rare earth elements such as cerium and lanthanum. However, these result in an undesirable type of inclusion. Sims and Briggs conclude that the only practical and economical way to lower the sulfur level of a steel is by treatment with a basic slag.

Results of another research project were reported by Lichy, Duderstadt, and Samways.<sup>15</sup> They studied the effects of aluminum, mischmetal, zirconium, and titanium on as-cast and rolled structures. Their research concentrates primarily on the effect of appropriate zirconium additions in producing beneficial oval-shaped sulfides in rolled steel. They also consider the modification of the Fe-Mn-S

phase diagram by carbon and the variation of sulfur solubility with temperature in carbon-saturated iron.

Research in Japan on sulfur in steel has concentrated primarily on macrosegregation. Typical of such work is that of Hirai, Araki, Matsukuma, and Kojima<sup>16</sup>. They found more Type II inclusions in the rapidly cooled areas of the ingot than in slowly cooled areas.

Dahl, Hengstenberg, and Düren<sup>17</sup> based their analysis of sulfide morphology on modifications of the basic Fe-Mn-S diagram by various alloying elements. They considered one basic level of sulfur content, 0.20%, which is commonly found in free-machining steels. The manganese content was held constant at about 1%. They then varied the carbon, silicon, aluminum, and phosphorous levels in such a way as to separate their individual and joint effects on morphology. Their most significant results and interpretations are summarized in the next few paragraphs.

Type I sulfides lie in the positive segregation zones, although some mixed types may be found within the dendrites. Electron microprobe analysis found these inclusions to consist of manganese, sulfur, and small amounts of dissolved oxygen along with some manganese and aluminum-bearing oxides. Dahl found that increasing carbon contents shifted the Type I-Type II transition to lower levels of aluminum addition. The higher carbon heats were found to have lower

oxygen contents at a given aluminum level, so that a relation appeared to exist between the oxygen level and the transition from Type I to Type II. Dahl found that below 0.011% oxygen only Type II sulfides exist, while between 0.01 and 0.02% oxygen an intermediate type occurs, and above 0.02% only Type I is present.

Dahl, Hengstenberg and Düren found that even very large additions of aluminum could not produce Type III inclusions unless threshold levels of carbon and/or silicon were also present. These inclusions were found to be distributed throughout both the positive and negative segregation regions. Type III inclusions were found in specimens containing sufficient carbon and silicon even in the absence of aluminum additions. Higher phosphorous contents were found to promote the formation of Type III inclusions. Most of Dahl's experiments were carried out at phosphorous levels between 0.01% and 0.04%. Addition of 0.26% P caused a transformation from Type II to dendritic sulfide morphology.

Electron microprobe analysis of several Type III inclusions showed them to consist entirely of manganese and sulfur, except that a small dark particle consisting of alumina was frequently present. Silicon was not detected in the inclusions, even though the matrix contained large amounts of it.

Dahl attempted to explain the various morphologies on the basis of phase diagram modifications. He presented a qualitative Fe-MnS-MnO phase diagram and by means of a quasi-binary cut through it showed how liquid droplets of a slag phase could precipitate in the enriched liquid between primary iron dendrite arms. In deoxidized melts the Fe-Mn-S ternary becomes relevant. A quasi-binary cut across the ternary from Fe to MnS is appropriate for systems containing moderate amounts of manganese, and is used by Dahl to demonstrate how the eutectic Type II inclusions could form. Dahl concluded that Type III inclusions form as the primary phase. He based this on their angular form, random location, and on the absence in them of elements contained in the matrix. Type III inclusions may be found at the same levels of manganese and sulfur as Type II, but only at higher levels of silicon and carbon. Dahl attributed the Type II-Type III transition to the effects of these elements. Silicon and carbon are known to have a strong influence in lowering the melting point of iron and they also reduce the solubility of sulfur in the melt. These effects combine to make Mn-S the primary phase provided that the oxygen level is kept low by aluminum additions or by high levels of carbon and silicon. Dahl shows qualitatively how the quasi-binary cut across the Fe-Mn-S system may be modified by additions of silicon and carbon in such a way that

a manganese and sulfur concentration which fell in the primary iron region in the pure system now falls on the other side of the eutectic in the primary MnS region. Under such conditions the sulfides could grow as angular solids in the liquid iron melt, would be able to reject alloying additions such as silicon, and could assume random locations relative to the iron grains which solidify at a lower temperature.

Beech, Hands, and Mohla<sup>18</sup> developed a technique for melting small amounts of metals in such a way as to avoid contamination by a crucible. They formed water-cooled copper tubes into the shape of a boat to hold the metal, and melted the specimen by means of r.f. heating. By passing pure hydrogen over the melt they were able to obtain oxygen levels of 5 p.p.m. The resulting sulfide structures do not appear different from those seen elsewhere at slightly higher oxygen levels.

Mohla and Beech<sup>19</sup> used their melting apparatus to investigate the factors which determine sulfide morphology. They varied the oxygen content in a series of melts containing 1% manganese and 0.05, 0.10 and 0.20% sulfur. They found when the oxygen level is reduced that Type I inclusions transform to Type II, confirming the results and conclusions of earlier researchers. Their data shows that the Type I-Type II transition occurs at higher oxygen levels as

the sulfur content is increased. Another conclusion is that at very low oxygen levels Type III inclusions do not form in the pure Fe-Mn-S system. Additions of carbon, boron, or phosphorous produced Type III inclusions even in the absence of aluminum. Addition of 2.5% silicon with or without aluminum did not produce Type III inclusions, although silicon was capable of moving the boundary between Types II and III to lower levels of manganese and sulfur. Mohla and Beech compared their results at a high cooling rate using the copper boat with other results in the literature, and concluded that cooling rate as well as composition is an important variable. Using high aluminum contents ( $> 0.10\%$ ) they found that the higher the cooling rate the greater the aluminum content needed for the formation of Type III inclusions. Mohla and Beech also present a series of micrographs showing morphologies which may be present at various stages in the growth of Type III inclusions. They are in substantial agreement with Dahl, et al, on the phase diagram interpretation of morphology.

Mohla and Beech<sup>20</sup> in an additional publication considered the effect of cooling rate more thoroughly. They studied alloys containing combinations of silicon, carbon, and aluminum, and varied the compositions and cooling rates in order to separate their effects. Cooling rates ranged from less than  $1^{\circ}\text{C}/\text{second}$  to about  $340^{\circ}\text{C}/\text{second}$ . Sulfur



and deoxidizing elements on sulfide morphology in AISI 4330 low alloy steel. The appearance of Types I, II, and III inclusions is explained on the basis of the Fe-Mn-S ternary.

Summary: There is general agreement in the literature that oxygen is responsible for the transition from Type I to Type II inclusions. Several attempts have been made to explain this in terms of phase diagrams, but even qualitative knowledge of the necessary phase relations is limited. Considerable confusion still exists as to the true factors leading to formation of Type III inclusions, although Dahl, Hengstenberg and Düren<sup>17</sup> have presented the most convincing explanation so far, based on phase diagram modifications caused by carbon and silicon. Mohla and Beech<sup>20</sup> discovered that cooling rate had an effect on the Type II to Type III transition. In summary, however, there is a lack of a systematic study of sulfide formation in steel which considers a range of compositions in the simple Fe-Mn-S system, using high purity materials, and then expands this fundamental study by controlled additions of commercial alloying elements.

#### B. Phase Diagram and Solubility Data

A brief overall review of the literature concerning relevant phase diagrams and solubility data is presented in this section. The actual phase diagrams which are

important for the present research are discussed in considerable detail in Chapter III.

One of the most important investigations of the equilibrium relations among iron, manganese, and sulfur was carried out by Meyer and Schulte<sup>23</sup>. They studied the equilibrium coefficients for the various reactions between components in the slag and the bath at 1600°C. They noticed that carbon and silicon have a strong influence on the equilibrium coefficients.

Joseph and Holbrook<sup>62</sup> presented a series of curves for the solubility of sulfur in iron as a function of temperature and manganese content.

Körber and Oelsen<sup>24</sup> also researched this system, and presented data which substantially confirmed the position of the projection of the miscibility gap at 1600°C onto the base of the Fe-Mn-S ternary phase diagram implied by Meyer's work. They added new data points and tie lines. The influence of alloying elements such as silicon, carbon, and phosphorous is mentioned. Several graphs relating sulfur and manganese contents in the melt to their contents in the slag are presented.

Wentrup<sup>25</sup> presented qualitative phase diagrams of many systems of interest in studying the formation of inclusions in steel. Among these are Fe-FeO-FeS, Fe-Mn-O, Fe-Mn-S, FeO-MnO-FeS-MnS, Fe-Si-O, Fe-Mn-Si-O, Fe-Al-O, and Fe-Si-Mn-Al-O. Photomicrographs of the inclusion structures found at various compositions in many of these systems are included.

About the same time Vogel and Hotop<sup>26</sup> were investigating the Fe-Mn-S system in more quantitative detail. They concluded from their results that the eutectic does not intersect the miscibility gap on the iron-sulfur side, although it may approach it quite closely.

Schurmann<sup>27</sup> considered the desulfurization of cast iron by manganese. Some of his data are summarized in graphs showing the decrease in manganese sulfide solubility with falling temperature in high carbon alloys. He disputes Vogel's conclusion that the eutectic does not intersect the miscibility gap, but admits that he does not have conclusive evidence to disprove Vogel's version.

Hilty and Crafts<sup>28</sup> examined the Fe-S-O system in some detail and generated a phase diagram from their data. A few tie lines across the miscibility gap are included. They later considered the modification of this system by manganese, and experimentally verified their qualitative conclusions for a system containing 1% manganese in solid metal

which was equilibrated at 1475°C against melts containing various proportions of oxygen and sulfur<sup>29</sup>.

Schurmann and von Hertwig<sup>30</sup> also studied the Fe-O-S system, using an experimental technique virtually identical to that used by Hilty and Crafts. Their results differ somewhat from Hilty's, especially as concerns the oxygen content at the plait point of the miscibility gap. The results of Hilty and Crafts may be more reliable because of the method of oxygen analysis used<sup>31</sup>.

Chao, Smith, and Van Vlack<sup>32</sup> found in studying the MnS-MnO binary that there is considerably less solid solubility at each end of the phase diagram than had previously been assumed. They found that solid solubility at the eutectic was less than 2% on both sides of the diagram. The MnS-MnO eutectic was determined to be at 1232°C.

The system Fe-FeS-FeSi was investigated by Vogel, Uschinski, and Theune<sup>33</sup>. More recently, Schurmann and von Hertwig<sup>34</sup> considered the related quaternary system, Fe-FeO-FeS-SiO<sub>2</sub>.

Research relevant to the modification of the basic phase diagrams by common alloying additions was conducted by Norro and Lundquist<sup>35</sup> and by Vogel and Hillen<sup>36</sup>. The former investigated the miscibility gap in the Fe-S-C system saturated with carbon between 1300 and 2000°C. The latter pair researched the Fe-Al-S system. They found that a

miscibility gap extends across the phase diagram from the Al-Al<sub>2</sub>S<sub>3</sub> side, much as in the case of Fe-Mn-S. An important difference is that Al<sub>2</sub>S<sub>3</sub> melts at a lower temperature than iron, whereas MnS melts at a higher temperature.

Morris and Buehl<sup>37</sup> investigated the effect of carbon on the activity of sulfur in liquid iron. Graphs are presented which compare the effect of carbon with that of silicon. The latter element was investigated in an earlier paper<sup>38</sup>. The paper on the effect of carbon is discussed by Richardson, Sherman and Darken in a seminar with Morris and Buehl<sup>39</sup>.

Hilty and Crafts<sup>40,41</sup> found that silicon and manganese in combination are a much stronger deoxidizer than separately. Hilty<sup>42</sup> found that between 0.005% S and 0.10% S the solubility of oxygen is slightly reduced by increasing sulfur, but that at higher sulfur levels the trend is reversed. Sulfur contents above 1% greatly increase the oxygen solubility in pure iron. Plots of oxygen versus sulfur with various amounts of Al, Mn, and Si in the melt are also presented by Hilty. Earlier research by Hilty and Crafts<sup>43</sup> showed that the actual level of oxygen in a melt deoxidized with aluminum is far higher than would be predicted on the basis of the equilibrium constant.

The chemical potential for the formation of MnS in iron is plotted by Brown<sup>44</sup> for various manganese and sulfur

concentrations and temperatures. Brown also considers the effect of the distribution coefficient and microsegregation on the precipitation of inclusions and the proportion of FeS versus MnS which results.

The thermodynamic properties of sulfur in molten iron-sulfur alloys were investigated by Sherman, Elvander, and Chipman<sup>45</sup>. The equilibrium constant for the reaction between dissolved manganese, and an oxide slag was investigated by Chipman, Gero, and Winkler<sup>46</sup> and found to be higher than reported by Körber and Oelsen<sup>47</sup>. Further thermodynamic data on the activity of sulfur in iron, and on the effects of alloying elements, was presented in another paper by Sherman and Chipman<sup>69</sup>.

### C. Processing and Solid State Reactions

In order to understand the observed microstructure and relate it to conditions existing at the start of freezing it is necessary to know what solid state reactions may occur to modify the original structure. A brief review of work related to the iron-sulfur-oxygen system follows.

The solubility of oxygen in  $\alpha$ -iron between 700°C and 900°C was studied by Seybolt<sup>48</sup>. Precipitation of iron oxide from solid solution as the temperature was lowered in this region was also investigated by Seybolt<sup>49</sup>. The precipitate consisted of barely resolvable spheroidal particles. No

metallographic evidence was found of grain boundary oxide film. Seybolt therefore showed that oxygen diffusion in  $\alpha$ -iron does not occur primarily by an intergranular mechanism even at these temperatures.

Turkdogan, Ignatowicz and Pearson<sup>50</sup> investigated the solid solubility of sulfur in iron and iron-manganese alloys, expanding on earlier work by Rosenqvist and Dunicz<sup>70</sup>. Their phase diagram of the iron-rich corner shows that the solubility of sulfur is progressively lower in  $\delta$ ,  $\gamma$ , and  $\alpha$ -iron. Their experiments also demonstrated the effect of manganese in reducing the solubility of sulfur, and produced some experimental values. They conclude that sulfur contents above 0.01% can cause hot-shortness in pure iron, but that the addition of about 0.40% Mn will bind almost all the sulfur as solid MnS and prevent the problem.

The behavior of sulfur in solid iron was described in a series of papers by Ainslie and Seybolt<sup>51</sup>, Ainslie, Hoffman, and Seybolt<sup>52</sup>, and Ainslie, Phillips, and Turnbull<sup>53</sup>. Sulfur solubility and volume diffusion in pure iron and in 3.25% silicon-iron was researched in the first of these. The sulfur-manganese solubility product in the silicon alloy was also determined. Grain boundary diffusion of sulfur is apparently quite rapid in the  $\alpha$ -iron range. The second two papers use this high diffusion rate to explain sulfur segregation at  $\alpha$ -iron grain boundaries formed by

exposure to  $H_2S$ . A high dislocation density at the grain boundaries is associated with the sulfur segregation.

Kiessling and Westman<sup>64</sup> found that  $MnS$  is capable of dissolving considerable amounts of chromium and other transition metals in substitutional solid solution. They found that these elements increased the microhardness of the inclusions over the value determined for pure  $MnS$ .

Brammer and Honeycombe<sup>54</sup> used electron microscope and microprobe techniques to investigate the grain boundaries. They attributed embrittlement to the segregation of sulfur to the grain boundaries during cooling through the  $\alpha$ -iron range. They report a number of interesting sulfide structures in  $\alpha$  and  $\gamma$  grain boundaries. An important conclusion is that manganese sulfide, even when preferentially precipitated at grain boundaries, does not have a deleterious effect on impact strength. However, their oxygen level was in the range of Dahl's<sup>17</sup> Type I compositions, so their results may not contradict those of Dahl<sup>17</sup> and Sims<sup>5</sup>.

In studying the effect of sulfur on the recrystallization behavior of iron, Baird and Arrowsmith<sup>55</sup> also observed the precipitation of sulfur on grain boundary dislocation substructures. Electron microscope pictures of some of these subgrain structures are included.



In researching the machineability of rephosphorized screw steel, Paliwoda<sup>56</sup> found that although high sulfur levels improved machineability, sulfide shape was even more important, with oval sulfides providing the best results. Yeo<sup>57,58</sup> found that deoxidation reduced machineability because it caused the formation of eutectic sulfide stringers instead of larger more desirable oval types. He used a phase diagram explanation of morphology. He also asserted that the oxygen in Type I inclusions has a hardening effect which helps them to remain oval during rolling. His primary composition for investigation was 0.1C-1.0Mn-0.25S, deoxidized with silicon, boron, aluminum, or a carbon boil.

Van Vlack has emphasized the importance of interfacial energy on sulfide morphology in several papers. Dihedral angles were measured to obtain the interfacial energy of  $\gamma$ -iron and a sulfide liquid held for several hours at 1000-1200°C<sup>59</sup>. This was found to be about 0.5 of the  $\gamma$ -iron/ $\gamma$ -iron value, and less than this above 1200°C. When oxygen was present the value did not drop below 0.5, resulting in less spreading between the grains. A later paper<sup>60</sup> studied this phenomenon more thoroughly. Keh and Van Vlack found at 1300°C that the sulfide spreads to form a complete network as the dihedral angle approaches zero. Silicon has little effect on this behavior. However, aluminum, oxygen, and manganese all transfer the temperature necessary for

network formation to a higher temperature. Keh and Van Vlack note that the sulfide tends to form in grain corners in order to reduce the surface energy. Coarsening of spherical sulfides within the grains was also observed. A later paper by Van Vlack, Riegger, Warrick and Dahl<sup>61</sup> discusses the effect of silicon and oxygen in fluxing sulfide inclusions at hot-rolling temperatures. Manganese is shown to have a beneficial effect in creating a more spherical morphology.

### III. BASIC PHASE DIAGRAMS AND THEIR MODIFICATION BY ALLOYING ADDITIONS

The phase diagrams which are relevant to the formation of sulfide inclusions in steel will be discussed in this section. A few of the ternary systems have been investigated quantitatively in some detail. Others are known only qualitatively except for a few data points. Information on quaternary and pseudo-ternary diagrams is almost entirely qualitative.

#### A. The Fe-Mn-S System

This ternary phase diagram is of fundamental importance in understanding sulfide inclusion formation in deoxidized steels. The modification of this basic system by alloying elements can have a large effect on the expected equilibrium structures.

Reference has already been made to the major research on the Fe-Mn-S ternary.<sup>23,24,25,26,27,29,62</sup> These researchers generally agree on the basic features of the system. The phase diagram is dominated by a large liquid miscibility gap which extends from the Mn-MnS side almost entirely across to the iron corner and then drops in temperature to a critical point near the Fe-FeS side of the diagram. The Fe-FeS and Fe-Mn binaries have been extensively studied and are well known in their general outlines.<sup>65</sup>

In some areas they are known in considerable detail, e.g. Turkdogan's<sup>50</sup> study of the iron corner. The Fe-FeS system is a simple eutectic. Iron and manganese, on the other hand, have unlimited solubility in the liquid and solid states. The Mn-MnS binary is not well established but can be deduced from the known melting points of the components and their low mutual solubility in either the liquid or solid state. Vogel's<sup>26</sup> research indicates that a miscibility gap extends from about 0.3% S to 33.5% S. Vogel also presents a binary diagram of the FeS-MnS system based on his own research and that of Shibata<sup>66</sup>. FeS and MnS form a eutectic near the FeS corner. The phase diagram indicates that manganese sulfide will dissolve considerable FeS, but solid iron sulfide can contain only about 7% Mn.

Whereas there is substantial agreement on the general outline of the phase diagram there is disagreement in the literature on some of the details. The commonly presented versions of the Fe-Mn-S ternary<sup>15,19,20,27,29</sup> have the features proposed by Wentrup<sup>25</sup>. Vogel<sup>26</sup> is apparently the only one to question the relative positions of the three-phase liquidus equilibrium lines presented by Wentrup. Qualitative sketches of the projection of these lines on the base plane are shown in Figure 1 (Wentrup) and Figure 2 (Vogel).

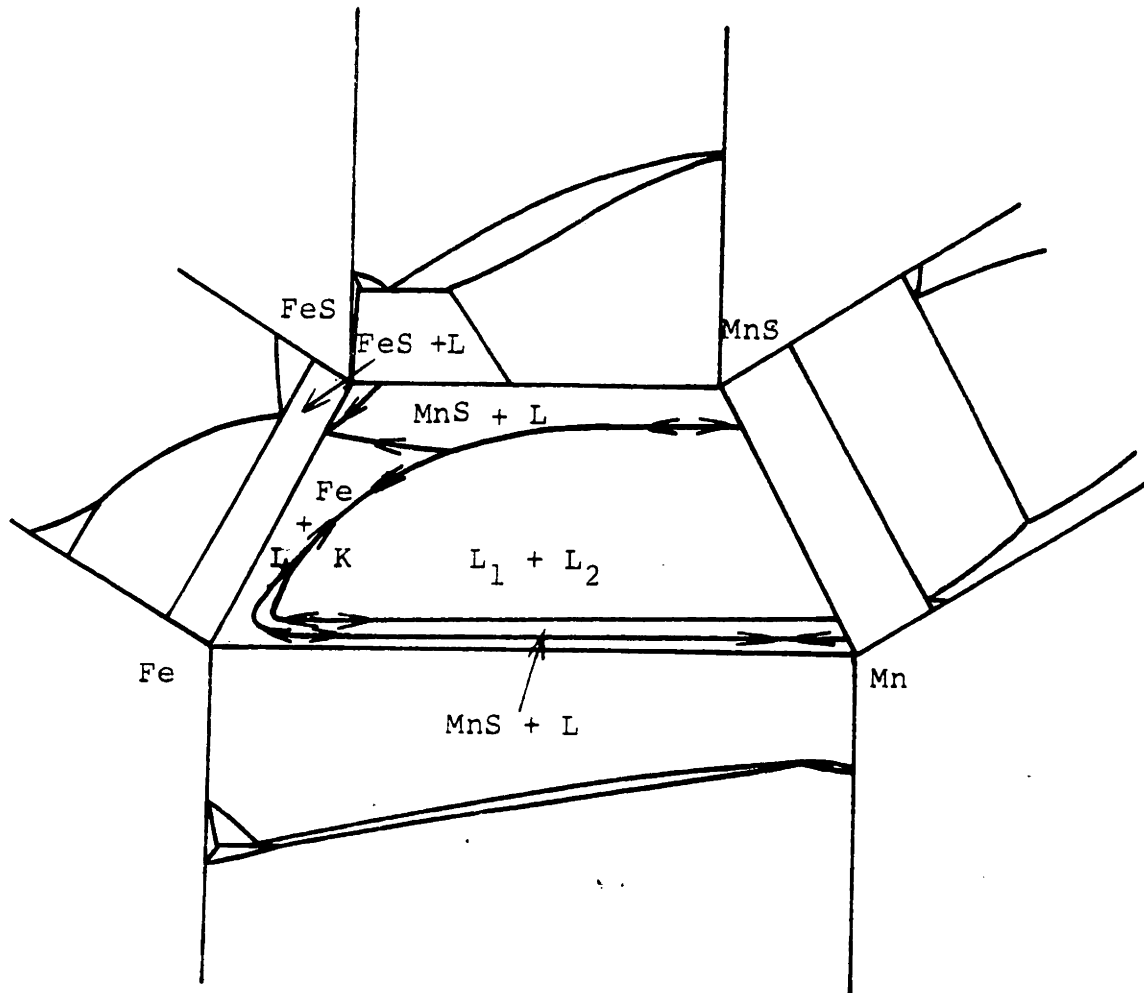


Figure 1: Qualitative projection of Fe-Mn-S phase diagram according to Wentrup<sup>25</sup>, Schurmann<sup>27</sup>, and others. Arrows point in the direction of falling temperature.

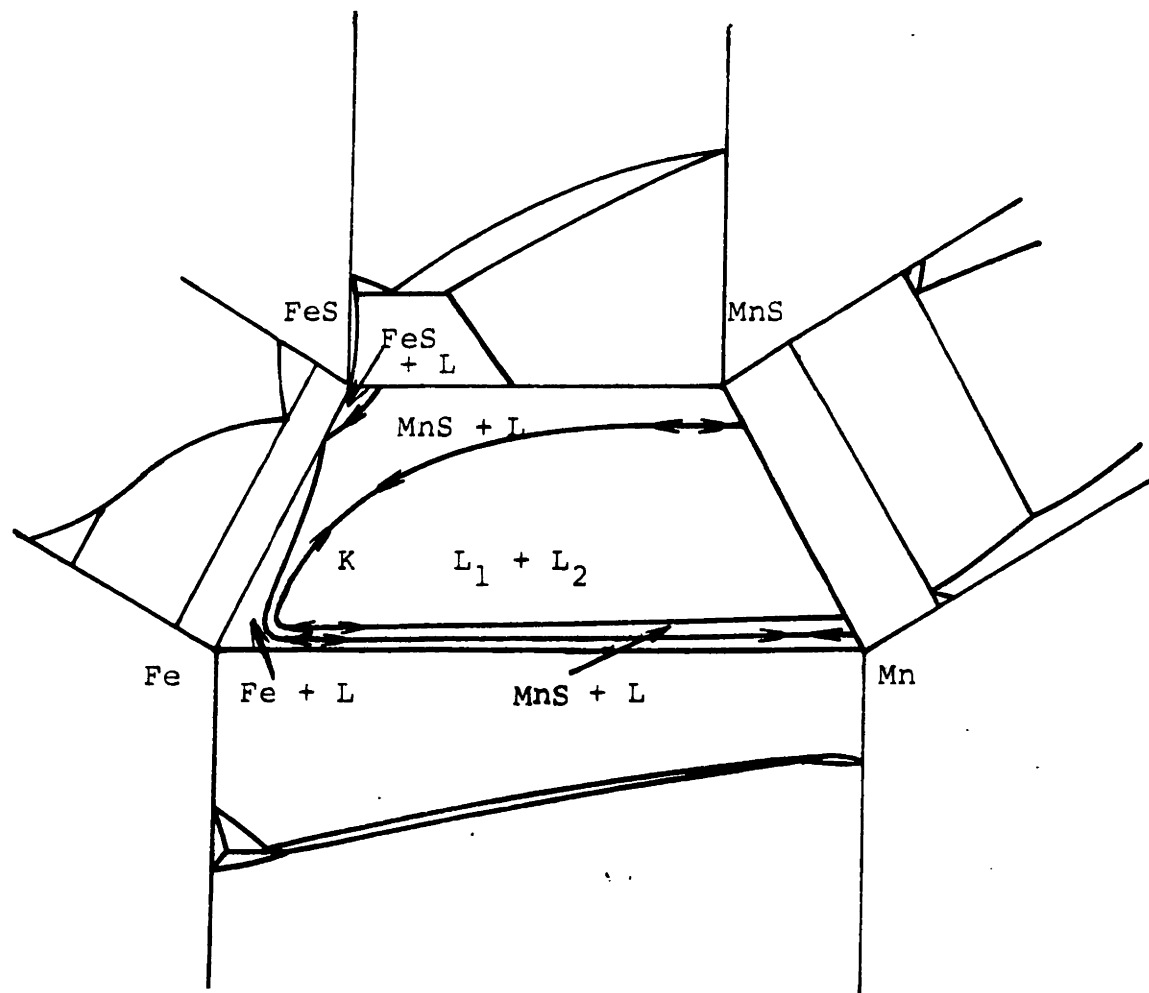


Figure 2: Qualitative projection of Fe-Mn-S phase diagram according to Vogel<sup>26</sup>.

Similarities will be considered first. It can be seen that there is agreement on the form of the contiguous binaries. Some differences are present as to exact temperatures and compositions but these are not shown as the present discussion is aimed at resolving differences in the relative positions of the liquidus lines. Wentrup and Vogel agree on the form of the miscibility gap. It stretches out across the phase diagram from the Mn-MnS side, dropping to a critical point near the Fe-FeS side, and reaching far into the Fe corner above the melting point of iron. The miscibility gap approaches the Fe-Mn side closely, although this is not apparent on the sketches. The course of the line from the FeS-MnS eutectic to a ternary eutectic very near the Fe-FeS binary eutectic is agreed upon.

Disagreement arises over whether the eutectic line intersects the miscibility gap or whether it merely approaches it closely on the Fe-FeS side before proceeding below the critical point to the ternary eutectic. This latter view is supported by Vogel and has the significance that the miscibility gap is surrounded on all sides by a surface of primary precipitation of MnS. The former view is supported by Wentrup, Schurmann, and others, and leads to a four-phase equilibrium. In this case the region of primary precipitation of iron on the Fe-FeS side is more extensive, and certain compositions can lead to the formation of a slag

phase instead of immediate precipitation of solid MnS. When a melt solidifies at higher initial manganese concentrations than this, near the maximum of the eutectic in the iron corner, it proceeds down the eutectic on the Fe-FeS side, encountering the four-phase plane on which solid Fe and sulfur-rich liquid coexist with solid sulfide and iron-rich liquid. The sulfide melts, and afterwards the temperature drops as iron continues to precipitate and slag phase forms in the remaining liquid.

Wentrup<sup>25</sup> based his version of the phase diagram on the research of Körber<sup>24</sup> and Meyer<sup>23</sup> plus his own work<sup>68</sup>. His support for the existence of the four-phase plane is based on the premise that the sulfide phase which forms becomes progressively lower in manganese content until its melting point falls below that of iron. Hilty and Crafts<sup>29</sup> derive the Fe-Mn-S diagram they present directly from Wentrup. They do not reference Vogel's work and apparently were not aware of it. Schurmann<sup>27</sup> references the work of both Wentrup and Vogel, while presenting Wentrup's version of the phase diagram. He states that there is insufficient evidence to conclusively support either version. Lichy<sup>15</sup> cites Schurmann as the source of the phase diagram used in his work. Later, Mohla and Beech<sup>19</sup> refer to Lichy, Schurmann, and Wentrup as the source of their Fe-Mn-S diagram, without mentioning Vogel. The intention of these comments



is to demonstrate that the many versions of the phase diagram which show the eutectic intersecting the miscibility gap are all based on one experimental source, Wentrup<sup>25</sup>. On the other hand, one single experimental source, Vogel<sup>26</sup>, supports the non-intersecting model.

In his experiments Vogel solidified a series of alloys along each of four vertical sections through the ternary at constant Fe/Mn ratios. He recorded the temperatures at which thermal arrest occurred in order to study the phase transformations. Vogel concluded from his data that the critical point of the miscibility gap lies about 1370°C with a composition of 76% Fe, 4% Mn, and 21% S. Analysis of slag and metal produced information on the direction of the lines in the miscibility gap. In agreement with the consensus of the other researchers Vogel found that to the right of a line drawn from Fe to MnS in Figure 2 the tie-lines fan out from the MnS corner, while to the left they are more nearly parallel to the Fe-MnS line. Vogel found that a line drawn between the maximum of the monotectic in the MnS corner to the coexisting liquid across the miscibility gap in the Fe corner nearly lies within a vertical section between Fe and MnS.

Vogel found the ternary eutectic to be about 1000°C. This is above values which have been reported previously and since for the Fe-FeS eutectic. Vogel concluded that previous

determinations of the binary eutectic had been too low, perhaps because of the presence of oxygen. The implications of Vogel's results are that either, (1) the ternary eutectic lies very near the Fe-FeS binary eutectic, or (2) the downward slope of the Fe-FeS eutectic valley into the ternary must be very slight.

In support of his version of the Fe-FeS side of the ternary Vogel presents several photomicrographs of alloys in the range beyond the critical point expected to produce primary iron according to Wentrup's diagram. In these photomicrographs primary MnS dendrites appear instead of iron dendrites. However, it is also clear that some of Vogel's experimental data points about 1400°C do not fall on the phase boundary lines he has drawn, but could possibly be evidence of thermal arrest on a four-phase plane. Despite this, the fact that manganese sulfide appears in the area where Wentrup's model predicts iron is considered sufficiently convincing so that Vogel's diagram is tentatively favored.

The present work has provided some information on the liquidus isotherms and the position of the eutectic as a byproduct of morphology studies. Appendix A describes this research and includes a discussion of the implications of Hilty and Crafts<sup>29</sup> work for the phase diagram. The phase diagram presented in Figure 3 includes the results of this research and is believed to include the most reliable data

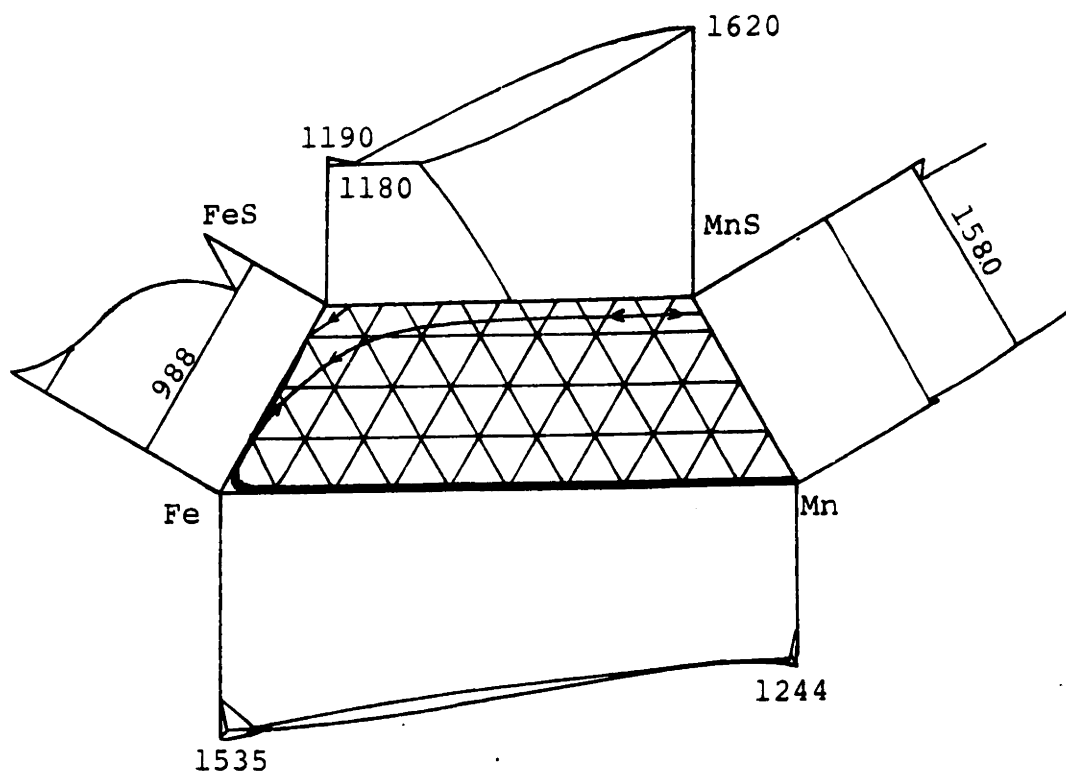


Figure 3: Actual Fe-Mn-S Ternary Diagram. Compositions marked in 10% intervals (by weight). Temperatures in  $^{\circ}\text{C}$ .

presently available. Figure 4 is a qualitative representation of the diagram in three dimensions and shows some of the features more clearly.

#### B. The Fe-S-O System

A qualitative version of this diagram was presented by Wentrup<sup>25</sup>. Experimental work by Hilty and Crafts<sup>28</sup>, Schurmann and Hertwig<sup>30</sup>, and Yarwood<sup>31</sup> provided much factual information on the system. A miscibility gap which starts from the iron-wustite side extends out across much of the system and terminates at a critical point near 1340°C. Eutectics starting from near the wustite composition, and from the FeO-FeS and Fe-FeS sides proceed along eutectic valleys to a ternary eutectic near 920°C. The absence of a slag phase which melts at a higher temperature than iron is one of the most important differences between this system and the Fe-Mn-S ternary.

#### C. The Fe-Mn-S-O System

Extensive consideration has been given in Appendix B to the quaternary Fe-Mn-S-O system. Accurate representation of quaternary systems is difficult, especially in cases where the related ternaries are not well known. An attempt has been made to understand the various phase fields which exist in the Fe-Mn-S-O system. Isothermal sections at 1% Mn through the 1500°C, 1490°C, and 1475°C quaternaries have been derived and presented in Figures 5, 6, and 7. Details of the

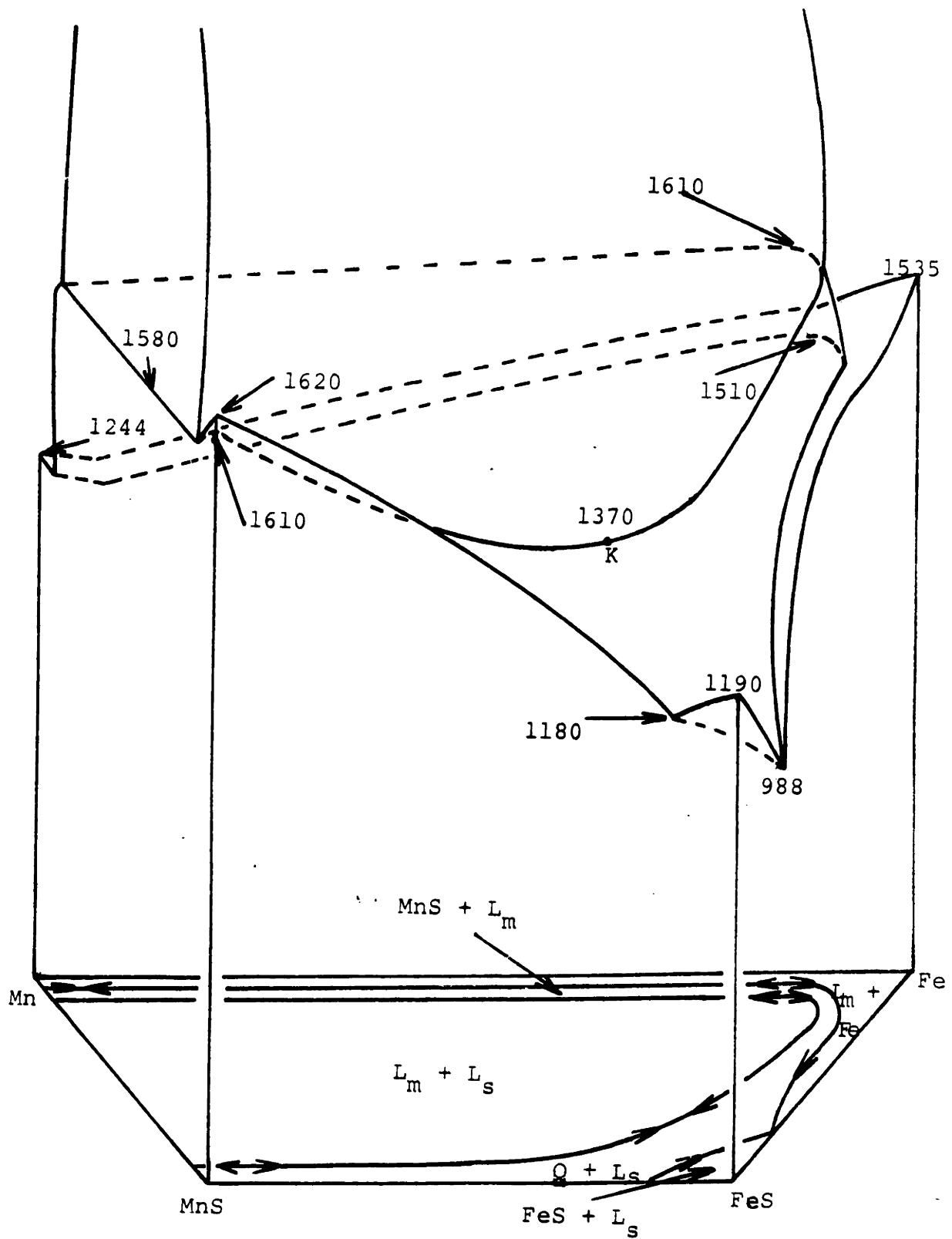


Figure 4: Appearance of Fe-Mn-S ternary, qualitatively represented. Temperatures in °C.

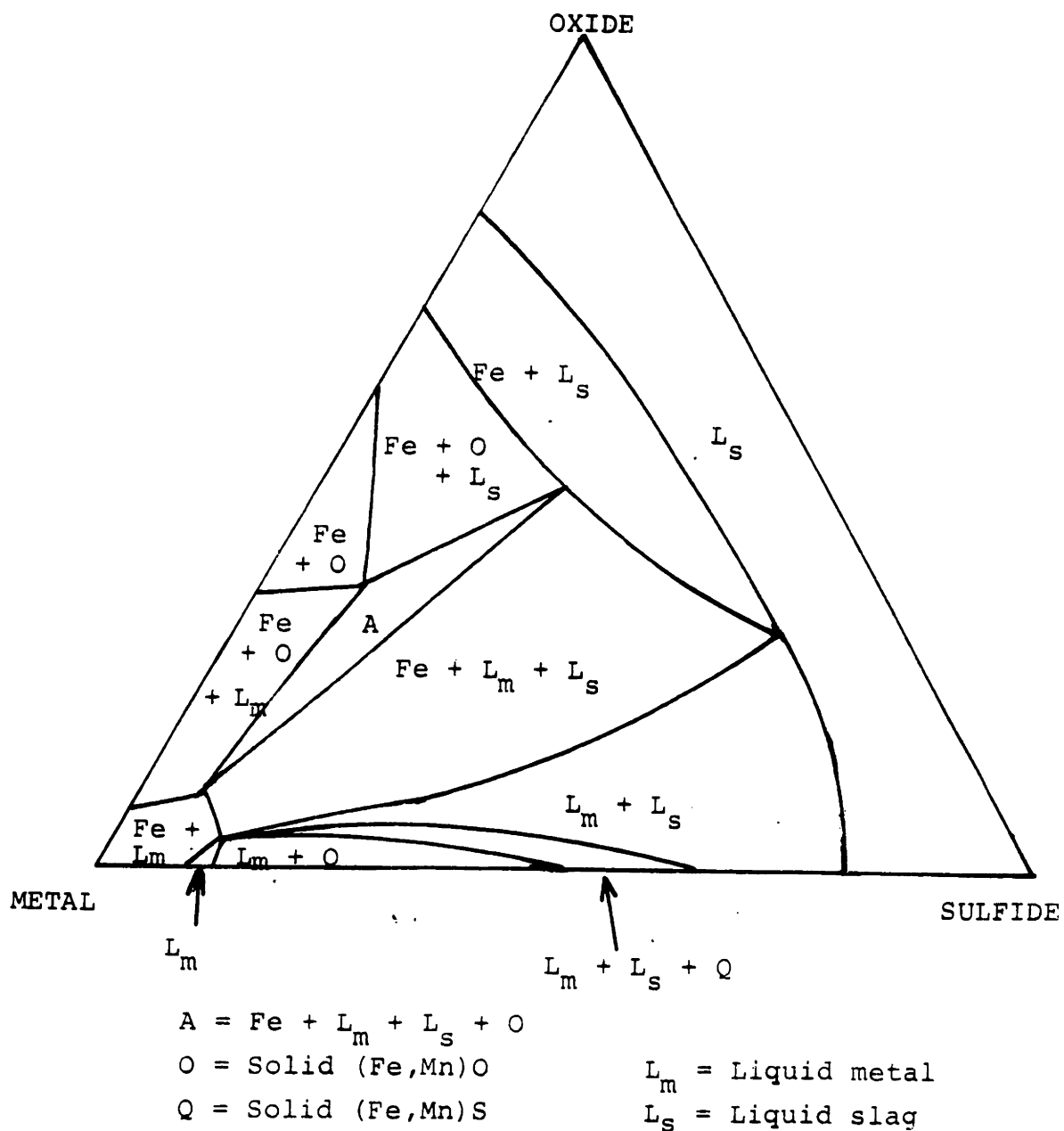


Figure 5: Qualitative isopleth of the Fe-Mn-S-O quaternary at 1500°C and 1% Mn. The isopleth is a plane of constant composition intersecting the isothermal quaternary tetrahedron.

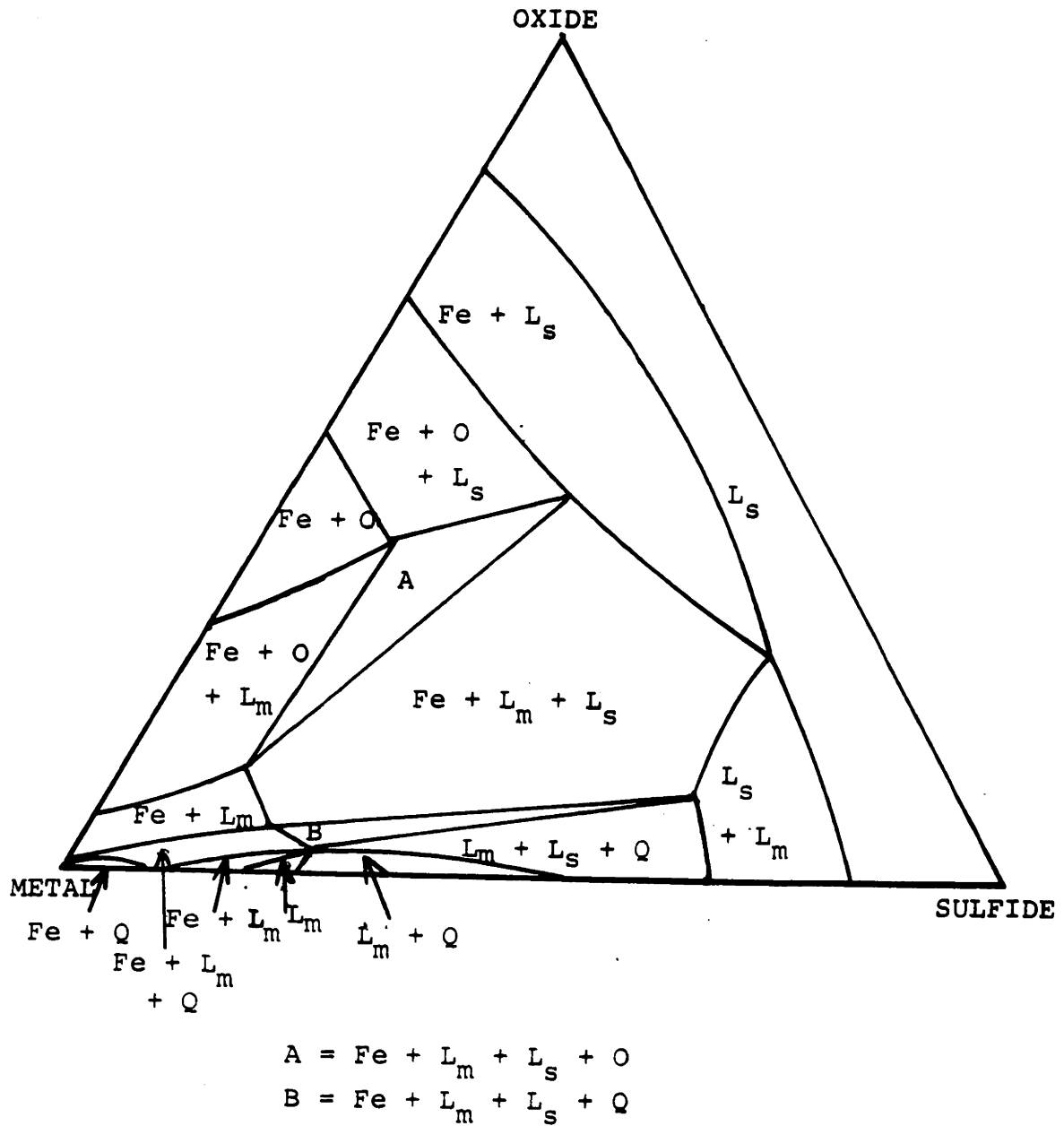


Figure 6: Qualitative isopleth of the Fe-Mn-S-O quaternary at 1490°C and 1% Mn.

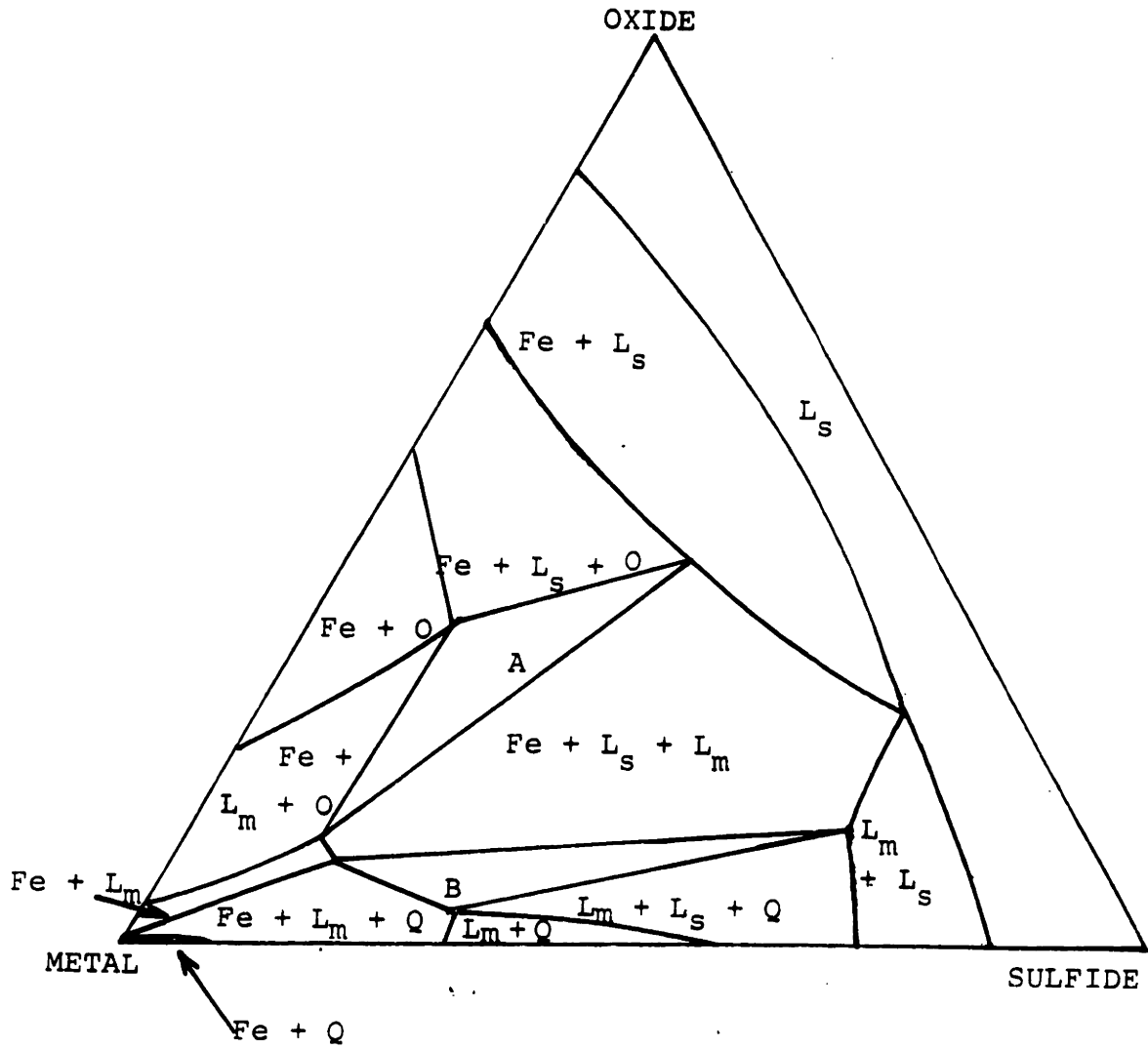


Figure 7: Qualitative isopleth of Fe-Mn-O-S quaternary system at 1475°C and 1% Mn.



steps taken to construct these diagrams are reported in Appendix B.

These figures show in a qualitative manner the relations between the phase fields which exist in the system. The boundaries of the phases change with overall manganese content, but the qualitative changes are not drastic over composition ranges encountered during solidification of most alloys.

These diagrams indicate regions of phase equilibrium at the given temperature and overall manganese content, but do not give the composition of the various phases. In general, tie-lines connecting phases in the quaternary intersect the plane of these diagrams and cannot be represented on them. However, the diagrams do show that at appropriate O/S ratios the melting point of the Q phase is so reduced that a three-phase Fe + L<sub>S</sub> + L<sub>M</sub> region is entered and solid sulfide does not form, but is replaced by liquid slag. Such a liquid slag contains significant amounts of oxygen, which lowers its melting point.

#### D. The Fe-S-C System

Several references on this system have already been given<sup>35,37</sup>. In addition, Sherman and Chipman<sup>69</sup> have studied the effect of carbon on the activity of sulfur in liquid steel. They found that the activity coefficient is increased not only by carbon, but also by phosphorous, aluminum, and silicon. For 3.5% C the activity coefficient of sulfur at 1600°C is increased to about 3.

Norro and Lundquist<sup>35</sup> studied the Fe-S-C system in the limiting case of carbon saturation in the liquid. They found that a miscibility gap extends from near the FeS-Fe<sub>3</sub>C side out into the ternary. Their experiments indicated that the peak of this gap is about 1970°C at 9.5% S and 4.9% C. Earlier work by Hanemann and Schildkötter<sup>71</sup> and Vogel and Ritzau<sup>72</sup> gives additional information on the position of the miscibility gap. The intersection with the primary iron field was found to lie in the general area of 7.5% S and 1.2% C. This means that even in the absence of manganese, slag phase can form in a high-sulfur, high-carbon melt. The carbon and sulfur levels necessary to intersect the miscibility gap may be reached because of segregation during non-equilibrium solidification. Large round iron sulfide inclusions can form in the system as a result of the miscibility gap.

Norro and Lundquist also investigated the solubility of carbon in FeS at 1400°C. They found it to be very low, less than 0.03% C.

#### E. The Fe-Al-S System

The research of Vogel and Hillen<sup>36</sup> provides some information on the system, despite the experimental difficulties they encountered. The phase diagram is superficially similar in some ways to the Fe-Mn-S system. A large miscibility gap extends from the Al-S side into the iron corner, with a critical point near the FeS-Al<sub>2</sub>S<sub>3</sub> side. However, there are many other features of the system which are quite

different from the Fe-Mn-S case. Several intermediate phases form along the Fe-Al side of the diagram, in contrast to the mutual solubility of iron and manganese. In addition, the melting point of aluminum is considerably lower than that of manganese. Because of these factors, the eutectic which starts in the aluminum corner does not climb into the iron corner and then down again on the Fe-FeS side as in the Fe-Mn-S system, but terminates instead near where it starts. Another major difference is that the melting point of  $\text{Al}_2\text{S}_3$  is less than that of iron, so there is no region of primary sulfide solidification in the iron corner.

Vogel and Hillen confirmed that a mixed crystal of  $\text{Fe}_3\text{Al}_2\text{S}_3$  exists, which implies that there is not an unbroken range of mutual solubility between FeS and  $\text{Al}_2\text{S}_3$ . They were unable to obtain much other information on that side of the diagram. Other parts of the ternary are also highly complicated. Vogel concludes, for example, that there are ten four-phase reaction planes near the Fe-Al side.

Most of these details are of no direct interest to the present research. Of more importance are the features of the system near the iron corner. The maximum of the miscibility gap in this region occurs at approximately  $1500^\circ\text{C}$  in the composition range of 5% S and 10% Al. The miscibility gap makes its nearest approach to the Fe-FeS side at 15% S, 0.5% Al, and approximately  $1400^\circ\text{C}$ . These figures clearly show that for most

alloy systems containing the usual levels of aluminum encountered in industrial practice, the direct effect of aluminum on the phase diagrams applicable to initial solidification is small. Indirect effects, such as the lowering of the O/S ratio through the formation of  $\text{Al}_2\text{O}_3$ , may be much more influential in modifying the resulting alloy structure. Direct effects, such as lowering of the freezing point of iron, are negligible. Aluminum has a very small effect on the liquidus.

There is one specific situation in which a direct effect of aluminum on sulfide morphology can be visualized. Both S and Al are strongly segregated during solidification. If the Al/S ratio is such that the miscibility gap can be intersected during a non-equilibrium solidification process which extends over a sufficiently large temperature range, then slag phase may form. Out of this slag  $\text{FeS}\cdot\text{Al}_2\text{S}_3$  mixed crystals can then precipitate. Vogel and Hillen present a photomicrograph of an alloy containing 4% Al and 1% S in which they say this process has occurred. The sulfides which result are distributed in the same manner around the dendrite arms as are Type II inclusions, but they are coarser than the MnS eutectic and are not sheetlike as are Fe-FeS eutectics. Vogel's data on the Fe-Al-S system indicates that the slag phase does not solidify until about  $1000^\circ\text{C}$ , long after the iron phase is solid. This is quite a

different process from what can occur in the Fe-Mn-S system, in which solid Fe and solid MnS form simultaneously. Even in the presence of some manganese, the  $\text{FeS} \cdot \text{Al}_2\text{S}_3$  mixed sulfides may occur as a result of stronger segregation of Al and S than of Mn.

#### F. The Fe-Si-S System

As is the case for the Fe-C-S and Fe-Al-S systems, the presence of the third component causes a miscibility gap to appear. Silicon forms the compound FeSi, which serves as a natural limit for one corner of a phase diagram determined by Vogel, Uschinski, and Theune<sup>33</sup>. The miscibility gap on the FeSi-FeS side extends over a composition range of approximately 1% S-30% S. The eutectic is on the FeS side of this gap. As in the above systems, the miscibility gap extends quite far out toward the iron corner. It falls to a critical point in the neighborhood of 1% Si, 18% S, and 1200°C. The maximum of the miscibility gap in the iron corner occurs at approximately 2.5% Si, 5% S, and 1380°C. In this region a sulfide rich slag phase can form in conjunction with liquid metal and with solid iron containing up to 17% Si. FeSi phase precipitates when the Si concentration in the melt reaches about 19% and the temperature falls to 1200°C with sulfur levels near the Fe-FeSi side.

G. Complex Systems Involving Modification of the Fe-Mn-S System by Si, Al, and C.

In order to derive the sort of qualitative phase diagram information generated for the Fe-Mn-O-S system more information is required than is presently available. For example, to create a pseudo-ternary diagram for the Fe-Mn-C-S system at a particular manganese level, information on the Fe-Mn-C and Mn-C-S ternaries is needed. Nevertheless, a few statements can be made about probable effects.

When sufficient manganese and sulfur are present in the Fe-Mn-S system the miscibility gap is intersected and tie-lines then run across the phase diagram from the eutectic valley near the iron corner to a high-melting sulfide phase. The effect of carbon, silicon, or aluminum, in order of decreasing influence is to lower the solubility of sulfur in the liquid metal. This is equivalent to extending the miscibility gap further into the iron corner.

Norro and Lundquist<sup>35</sup> found that carbon is practically insoluble in FeS. Dahl, Hengstenburg, and Düren<sup>17</sup> found no silicon or aluminum\* present in primary MnS even when the surrounding matrix contained up to 6% Si and/or Al.

---

\*Except as a small alumina particle.

The phase diagrams also indicate that FeS can contain only trace amounts of Si. As was discussed under the "Fe-Al-S System", FeS may possibly contain some Al in combination or solution. Dahl's results indicate that manganese can easily displace this. The purpose of these comments is to suggest that since C, Si and Al are virtually insoluble in the high-melting Q-phase of the pure Fe-Mn-S system they will have no effect on the melting temperature of that phase.

However, these elements are expected to:

- a) lower the liquidus of the metal phase
- b) lower the eutectic valley in the metal corner
- c) expand the miscibility gap further into the iron corner
- d) extend the region of primary precipitation of the high-melting sulfide further into the iron corner
- e) extend the temperature range of primary Q formation, because its melting temperature is unchanged, although the eutectic has been lowered.

#### IV. SOLIDIFICATION MODELS

##### A. Introduction

The equilibrium phase diagrams are a starting point for studying the inclusions which form during solidification. These phase diagrams have been discussed in Chapter III. By making various assumptions about departures from equilibrium during solidification, models can be generated for expected structures starting from a given location in the appropriate phase diagram. Proposed solidification paths for various systems are discussed below.

##### B. The Fe-Mn-S System

The following assumptions are made in considering the solidification of a closed volume element of metal:

1. There is negligible undercooling before nucleation or from curvature or kinetic effects.
2. There is no mass flow in or out of the volume element considered. Such flows might occur, for example, from movement of liquid by convection or to feed shrinkage, from movement of solid during solidification, or from diffusion.
3. Diffusion in the liquid within the volume element considered is complete.



4. Diffusion in the solid is negligible.
5. There is no solubility of sulfur in the iron phase. Actual value is 0.05% in  $\delta$ -Fe at 1500°C. In the qualitative diagrams to follow representation of such small compositions is impossible.

Given these assumptions, the course of solidification of an alloy with a composition on the manganese side of the line between the maximum of the eutectic and the MnS phase should proceed as diagrammed in Figure 8. The iron corner of the phase diagram has been enlarged and exaggerated for clarity, and the miscibility gap has not been shown. Different partition ratios for sulfur and manganese cause the bending of the curve across the Fe + L field. One of the assumptions made is that the partition ratios remain constant. Taking  $k_S = 0$  (already assumed), and  $k_{Mn} = 0.20$  (from an estimation of the tie-lines to  $\delta$ -iron in the ternary), the resulting equation for the solidification path is:

$$\left( \frac{C_L - Mn}{C_O - Mn} \right)^{1.3} = \frac{C_L - S}{C_O - S}$$

$C_L - Mn(S)$  = manganese (sulfur) concentration in liquid

$C_O - Mn(S)$  = initial manganese (sulfur) concentration

This relationship shows that sulfur increases in concentration faster than manganese, causing the solidification path to curve toward the Fe-FeS side of the ternary (Figure 8a).

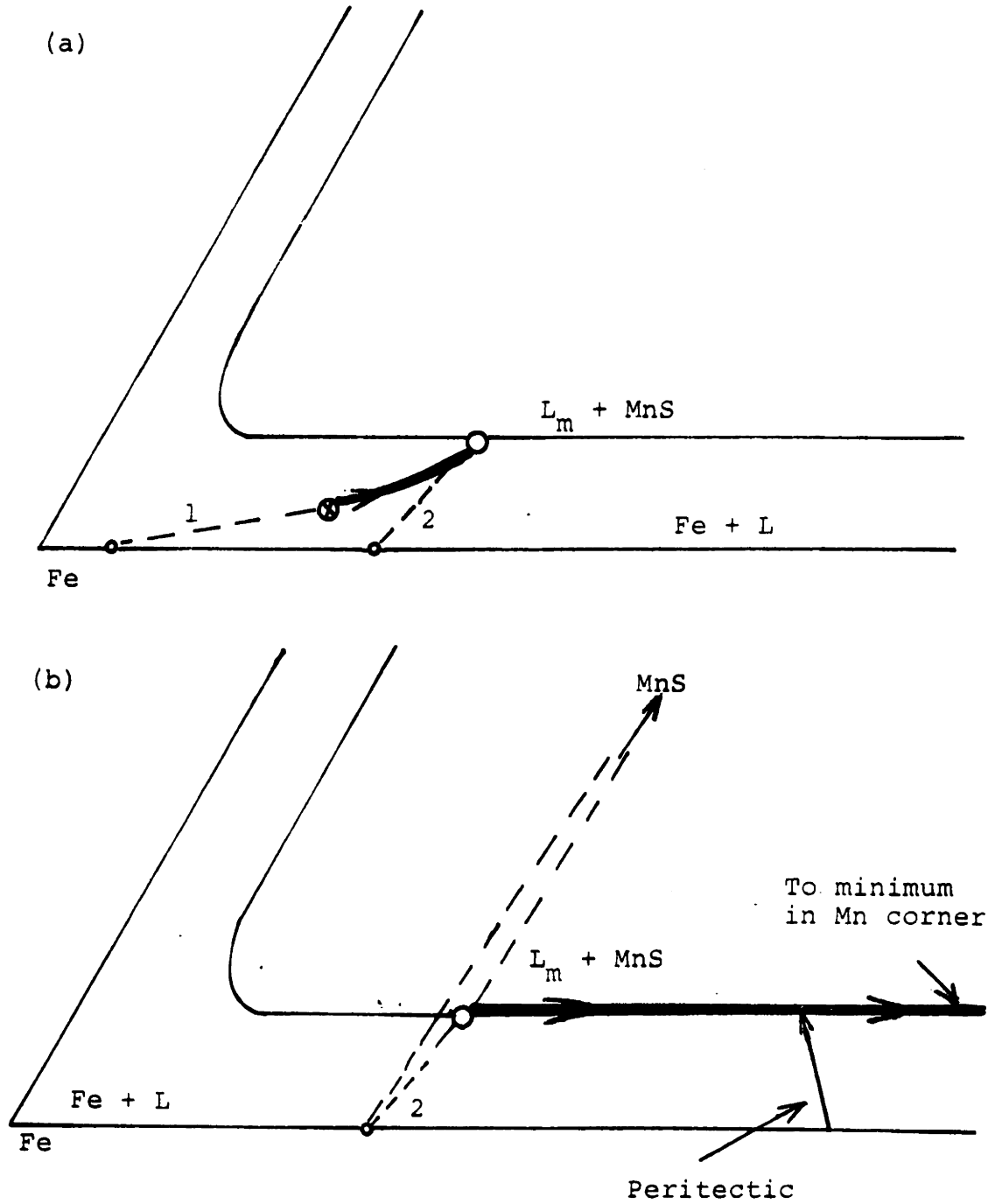


Figure 8: Solidification path of a typical high-manganese steel. Miscibility gap not shown

- a) Initial composition is  $\bullet$  and dashed tie-line (1) indicates solid composition. Heavy line shows change in liquid composition due to segregation of Mn + S. Dashed tie-line (2) shows metal composition at nucleation of sulfide.
- b) Shows tie-triangle when sulfide is nucleated. Liquid composition then proceeds down the eutectic valley to the minimum near the manganese peritectic.

The effect has been exaggerated. Significant curvature will only occur if the eutectic valley is not intersected until quite late in solidification. Below the iron peritectic, in ternary space,  $k_{Mn}$  changes because of increased manganese solubility in  $\gamma$ -iron. Solidification path curvature would be greater in this region. However, most systems of interest here will intersect the eutectic before the required  $C_{L-Mn}$  of about 8% is reached.

The eutectic valley is reached at a composition indicated by the open circle in Figure 8b. Three phases can now coexist over a range of temperatures. As solidification continues the composition of the remaining liquid follows the eutectic valley toward the manganese corner (Figure 8b). With the assumption of no diffusion in the solid, solidification will proceed to the lowest temperature at which liquid can exist in this side of the diagram<sup>84</sup>. In the present case that will occur on the four-phase plane representing equilibrium between  $\gamma$ -Mn,  $\delta$ -Mn, MnS, and  $L_m$ . This is represented by the diamond in the manganese corner of Figure 10. It implies that liquid metal will persist to just below 1240°C and will have a manganese concentration of 90%. Only if the assumption of no solid state diffusion breaks down due to decreasing diffusion distances near the end of solidification, will solidification end before reaching this theoretical limit.

When the liquid composition in the eutectic valley reaches about 8% Mn, a peritectic reaction will be encountered representing the transformation of  $\delta$ -iron to  $\gamma$ -iron of a higher manganese content. Vogel<sup>26</sup> considered in some detail the equilibria and phase transformations occurring in the iron corner as a result of the peritectic. If solidification could take place in such a manner that equilibrium exists within each phase as well as at the interface (requiring complete solid as well as liquid diffusion) then the peritectic reaction would occur at constant temperature and result in the complete disappearance of  $\delta$ -iron. Under the present assumption of no solid state diffusion thermal arrest will not occur. There will merely be a shift of the tie-lines from solid MnS and the liquid to  $\gamma$ -iron of higher manganese content than the previously formed  $\delta$ -iron. Composition of the iron phase forming with solid sulfide will therefore change discontinuously. For most alloys of interest this will occur late in solidification. The  $\delta$ -iron will transform later, at lower temperatures, without a change in composition.

A different initial composition will now be considered, using the same assumptions. If the melt is again on the manganese side of the phase diagram, between the eutectic and the miscibility gap, the first solid phase encountered will be solid MnS (Figure 9). Information on the Fe-Mn-S phase diagram indicates that this region is very narrow, and

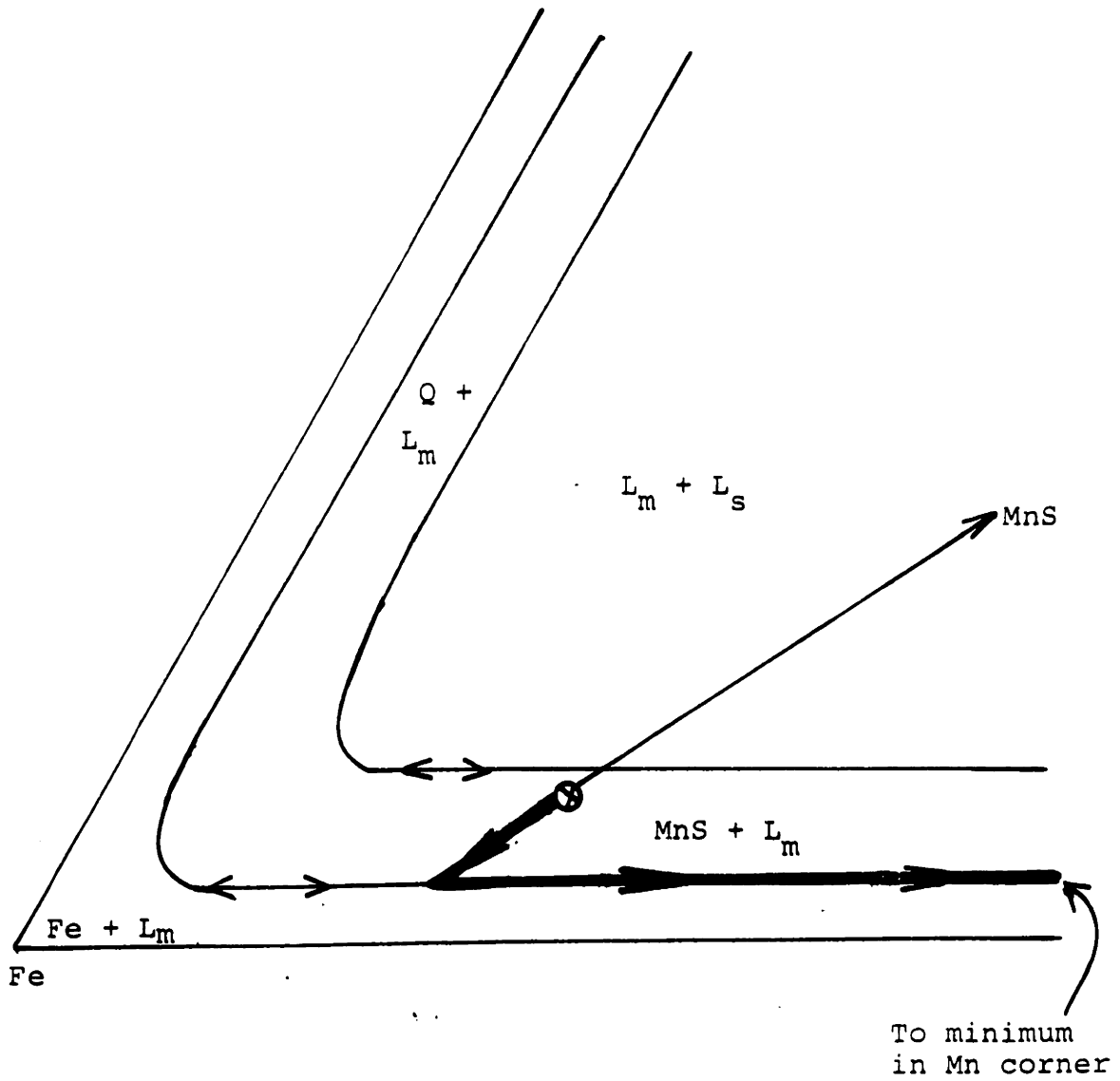


Figure 9: Solidification path if initial composition is between the miscibility gap and the eutectic valley.

that it is also very steep. The difference in temperature at their maxima between the eutectic and the miscibility gap is approximately  $100^{\circ}\text{C}$  ( $1610-1510^{\circ}\text{C}$ ). The  $\text{MnS} + \text{L}_m$  region evidently extends over only a fraction of a percent in composition, so it must slope steeply. The probability that an alloy will intersect the  $\text{MnS} + \text{L}_m$  region initially is therefore small. The structure, under the assumptions of the model, is expected to show some sort of primary sulfide. The morphology will depend upon such factors as heat extraction, diffusion, surface contamination, entropy of fusion, concentration of solute, and the slope of the  $\text{MnS} + \text{L}_m$  surface. Nucleation has been assumed to occur near its theoretical temperature, as the  $\text{MnS} + \text{L}_m$  surface is intersected. The composition change of the liquid is shown in Figure 9. When the eutectic valley is reached, solidification proceeds as diagrammed in Figure 8b. The point to be made here is that the specimen should consist of nearly 100 percent Fe-MnS eutectic, with primary sulfide dispersed throughout.

If the initial composition is in the miscibility gap on this side of the diagram a more complex situation results. The situation can perhaps be clarified with the following example: A melt containing sufficient sulfur so that an iso-concentration line parallel to the Fe-Mn side of the phase diagram intersects the miscibility gap is held at a temperature greater than  $1610^{\circ}\text{C}$ . To this melt Mn is added in a

quantity greater than the MnS stoichiometric value. When this is done, a liquid slag containing on the order of 5 percent iron will separate from the metallic liquid and co-exist with it at temperatures above  $1610^{\circ}\text{C}$ . At a temperature between  $1610^{\circ}\text{C}$  and  $1580^{\circ}\text{C}$  depending on the overall manganese content, the system will intersect the surface of the  $L_s + L_m + \text{MnS}$  field in ternary space. Examination of the ternary phase diagram (Figure 4) will show that in the MnS corner the miscibility gap intersects the field of primary precipitation of MnS at a maximum temperature of  $1610^{\circ}\text{C}$ , which falls to  $1580^{\circ}\text{C}$  on the Mn-MnS binary. The compositions of the three phases when the system first enters the three-phase field is shown by the solid tie-triangle in Figure 10. The compositions of the three phases when the slag has solidified is shown by the dashed tie-triangle.

As the slag solidifies it will reject both iron and manganese. Since the initial composition was on the manganese-rich side of the MnS stoichiometric ratio, and since pure MnS is precipitating the net effect must be to enrich both liquid phases in manganese. The effect has been greatly exaggerated here. The Mn-MnS monotectic at  $1580^{\circ}\text{C}$  is probably only approached by the slag phase at overall manganese and sulfur levels far above the range of interest here. Solidification of the slag probably stops before the monotectic is reached. The lever rule can be used here since pure MnS is forming. When solidification of the slag is

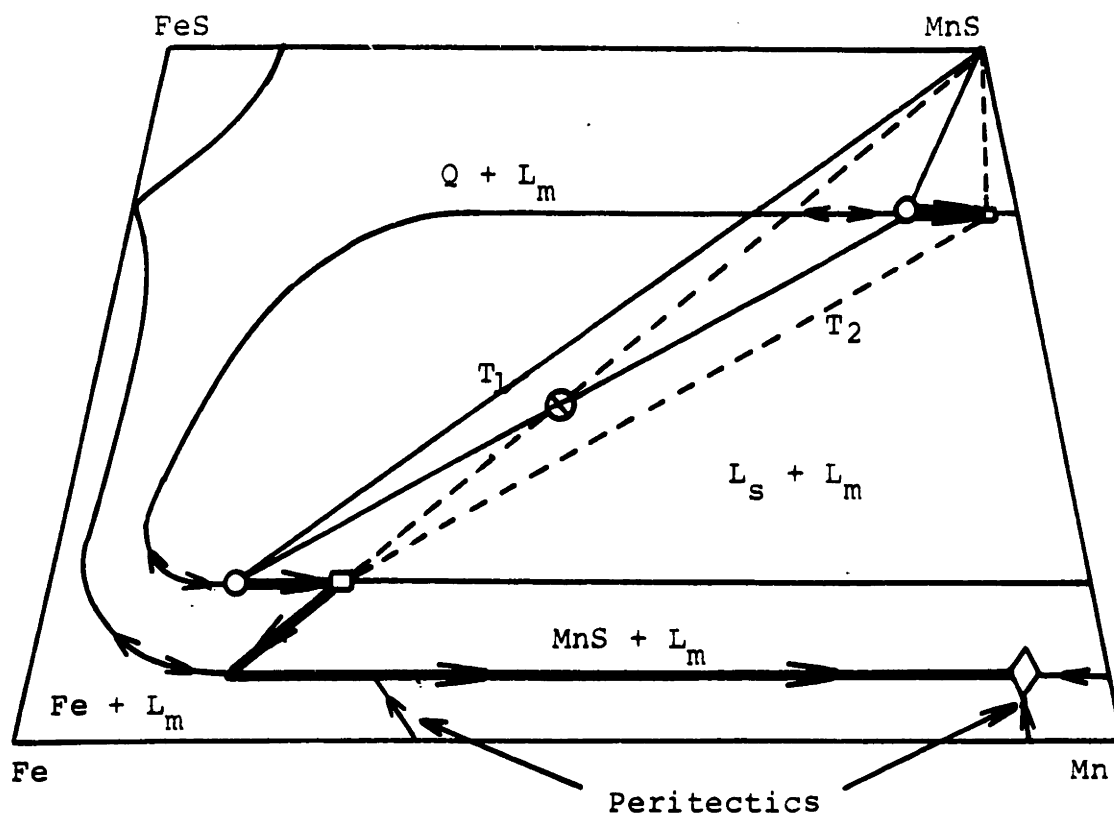


Figure 10: Course of solidification in an alloy of initial composition in the miscibility gap.

⊗ = initial composition

Solid tie-triangle is at  $T_1$ .

Dashed tie-triangle is at  $T_2$ , when solidification of slag is complete.

$$T_1 > T_2$$



complete, the  $MnS + L_m$  two phase region is entered and solidification should proceed as already described and pictured in Figure 9.

A similar approach can be used to model the course of solidification on the Fe-FeS side of the phase diagram. Vogel's version of the phase relations, according to which the eutectic does not intersect the miscibility gap, will be considered first. On this side of the diagram the amount of manganese dissolved in freezing iron will be less than on the right of the eutectic maximum. The path of the liquid composition in an alloy with a Mn/S ratio less than the stoichiometric value of 1.7, and whose overall composition falls in the  $Fe + L_m$  region has been schematically represented in Figure 11, starting at the crossed circle labelled "1". An initial composition in the field of primary precipitation of Q sulfide would follow the path starting at the crossed circle labelled "2". When the initial composition falls within the miscibility gap slag phase will separate, and the expected path of solidification after freezing of the slag begins will be as illustrated by the heavy lines leading from the ends of the tie-triangles including the crossed circle labelled "3". The temperature at which the  $L_s + L_m + Q$  field is entered may be considerably lower on this side of the phase diagram than in melts where a substantial excess of manganese is present, because the liquidus of the mixed Q-sulfide is less than that of pure MnS.

When the Q phase begins to solidify, the manganese concentration of the slag phase is reduced, along with the sulfur content as the metallic and sulfur-rich liquids approach each other at the critical point. In most cases the reaction will not proceed far before the slag phase is used up at the solid tie-triangle, as shown in Figure 11.

Wentrup's phase diagram is somewhat more complex because of the existence of a four-phase plane. The expected course of solidification is shown in Figure 12. If the initial composition is on the eutectic valley at the crossed circle, the first iron to form will have the composition  $Fe_1$  and the sulfide will be at  $Q_1$ . The tie-triangle for this initial stage of solidification has not been drawn in to avoid cluttering the diagram. As solidification proceeds the phases will follow the paths shown by the heavy arrows until the eutectic liquid composition is intersected by the miscibility gap and the four-phase plane is encountered. At this point the phase equilibrium will be as indicated by the solid tie-triangle and will transform to the dashed triangle during the constant temperature reaction. Several assumptions have been made in plotting these solidification paths. The actual compositions of Q are unknown. Vogel concluded that very little iron would dissolve in it until temperatures fall to the region of  $1400^{\circ}C$ . However, if the miscibility gap intersects the eutectic, as in this model, the sulfide seems likely to contain significant amounts of iron at higher

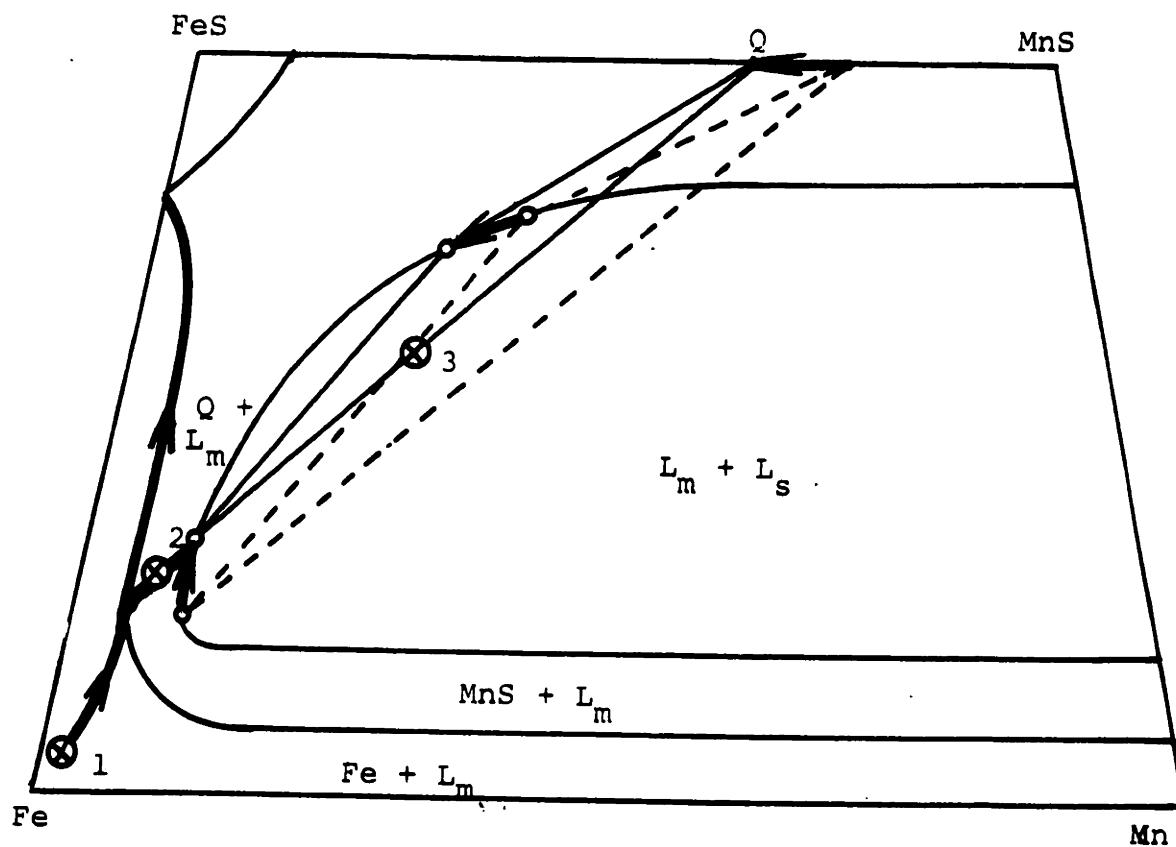


Figure 11: Solidification paths of three specimens with initial compositions 1, 2 and 3. Effect of coring of sulfide phase ignored. All will probably reach the ternary eutectic, although the volume fraction of ternary eutectic may be quite small. Arrows point to lower temperatures.

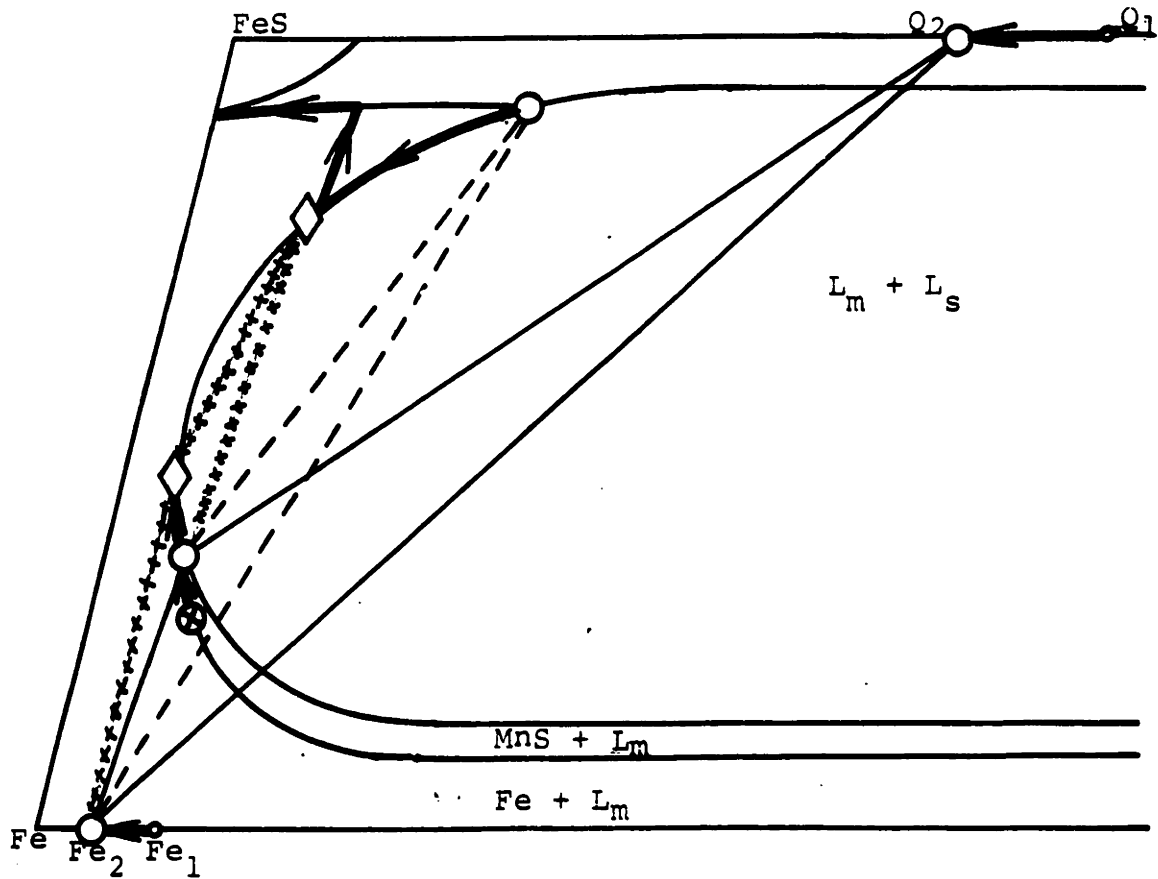


Figure 12: Course of solidification of an alloy with initial composition on the eutectic, according to Wentrup's phase diagram. Change in phase equilibrium at four-phase plane represented by transfer from solid to dashed tie-triangle. Initial composition at  $\otimes$ . Tie-triangle with X's represents final freezing of liquid metal phase.

temperatures than that. The composition of precipitating sulfide is assumed to change as indicated schematically, from  $Q_1$  to  $Q_2$ . The manganese content of the iron probably only changes very slightly from  $Fe_1$  to  $Fe_2$ . Because absence of solid state diffusion has been assumed coring of the solid phases will occur, creating a greater volume fraction liquid at a given temperature than would be the case if the manganese concentrations in the solids were uniform. If sulfide rods form, coring occurs longitudinally, making the assumption of insignificant diffusion especially valid. The expected result of this is that slightly more liquid metal phase is still left when the four-phase plane is intersected than would be indicated by the diagram as drawn. The effect is probably small because 1) the weight fraction of the sulfide is small, 2) the difference between  $Q_1$  and  $Q_2$  may be small, and 3) the difference between  $Fe_1$  and  $Fe_2$  is very small. For these reasons, and for simplicity, the effect has been ignored in drawing Figure 12.

A more detailed consideration of the events occurring on the four-phase plane is necessary. Figure 13 is a simplified representation of the tie-lines connecting the four-phases. It has been tilted to generally conform to the orientation and nomenclature of Figure 12. The solid diagonal connects the eutectic liquid with sulfide forming just above the reaction plane. The dashed line is part of the dashed tie-triangle in Figure 12. The composition at

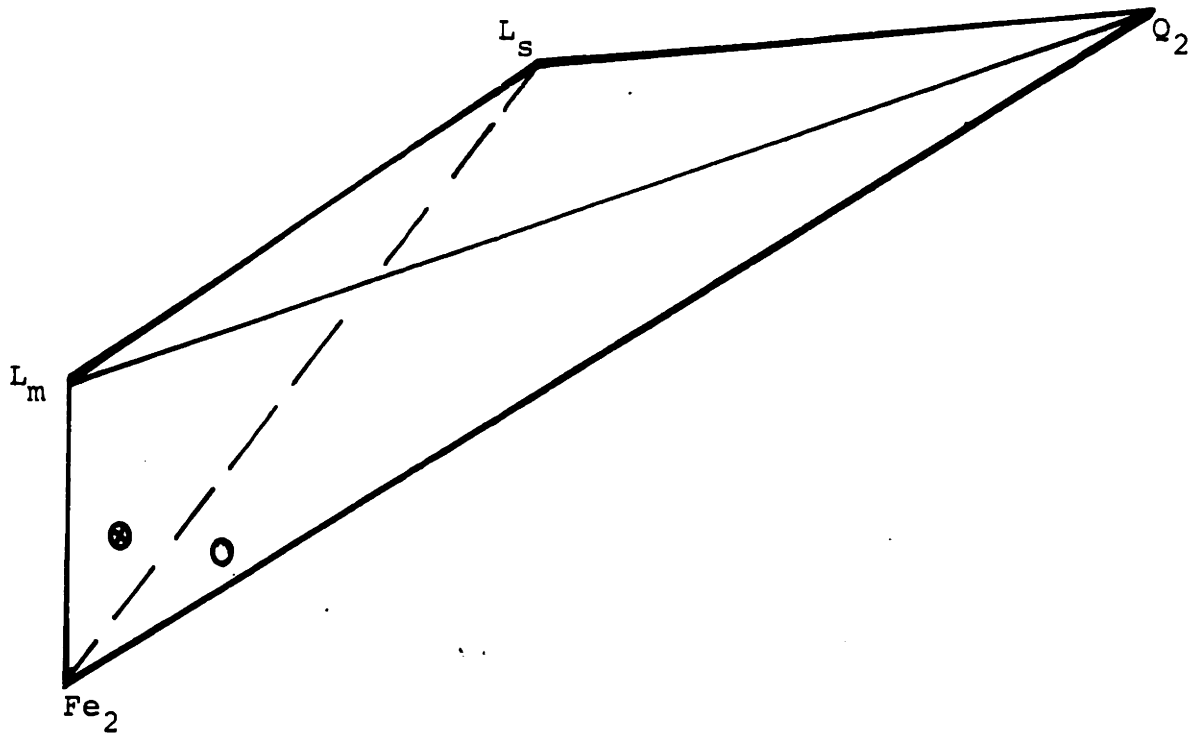


Figure 13: Four-phase reaction plane, isolating the phases which are in equilibrium in Figure 12.

the crossed circle represents the initial liquid composition used for the discussion of Figure 12. When the four-phase plane is encountered this initial composition yields the following reaction:  $Fe_2 + L_m + Q_2 \rightarrow Fe_2 + L_m + L_s$ .

Sulfide phase of composition  $Q_2$  disappears and is replaced by a slightly larger weight fraction of slag. The amount of solid iron increases, and the amount of liquid metal decreases. Under the assumption of no solid state diffusion, and because of the variation in sulfide composition, remelting will occur only at the interface and solidification will immediately continue with the formation and growth of slag and solid iron at the expense of liquid metal. When the tie-triangle indicated by crosses is reached metal phase will disappear, and solidification will proceed by precipitation of iron from the slag, followed by coprecipitation of Fe and Q, and finally by formation of FeS, Fe, and Q at the ternary eutectic.

If the initial eutectic liquid has a higher manganese content, represented by the open circle in Figure 13, a different process is expected to occur when the four-phase plane is intersected. A longer solidification path will be required to reach the reaction plane, resulting in more of the eutectic and less liquid metal. During this reaction liquid metal disappears instead of solid sulfide, in contrast to the situation described above. The reaction is:  $Fe_2 + L_m + Q_2 \rightarrow Fe_2 + L_s + Q_2$ . Some sulfide is dissolved, but not all, and

additional iron is precipitated. The remaining liquid,  $L_s$ , then travels directly down the  $Fe + L_s + Q$  eutectic valley instead of around the miscibility gap as in the earlier case.

Summary: The expected path of solidification on the Fe-Mn side of the Fe-MnS diagonal may be simply described. Primary iron or primary sulfide forms first depending upon whether the miscibility gap is intersected. This is followed by simultaneous precipitation of both phases along the line of two-fold saturation until the minimum temperature near the manganese corner is reached. Solidification on the Fe-FeS side of the Fe-MnS line is complicated by the fact that there is disagreement in the literature on the form of the phase diagram in that region. Models are proposed for solidification according to each of the two competing versions of the phase diagrams. One version (the Vogel version) implies that solidification will proceed directly down the line of two-fold saturation to the ternary eutectic. The other (the Wentrup version) implies that the miscibility gap is intersected, resulting in the formation of liquid slag particles in the liquid metal. It is hoped that comparison of the two models with the experimental results will enable the correct version of the phase diagram to be defined.



### C. The Fe-Mn-S-O System

Because so little quantitative or even qualitative data on this system is available only a general discussion is possible. A rough calculation may be made to approximate the segregation which takes place during the initial stages of solidification, which will serve as an example of the sort of effects which can be expected. An alloy of the following initial composition will be considered: Mn = 1%, S = 0.1%, O = 0.01%, remainder Fe. Diffusion of manganese in the solid will be assumed to be nil. Equilibrium is assumed to exist at the liquid-solid interface. The solubility of oxygen in the solid is taken to be zero. Sulfur solubility is about 0.05% at the liquidus temperature. Since the oxygen level is so low the Fe-Mn-S phase diagram will provide a reasonably accurate approximation of the early stages of solidification. The liquidus should be intersected at about 1520°C. Values  $k_S = 0.05$  and  $k_O = 0$  are therefore implied. The partition ratio of manganese in the delta iron region has already been estimated as approximately  $k_{Mn} = 0.2$ . This value should be reasonably constant above 1500°C. The effect of changing sulfur and oxygen values on  $k_{Mn}$  is ignored. Application of the Scheil equation to these conditions leads to the following composition of the liquid at 80% fraction solid: Mn = 3.55%, S = 0.46%, O = 0.05%. Rejection of the alloying elements

from the growing iron phase causes the composition of the liquid to become enriched to such an extent that it nearly reaches the position of the pure Fe-Mn-S eutectic when solidification is only 80% complete. This segregation also causes the oxygen level and O/S ratio to increase to a point where the freezing point of the sulfide is significantly lowered. Precipitation of iron from the liquid is occurring over a range of temperatures and compositions and cannot be traced on a projection of liquidus lines as was done for the pure system because these lines move as solidification proceeds. Figure 5 for example refers to just one particular overall manganese content and temperature.

Depending upon the initial concentrations and O/S ratios, segregation occurring along the Fe + L<sub>m</sub> surface will cause intersection of the Fe + L<sub>m</sub> + L<sub>s</sub> region or the Fe + L<sub>m</sub> + Q region which appears when the temperature falls below 1500°C (Figure 6). Intersection of the Fe + L<sub>m</sub> + Q region should be favored by high initial sulfur levels because differential segregation will have less chance to increase the O/S ratio in the last stages of solidification. If the initial O/S ratio is high enough the Fe + L<sub>m</sub> + L<sub>s</sub> region will be intersected and liquid slag droplets will be formed in the interdendritic liquid. As the temperature falls further the Fe + L<sub>m</sub> + L<sub>s</sub> + Q region shown in Figures 6 and 7 will expand and solid sulfide will begin to precipitate in the slag droplets.

At high initial levels of sulfur which place the system in the miscibility gap the  $L_m + L_s + Q$  region may be intersected shortly before precipitation of iron begins in the  $Fe + L_s + L_m + Q$  region. This should result in a different structure than the low sulfur case because the liquid slag phase is now a primary phase instead of secondary to iron precipitation.

#### D. Models for Sulfide Formation in Systems Containing Carbon and Silicon

##### 1. Phase Relation Effects

Both carbon and silicon have a very strong effect on the liquidus temperatures of iron alloys, and on the activity of sulfur dissolved in them. Three major factors are expected to influence the formation of sulfides in melts containing significant amounts of these elements:

- a) Segregation of solute elements during solidification may increase their concentration in the remaining liquid far above their average value<sup>76</sup>.
- b) The effect of carbon and silicon on the activity of sulfur, especially when segregated

during solidification, may strongly decrease solubility of MnS in the remaining liquid.

- c) The lengthened liquid-solid region means that longer solidification times result from the same cooling rates. This possibly increases the effects of coarsening, and may change reaction rates or other factors which could determine morphology.

Representation of such effects on phase diagrams is impossible because quaternary and quinary systems are involved, and these are unknown. However, one source of information is available which is very useful in attempting to understand sulfide precipitation in segregation zones between dendrite arms. This source is a research program conducted by W. Oelsen to study the effects of carbon saturation on the solubility of manganese and sulfur in liquid metal. These results were reported by Schurmann<sup>27</sup>, and have been used in the present research as a key to understanding the morphologies which occur when sulfur solubility and melting temperature are lowered by alloy additions. Oelsen determined the solubility product over a range of temperatures for manganese and sulfur in iron which had been melted in a graphite crucible. Isothermal curves for the liquid and solid sulfide surface in carbon saturated melts were thereby determined.

These were plotted as a phase diagram in Schurmann's paper and are reproduced here in Figure 14. It should be emphasized that the diagram is not the projection of a true ternary or even of a pseudo-ternary derived for a constant carbon level, but is a representation in which the carbon level is made implicit by the condition of saturation. The actual carbon content in the melt varies with temperature in order to maintain equilibrium with the graphite crucible. The diagram is made useful for tracing the course of sulfide solidification prior to formation of solid metal by the assumption that the phase which forms is pure MnS. This avoids the difficulty of having to represent changes in composition which would occur if tie-lines from the  $L_m + \text{MnS}$  surface ran to a composition in quaternary space because of carbon dissolved in the sulfide. The assumption of no carbon in the sulfide is expected to be very good. Evidence of formation of carbides within primary MnS has not been reported elsewhere or observed here. Furthermore, the dashed line in Figure 14, which is the boundary between the miscibility gap and  $L_m + \text{MnS}$  surfaces would intersect the  $1600^\circ\text{C}$  isotherm if both were extended. This is approximately the highest freezing point for MnS which Vogel determined for the pure system, and reinforces the idea that pure MnS forms even at carbon saturation.

The effect of carbon on activity and solubility of sulfur in the melt can be appreciated by studying Figure 14.

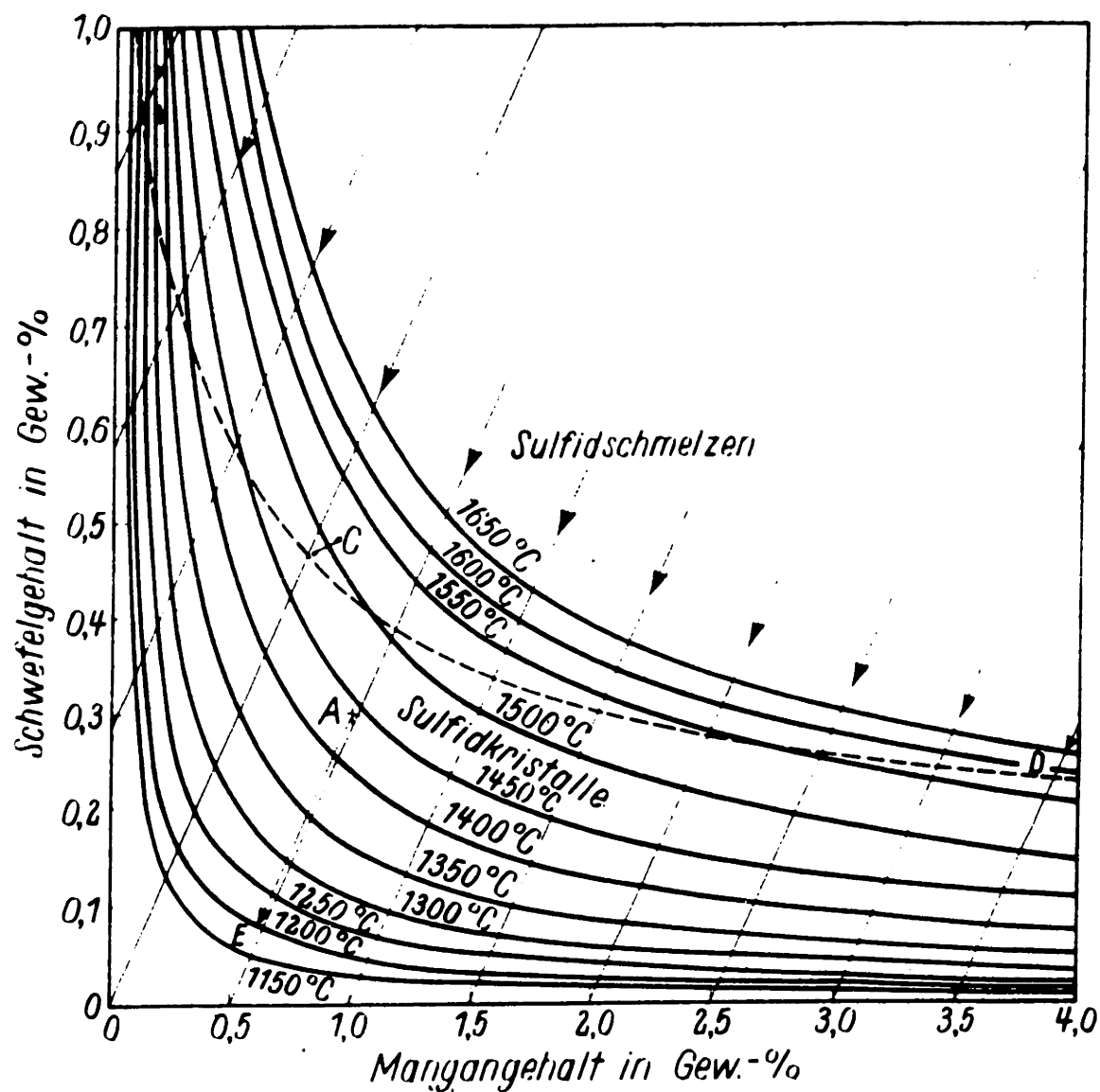


Figure 14: Derived from Schurmann<sup>27</sup>. Shows sulfur solubility as a function of temperature and manganese content for iron melted in a graphite crucible. Dashed curved line is the boundary between the miscibility gap and region of solid sulfide formation. If initial melt composition falls on one of the diagonal parallel lines, subsequent melt composition follows the same line as temperature decreases.

Along the manganese side of the diagram the ability of carbon to decrease sulfur solubility in the melt is somewhat counteracted by an opposite effect of manganese<sup>69</sup>. The result is that sulfur solubility in the manganese-rich region is only reduced to about half that observed in the pure system.

When the manganese level is low relative to sulfur, however, the effect of carbon-saturation is much greater. For example, the pure Fe-Mn-S phase diagram indicates that along the lower boundary of the miscibility gap 0.5% Mn can coexist in the melt with about 2.5% S at a temperature of 1450°C. If the melt is saturated with carbon, however, the research of Oelsen indicates that the amount of sulfur in equilibrium with 0.5% Mn is now reduced to 0.55%, again at 1450°C. The solubility product varies strongly with temperature, so that at 1150°C corresponding values are 0.5% Mn and 0.05% S, according to the diagram. If the original composition of a carbon saturated melt is known, the diagram can be used to predict the temperature and composition at which the first sulfide is formed as well as the composition of the last liquid to solidify. For example, if the initial composition is 2.45% Mn and 0.24% S, the sulfide will begin to precipitate as a solid (in equilibrium) at a temperature of 1520°C, and will continue until solidification is complete at about 1150°C when the composition of the liquid is reduced to about 2.05% Mn and 0.02% S. The composition of the melt follows the particular one of the parallel diagonal lines which passes through the initial

composition. A pseudo-binary cut through 2.45% Mn and 0.24% S and pure MnS is reproduced in Figure 15 based upon Figure 14. For comparison, a similar cut through the Fe-Mn-S system is also included (dashed lines). The most notable modifications caused by carbon are the tremendous extension of the  $Q + L_m$  region downward and toward the Fe(C) side, and the decrease in solubility of MnS. The diagram is fairly accurate, being based on empirical determinations, but tie-lines may run somewhat outside the plane shown. Lower carbon concentrations should have a similar, but less extreme, effect on sulfide formation.

The effect of silicon on sulfur activity coefficients is similar to that of carbon, but it is not so severe on a weight percent basis. Whereas it takes 3.25% C to increase the activity coefficient of sulfur 2.5 times at 1600°C, 5.4% Si is required to have the same effect<sup>69</sup>. Nevertheless, the principle is clear: solid (or liquid) MnS is expected to form in silicon-bearing liquid at manganese and sulfur levels which would have been in the single liquid region in the pure system, in a manner analogous to that described above for the case of carbon.

If solidification of iron starts before or soon after MnS precipitates, microsegregation will be an important factor causing additional sulfide formation. Based upon available data<sup>65</sup>, a few rough calculations may be made of the extent of segregation in melts containing carbon or silicon.



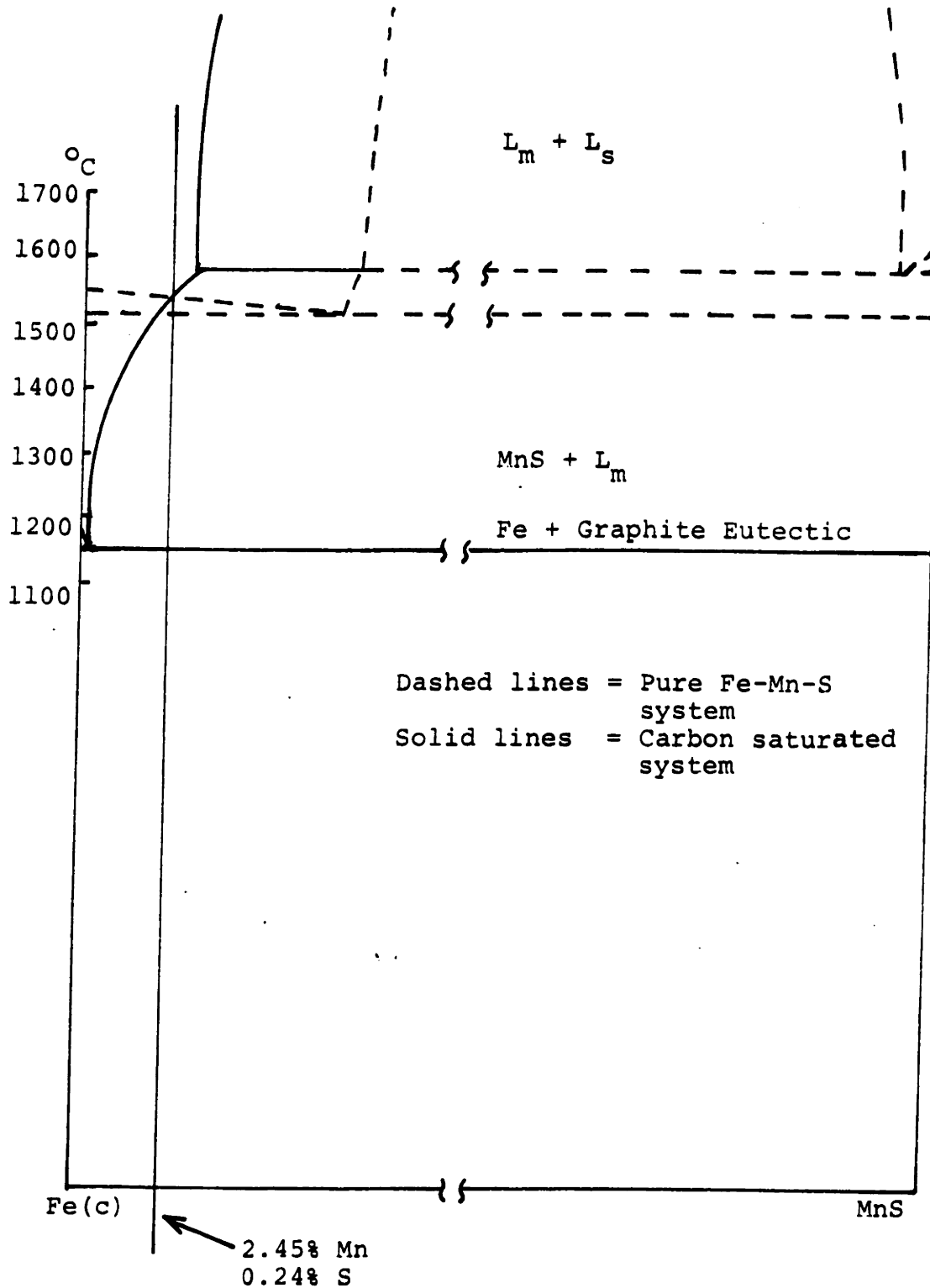


Figure 15: Pseudo-binary cuts between Fe and MnS for pure system (dashed lines), and for carbon saturated system. Shows that an initial composition of 2.45% Mn and 0.24% S would intersect Fe +  $L_m$  region in the former, and MnS +  $L_m$  region in the latter.

Insufficient information is available on the interaction effects of the various elements present on partition ratios, diffusion, melting temperatures, etc., to permit more than order-of-magnitude calculations. The following assumptions are made, plus others mentioned in individual cases:

1. Assumptions 1-3 on page 59 are also made here.
2. Diffusion of carbon in the solid metal is assumed to be complete so that the equilibrium phase diagram gives the carbon composition of the liquid.
3. Diffusion of silicon, sulfur, and manganese in the solid metal is assumed to be zero so that the Scheil equation applies for these elements:  $C_l = C_o(1 - f_s)^{k-1}$ .

The expected precipitation behavior of six alloys in these systems is summarized in Table 1. For examples 3-6 the liquid composition is calculated on the premise that the segregated elements remain in solution and do not precipitate out. The difference between these values and those which may be read in Figure 14 for carbon-saturation gives some idea of the amount of sulfide which must precipitate to avoid super-saturating the liquid. The methods used to obtain these values are described in the next few pages, and are followed by a few comments on dilute solution growth and the effect of a large temperature range for precipitation in the "Growth Factors" section.

Example 1: If the initial composition of the melt is 3.5% C, 2.6% Mn, and 0.65% S, substantial amounts of solid sulfide are expected to start precipitating as the temperature falls below 1550°C. Such an alloy is almost at a composition inside the miscibility gap in the pure system. With

TABLE 1

Example	$C_i$	$Mn_i$	$S_i$	$Si_i$	$f_s$	$C_l$	$Mn_l$	$S_l$	$Si_l$	Comments
1	3.5	2.6	0.65	-	-	-	-	-	-	Slag formation followed by considerable primary solid
2	-	2	0.5	8	-	-	-	-	-	MnS precipitation
3	1.75	2.6	0.15	-	0.8	3.25	5.88	0.75	-	MnS should precipitate before 80% solid
4	3.45	0.8	0.07	-	0.35	4.30	1.0	0.1	-	MnS should precipitate before 35% solid
5	-	1.0	0.05	8	0.9	-	3.2	0.5	13.5	MnS should precipitate before 90% solid
6	0.45	0.6	0.06	0.45	0.9	1.0	1.9	0.6	1.0	Borderline between early precipitation of individual particles

Subscripts: "i" = initial composition, wt. %,

"l" = liquid composition at  $f_s$  if MnS does not precipitate out

$f_s$  = fraction solid

3.5% C present it has a solubility nearer to that in Figure 14 and will probably reject some sulfide as slag before dropping below the miscibility gap. Solidification of the iron phase will begin about  $1225^{\circ}\text{C}$  and continue until 25% is solid and the Fe-Fe<sub>3</sub>C eutectic is reached. Following a diagonal line through 2.6% Mn and 0.65% S in Figure 14 yields a final composition in the liquid of 1.75% Mn and 0.03% S. This is not strictly a correct action since 3.5% C is not a saturation level of carbon, but it does serve to give an idea of the extent of sulfide precipitation which may occur in such a system.

Example 2: If substantial initial levels of manganese and sulfur are present the course of events described under Example 1 should also occur for high silicon alloys. A representative composition could be 8% Si, 2% Mn, and 0.5% S.

Example 3: Consider an initial composition of 1.75% C, 2.6% Mn, and 0.15% S. Solidification of the iron phase will be primarily determined by the Fe-C binary. Freezing will begin about  $1400^{\circ}\text{C}$ , and at  $f_s = 80\%$  the temperature will be approximately  $1250^{\circ}\text{C}$ . For sulfur,  $k_s = 0$  is a reasonable approximation based upon the effect of manganese<sup>70</sup>, and low solubility in the  $\gamma$  phase. The effect of Mn and S on  $k_c$  is probably relatively small, and is ignored. The partition ratio of manganese is difficult to estimate, being a function of temperature as well as the concentrations of C and S in both liquid and solid. Segregation for  $k = 0$ , and  $k = 1$  will

be calculated, as well as for  $k = 0.5$  which probably is a useful mean value. When solidification is 80% complete, the liquid will have approximately the following composition:

$$\begin{array}{ll} C = 3.25\% & \text{Mn} = 13.2\% \text{ for } k_{\text{Mn}} = 0 \\ S = 0.75\% & \text{Mn} = 5.88\% \text{ for } k_{\text{Mn}} = 0.5 \\ & \text{Mn} = 2.60\% \text{ for } k_{\text{Mn}} = 1 \end{array}$$

It may be seen that even without carbon, segregation of manganese and sulfur would have caused the liquid to intersect the region of solid sulfide formation. Carbon is expected to increase the formation of sulfide by moving the  $L_m + Q$  surface nearer the iron corner. At  $1250^\circ\text{C}$ , carbon-saturated iron with the initial, unsegregated manganese content (2.6%) could only dissolve about 0.05% S. The unsaturated carbon level reached here will allow somewhat higher sulfur solubility. Nevertheless, it is clear that based on the assumptions made, that solid MnS should begin to precipitate significantly before 80% of the iron has frozen.

Example 4: Consider an initial composition of 3.45% C, 0.8% Mn, 0.07% S. With the same assumptions the iron will begin to freeze at  $1250^\circ\text{C}$ , and will reach the Fe-Fe<sub>3</sub>C eutectic at  $1150^\circ\text{C}$  with 35% solid. This is sufficiently close to carbon saturation for present purposes. Other compositions will be:

$$S = 0.1\% \quad \text{Mn} = 1\% \text{ for } k_{\text{Mn}} = 0.5.$$

According to Figure 14, the maximum solubility of sulfur at this manganese level and temperature is about 0.03 percent.

An alloy of the given initial composition should therefore precipitate solid MnS slightly before reaching 35% solid. If the inclusions are not pushed ahead of the growing iron dendrites, some of them should be found in the dendrite arms. The latter should be surrounded by Fe-Fe<sub>3</sub>C eutectic containing more of the sulfides.

Example 5: Consider an alloy containing 8% Si, 1% Mn, 0.05% S. The problem again arises of the joint effect of Si, Mn and S, on the various partition ratios. Ainslie and Seybolt<sup>51</sup> have determined a function for the solubility product of Mn and S in iron containing 3.25% Si which indicates that the effect of silicon on solid solution behavior is not drastic. The absence of drastic changes in partition ratios is assumed here. The partition ratio of silicon changes with temperature, from 0.67 at 1500°C to 0.9 at 1300°C. Correct use of the Scheil equation would require repeated calculations over small intervals to allow for these changes. However, the other assumptions made do not warrant such precision here. An effective, or mean, value of  $k_{Si} = 0.8$  is therefore used. Similarly,  $k_{Mn} = 0.5$  is again assumed, along with  $k_S = 0$ . The calculated values of liquid composition at 90% solid are:

$$Si = 13.5\% \quad S = 0.5\% \quad Mn = 3.2\%$$

Sherman's<sup>69</sup> research indicates that at 1600°C the effect of 8.5% Si on the activity coefficient of sulfur is the same as that of carbon saturation of the melt. The correspondence

between activity coefficients and solubility, especially for different elements over a range of temperature, is by no means direct. Nevertheless, the tendency for a melt containing 13.5% Si to precipitate MnS should be approximately as great as one saturated with carbon. The alloy under consideration would therefore be expected to precipitate solid MnS before reaching 90% solid.

Example 6: When both Si and C are present their effects should combine or add in some complex manner. An alloy containing 0.6% Mn, 0.06% S, 0.45% C, and 0.45% Si will be considered. Carbon content will be the dominant element in determining the fraction solid and freezing temperatures. Other values of  $k$  are assumed the same as before. At 90% solid, these approximations imply a liquid composition of:

Si = 1%      C = 1%      Mn = 1.9%      S = 0.6%

These sulfur and manganese levels would place the liquid just on the primary iron side of the eutectic in the pure Fe-Mn-S system. One percent each of carbon and silicon can be estimated to increase the activity of sulfur in the melt by approximately 50 percent. The model is not sensitive enough to predict whether sulfide will begin to precipitate at 90% solid in this alloy, or whether it will form as a pseudo-binary eutectic or as individual particles.

Summary: The effects of microsegregation on the liquid composition are considered for specific cases. This is compared with information on the limits of sulfur solubility at the carbon and silicon level reached by the melt. Predictions are made as to when solid sulfide will precipitate.

## 2. Growth Factors

An additional feature of systems containing carbon and silicon which is expected to have an effect on sulfide morphology is the expanded temperature and composition region over which solid sulfide can form. At compositions represented in Figure 15, for example, MnS can begin to precipitate at 1550°C, and then continue to precipitate until the Fe-Fe<sub>3</sub>C eutectic is reached at about 1150°C. The composition of the liquid can vary from about 0.25% S down to a very dilute 0.02%. Miller and Chadwick<sup>78</sup> have recently shown how dilute solutions can affect the morphology of a solid phase growing in a liquid. They showed that there is a smooth transition from rounded dendrites growing in a concentrated solution to a faceted morphology as the solution becomes more dilute, even in the case metal systems such as aluminum dendrites growing into a tin-rich melt. They concluded that this is the result of lowered adatom population at the interface in the dilute solution. Faceted growth is commonly observed in non-metallic materials. Saratovkin<sup>79</sup> has studied a number of non-metallic systems and proposed a mechanism for faceted growth. He believes that impurity solute buildup on singular surfaces causes preferential growth in close-packed directions. He also investigates the transition from dendritic to crystallite growth. Jackson and Hunt<sup>82</sup> have related the curvature or flatness of a growing interface to the entropy of fusion, which is related in turn to the density



of atoms at the interface. Finally, in considering the morphologies which actually result, Cahn<sup>83</sup> has pointed out that the mode of propagation at a moving interface is determined by the magnitude of the driving force and may not be the same as the equilibrium form. These factors are expected to produce more faceted sulfide structures in the systems under consideration than in the pure system because carbon and silicon cause the remaining liquid to be more dilute in sulfur.

For a given cooling rate, primary sulfides precipitating in a system containing significant amounts of carbon or silicon will spend more time in the liquid region than will the corresponding morphology in the pure system. Kattamis, Coughlin, and Flemings<sup>80</sup> have shown that coarsening is a common, if not universal phenomena occurring during solidification. Along with overall precipitation of material a constant redistribution is occurring from high energy to low energy sites. Generally this occurs from areas with a high surface curvature to those of low curvature. The result is that some dendrite arms are melted off, and larger formations are favored over smaller ones, causing a coarsening of the structure. This effect is expected to cause a significant variation in morphology of sulfides forming in the high carbon and silicon melts.

## V. EXPERIMENTAL PROCEDURE

### A. General Procedure

The fifty-gram specimens were melted in alumina crucibles in a vacuum induction furnace. One-half an atmosphere of helium was introduced into the chamber above 1200°C to decrease the loss of volatile elements. The cooling rate was varied by solidifying with reduced induction power or by lifting the crucible out of the graphite susceptor. A range of cooling rates in the same ingot was obtained by adding 500 grams of metal to the crucible, instead of 50 grams, and surface chilling the melt by means of a water-cooled tube with the induction power on.

The specimens obtained as described above were cut up for polishing and metallographic examination. Sections were submitted for quantitative analysis. In a few cases small test bars were machined out of the ingot, broken, and examined with a scanning electron microscope.

The experimental procedure is described in more detail in the following sections.

### B. Experimental Setup

A Balzers VSG 10 vacuum induction furnace was used to make the specimens, with an experimental setup similar to that employed by Kattamis and Flemings<sup>86</sup>. A graphite susceptor was used to aid in melting and reduce stirring. Cylindrical alumina crucibles 1 3/8 x 1 1/8 x 6 inches in size were used throughout. One of these crucibles was submitted for spectrographic analysis of its calcium content. The

reported composition was 0.001% Ca. This is expected to be a good measure of the purity of the crucibles.

The temperature of the melt was continuously measured by means of platinum-platinum/10% rhodium thermocouples. These were protected in the melt by means of 1/4 x 5/32 x 6 inch alumina tubes, closed at one end. The thermocouple tip was supported at 1/2 inch above the bottom of the ingot by placing a piece of alumina of that length in the bottom of the protection tube. Temperature was recorded by means of a Moseley two-pen recorder. The temperature reading was frequently confirmed by means of a potentiometer which had been checked against a standard cell. The readings usually agreed within the width of the recorder ink line ( $\pm 5^{\circ}\text{C}$ ).

Alloying additions were made to the melt by means of a moveable rod through the top of the furnace from which the pieces to be added were suspended by an iron wire. A hook was used to lift out of the susceptor a molybdenum wire basket containing the crucible with alloys which were to be rapidly cooled. For even faster cooling, and for obtaining a range of cooling rates in the same specimen surface chilling was accomplished by means of the water-cooled tube.

### C. Materials Used

Ferrovac-E was used throughout as the source of iron. The analysis of this iron is given in Appendix C.

Powdered commercially available manganese sulfide was used

at first as one source of manganese and sulfur. However, it was found that this powder contained at least 10% oxygen which probably formed by decomposition in the air. Available sources of FeS were similarly unacceptable. Iron-sulfur and iron-manganese master alloys were therefore prepared. Sulfur dissolves very readily in molten iron. This fact was utilized to make the Fe-S master alloys. The iron was simply melted under 3/4 atmosphere of helium, and powdered sublimed sulfur was then dumped onto the surface. Considerable evolution of sulfur vapor occurred, but master alloys containing up to 20% sulfur were successfully prepared in this manner. The oxygen content of one of these master alloys was found to be 0.026%, indicating that contamination by oxygen is very low. A 50% Fe-Mn master alloy was also prepared, using Ferrovac-E and Johnson Matthey spectrographically standardized manganese.

Iron-carbon master alloys were also prepared, using Ferrovac-E and powdered graphite. Silicon metal was added as pieces of Alfa Inorganics' high purity silicon wafers. The source of oxygen was reagent grade  $\text{Fe}_2\text{O}_3$  powder. Aluminum metal used for deoxidation was reagent grade wire.

#### D. Experimental Procedure

Desired amounts of the master alloys were cut up and surface-ground to remove most of the surface contamination. The pieces were then briefly etched in concentrated hydrochloric acid, washed in water, and dried with acetone. They were then immediately placed in the crucible and into the

furnace or suspended from the moveable rod in the furnace for later addition to the melt. A vacuum of about one-tenth of a micron was then obtained by means of the diffusion pump. Induction power was increased gradually to avoid the possibility of breaking the crucible. When  $1200^{\circ}\text{C}$  was reached volatilization of some of the elements in the crucible usually caused a slow rise in the attainable vacuum. The chamber was back-filled with half an atmosphere of helium to decrease the rate of loss. When  $1650^{\circ}\text{C}$  was reached the manganese was added along with the deoxidizer. In the case of carbon-deoxidized alloys the chamber was briefly pumped down to 1000 microns to obtain a carbon boil, and then back-filled again with helium.

Homogenization of the liquid was found to occur rapidly in these small and strongly stirred melts. Cooling down to the quench or holding temperature was generally undertaken after only two or three minutes at  $1650^{\circ}\text{C}$ .

#### E. Chemical Analysis

Sections of the ingots were submitted for quantitative analysis. These were generally in the shape of a section of pie in order to average the effects of any macrosegregation which occurred.

Oxygen analysis was performed by the inert gas-fusion method. The aluminum content was determined by the color method using aluminon color reagent. Sulfur was measured by evolution

in an induction furnace. Manganese was determined by a volumetric measurement, silicon by gravimetric silica determination, and carbon by means of a carbon analyser or gravimetric measurement.

It should be pointed out that because of the rapid stirring of the melt slag particles often did not float to the surface when the miscibility gap was intersected. Some of these particles were entrapped and were doubtless included in the analysis of the liquid metal phase, giving an incorrectly high value for the composition on the edge of the miscibility gap. The same holds true for the large MnS dendrites. As a result the manganese and sulfur analyses of alloys which fall in the miscibility gap will usually be higher than the equilibrium value. This problem does not arise when the primary MnS phase does not form.

#### F. Fractography

Small test bars 1.0 x 0.125 x 0.03 inches were machined from the ingots of several alloys and were pulled to fracture with an Instron tensile testing machine. All were tested in the as-cast condition. The primary purpose of breaking the test bars was to obtain fracture surfaces for examination with a scanning electron microscope. The significance of the structures observed is discussed in Chapter VII.

## VI. EXPERIMENTAL RESULTS

### A. Introduction

In this section, the experimental dependence of sulfide inclusion morphology on chemical and thermal parameters is reported. Interpretation of these results and comparison to the solidification models developed in Chapter IV will be made in the next chapter. This section is divided into three parts. Part B, "Chemical Effects," summarizes all the morphological variations found in the specimens made without distinguishing the effects of cooling rates, undercooling, or the temperature at which alloying additions to the melt were made. In Part C, "Thermal Effects," appropriate pairs or groups of alloys are selected from Part B to show the effects of different thermal parameters on specimens of the same composition. Since Yarwood<sup>31</sup> found in the related Fe-O-S system that cooling rates over two orders of magnitude have little effect on sulfide morphology or distribution, this organization should be preferable to one which classifies the data primarily on the basis of thermal history.

A classification basically similar to that first proposed by Sims<sup>5</sup> will be used to describe sulfide morphology. However, the definitions used here are made without regard to composition, mode of formation, or position in the matrix, but are based only on the final shape or morphology. This is done in order to separate cause and effect and to avoid con-

fusion caused by prejudging the mode of formation from the morphology.

The cross-section of an inclusion as it appears on a polished section may give a false impression of the actual three-dimensional configuration. For example, rod-like inclusions may look like spheres in cross-section, or a low-angle cross-section of an intergranular sheet may look like a very large bulky inclusion. The actual shapes of the inclusions are determined by polishing-down, by scanning electron microscope pictures of fracture surfaces, or by reference to previous experimental determinations near the same composition. The inclusions are then classified according to type. In some cases the morphology may not fit clearly into one type or another but somewhere between. When appropriate, such transition morphologies are denoted by a slash mark between the two nearest types. For example, Type I/III would describe an inclusion which was neither as smoothly curved on the surface as ideal Type I, nor as sharply angular as Type III. Despite the limitations of any classification system, some such device is a useful shorthand for describing inclusion morphology.

The inclusions studied in this work will be classified according to morphology as follows: Type I inclusions are approximately spherical or ellipsoidal in shape. Type II S inclusions are sheets or films of sulfide. Type II R are rod-like. Sims<sup>9</sup> associated both types with eutectic precipitation and greatly reduced impact strength, and classified them both



as Type II. In order to maintain the present morphological basis for classification while avoiding the confusion of deviating from accepted practice, the two forms have been differentiated by the postscript rather than assigned different numerals. Type II F inclusions are groups of platelets which appear to be related crystallographically. Type III inclusions are here defined as sharply angular inclusions with planar or nearly planar surfaces. Type D inclusions are dendrites of MnS.

In assigning particular specimens in Section B to subgroups such as the Fe-Mn-S-O system rather than the Fe-Mn-S-(Al deoxidized) system a decision had to be made as to what constitutes "deoxidized". Various criteria such as 0.02% O, or an O/S ratio of less than 0.01 were considered. Neither criterion was satisfactory. The first failed to allow for variations in sulfur or manganese levels, while the second ignored the important effect of the Mn/S ratio on morphology. A satisfactory method for deciding if a specimen contained sufficient oxygen to place it in the quaternary Fe-Mn-S-O system was to examine the inclusions for oxide. Yarwood's research demonstrated that FeO was clearly distinguishable from FeS. MnO is considerably darker than MnS and is easily distinguishable. In any case, the borderline between "deoxidized" and "oxygen bearing" is a matter of definition and convenience. The oxygen level at which visible oxide disappears corresponds generally to the level which other workers have considered "deoxidized".

## B. Chemical Effects

### 1. The Fe-Mn-S-(Aluminum Deoxidized) System.

The compositions of nine specimens which fall into this system are presented in Table 2.

The structure present in 5-21 is similar to that found by Yarwood at low sulfur and O/S levels, except that no oxide was visible even at 1000 X (Figure 16a). Alloy 29-1 contained a fine rod-like Type II R, together with borderline I/III inclusions which were neither spheroidal nor sharply angular Type III's (Figure 16b). A few spherical Type I morphologies were also observed, plus some small dendrite structures. In Alloy 29-2 the Type II R inclusions again predominate. However, several very large and extensive dendrites are also present, together with numerous Type I inclusions consisting of MnS with included iron (Figures 16c, 16d). The I/III inclusions in 29-1 and the D and I inclusions in 29-2 tend to occur in clusters in several parts of the ingots. In specimen 5-26 the typical II R inclusions predominate, but a roughly serrated version of Type II S consisting of a duplex structure of FeS and MnS or Q sulfide also appears (Figure 17a). Figure 17b shows the combination of fine II R, small D, and iron-including Type I inclusions found in Alloy 8-13. Such clusters of D and I inclusions are often, but not always, found near the top surface of the specimen. They are least often found near the middle of the ingot. Figure 17c shows more detail of a typical Type I inclusion in this system. Figure 17d shows that small

TABLE 2.

Alloy	Mn	S	O	Al(sol)	Al(insol)	O/S	Type
5-21*		0.10	0.009			0.09	I, IIS
29-1	3.22	0.40					IIR, I/III, I, D
29-2	3.72	0.45					IIR, D, I
5-25	1.50	0.51	0.0046	0.053		0.009	IIR
5-26	1.30	0.78	0.058	0.018	0.011	0.08	IIR, IIS
8-13	3.18	0.82	0.0016	0.059		0.002	IIR, D, I
5-30	1.42	0.87	0.029	0.008	0.005	0.03	IIR, IIS, D
5-27*	0.02	1.41	0.043	0.002	0.004	0.03	IIS, I
32-1	2.81	0.72	0.0018	0.074			IIR, D

\* Aluminum was not added to these melts. However, since they do not properly fit into the Fe-Mn-S-O system or the carbon-deoxidized system they have been included here.



Figure 16: Photomicrographs of sulfide inclusions found in the aluminum deoxidized Fe-Mn-S system. Table 3.

- a) Alloy 5-21: Coexistence of Type I and II S inclusions at low sulfur and manganese levels. Dark areas are holes, 500X.
- b) Alloy 29-1: Type II R and I/III morphologies which formed when the manganese was added below the freezing temperature of MnS, 200X. 3.22% Mn, 0.40% S.
- c) Alloy 29-2: Type II R and coarse Type D which resulted from holding .8 minutes in L + Q temperature range, 200X.
- d) Alloy 29-2: Type I inclusions found in same specimen, 200X. 3.72% Mn, 0.45% S.

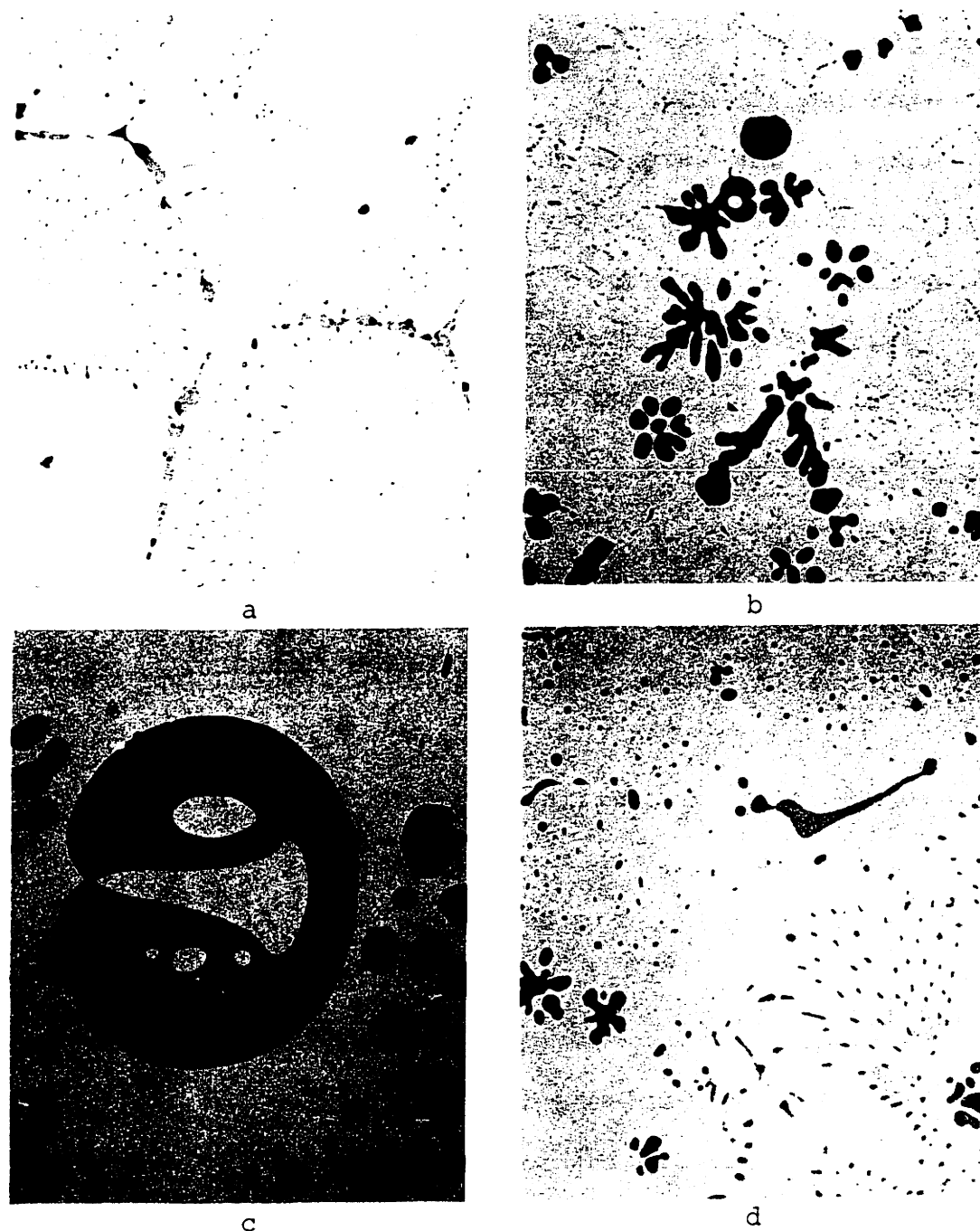


Figure 17: Photomicrographs of sulfide inclusions found in the aluminum deoxidized Fe-Mn-S system. Table 3.

- a) Alloy 5-26: Type II R inclusions plus serrated Type II S duplex inclusions containing FeS and Q sulfide, 200X. 1.3 Mn, 0.5 S.
- b) Alloy 8-13: Coexisting II R, I, and D inclusions, 200X.
- c) Alloy 8-13: Detail of a typical large Type I inclusion found in this system, showing included iron, 500X. 3.18 Mn, 0.82 S.
- d) Alloy 5-30: Coexisting II R, II S, and D inclusions, 200X. 1.3% Mn, 0.87% S.

amounts of the II S Type of inclusions can be found together with II R and a stubby dendrite form, in Alloy 5-30. The appearance of 5-27 is similar to that of 5-21, except that a larger volume percent of inclusions is present. A serrated duplex Type II S was found in this system when the Mn/S ratio was near to or less than the stoichiometric value. An example is shown in Figure 18b. Alloy 32-1 contains MnS dendrites which extend through large volumes of the melt, together with a rod eutectic (Figure 18c).

## 2. The Fe-Mn-S (Vacuum-carbon Deoxidized) System

Twelve specimens fall under this classification. Their compositions and the resultant morphologies are listed in Table 3.

Figure 19a shows the intermediate Type I/III morphology observed in Alloy 29-3, along with a fine II R form. A typical structure seen in these alloys is presented in Figure 19b. This is a photomicrograph of 8-7, and shows the appearance of the II R, D, and I inclusions. Manganese sulfide dendrites were observed in Alloy 8-11 in close proximity to the large spherical droplets and the II R phase (Figure 19c). Typical rod inclusions formed when the initial composition of the melt is in the Fe + L<sub>m</sub> + Q region are shown in Figure 18d. The morphology of II S inclusions at high sulfur and low oxygen levels in the nearly pure Fe-FeS system is seen in Figure 20a. Specimen 8-1 contained some excellent examples of dendritic morphology, with tertiary arms visible (Figure 20b).

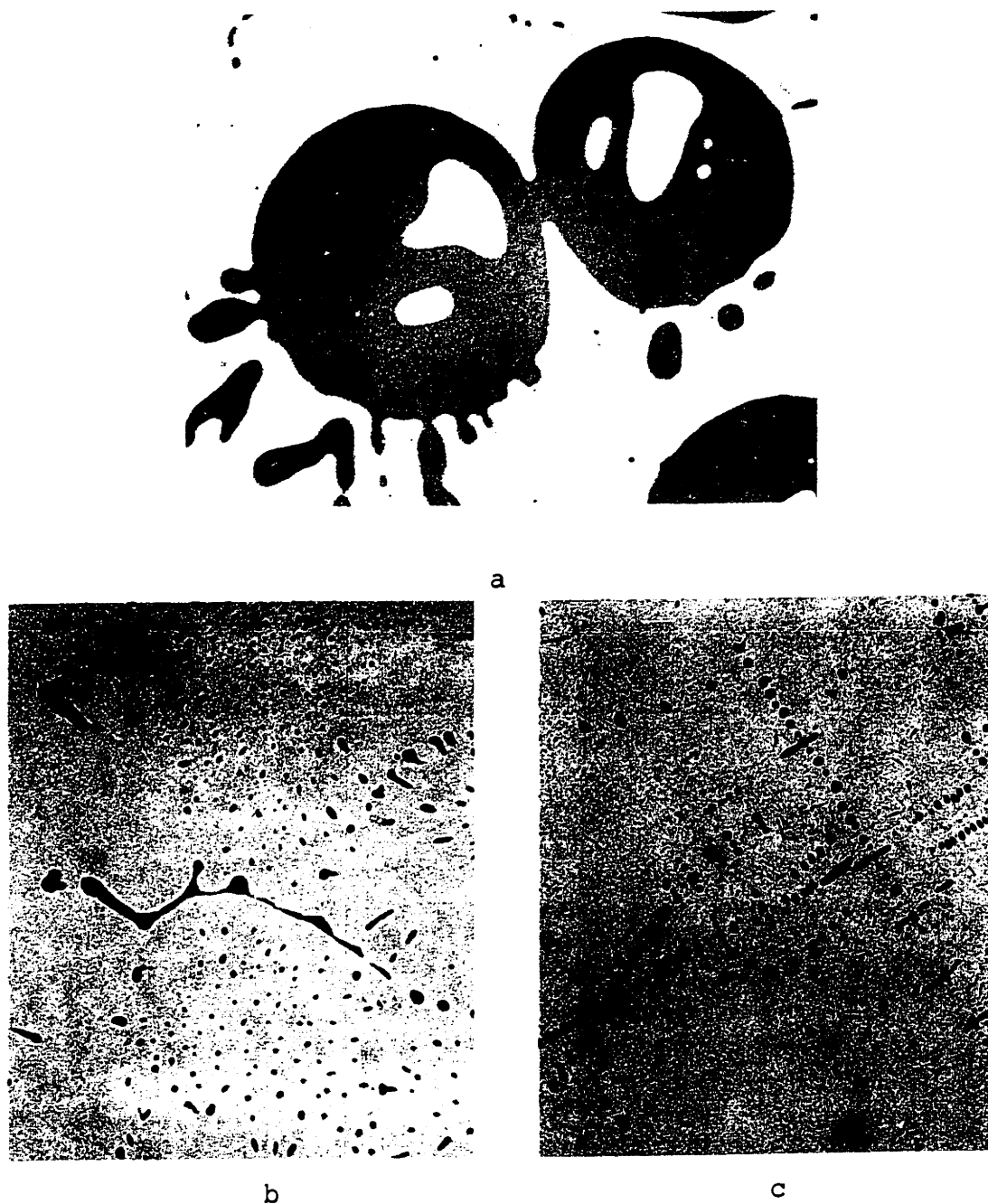


Figure 18: Photomicrographs of sulfide inclusions found in the aluminum deoxidized Fe-Mn-S system. Table 3.

- a) Alloy 29-2: Shows dendritic extensions from slag drop-let, 500X.
- b) Alloy 5-30: Type II S duplex inclusions formed at  $Mn/S = 1.65$ , together with Type II R inclusions, 200X. 1.42 Mn, 0.87 S.
- c) Alloy 32-1: Extensive dendritic sulfides, together with Type II R, formed when manganese was added to a melt containing almost 3% S, in L + Q temperature range, 100X. 2.81% Mn, 0.72% S.

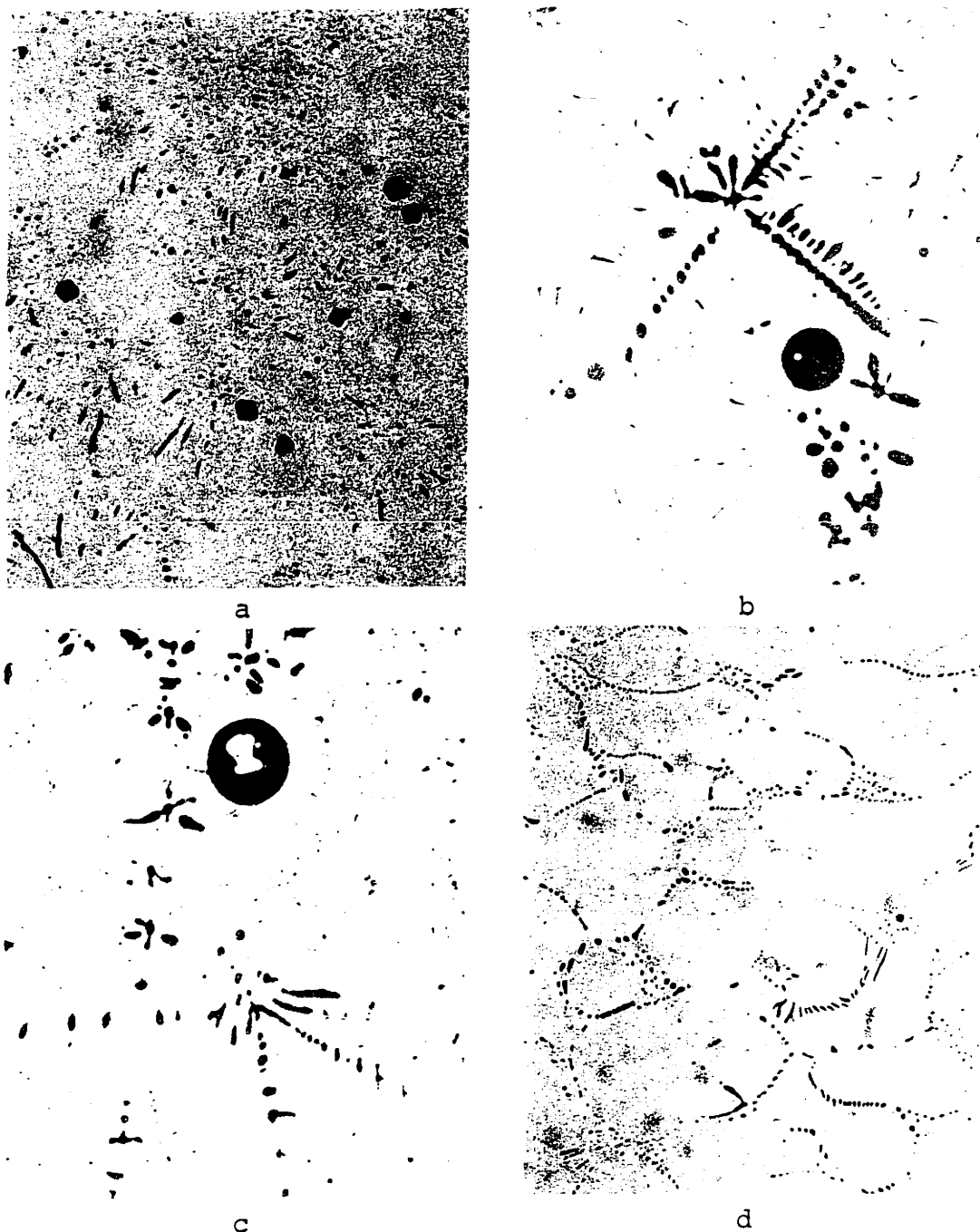


Figure 19: Photomicrographs of sulfide inclusions found in the vacuum-carbon deoxidized Fe-Mn-S system. Table 3.

- a) Alloy 29-3: Type II R and I/III inclusions which formed when the manganese was added below the melting temperature of MnS, 200X. 3.64% Mn, 0.77% S.
- b) Alloy 8-7: Coexistence of Type II R, D, and Type I inclusions typically found in this composition range, 200X. 2.03 Mn, 0.78 S.
- c) Alloy 8-11: Another example the same structure, 200X.
- d) Alloy 8-4: Composition initially in Fe + L<sub>m</sub> region on manganese-rich side of phase diagram, 250X. 1.13% Mn, 0.42% S.



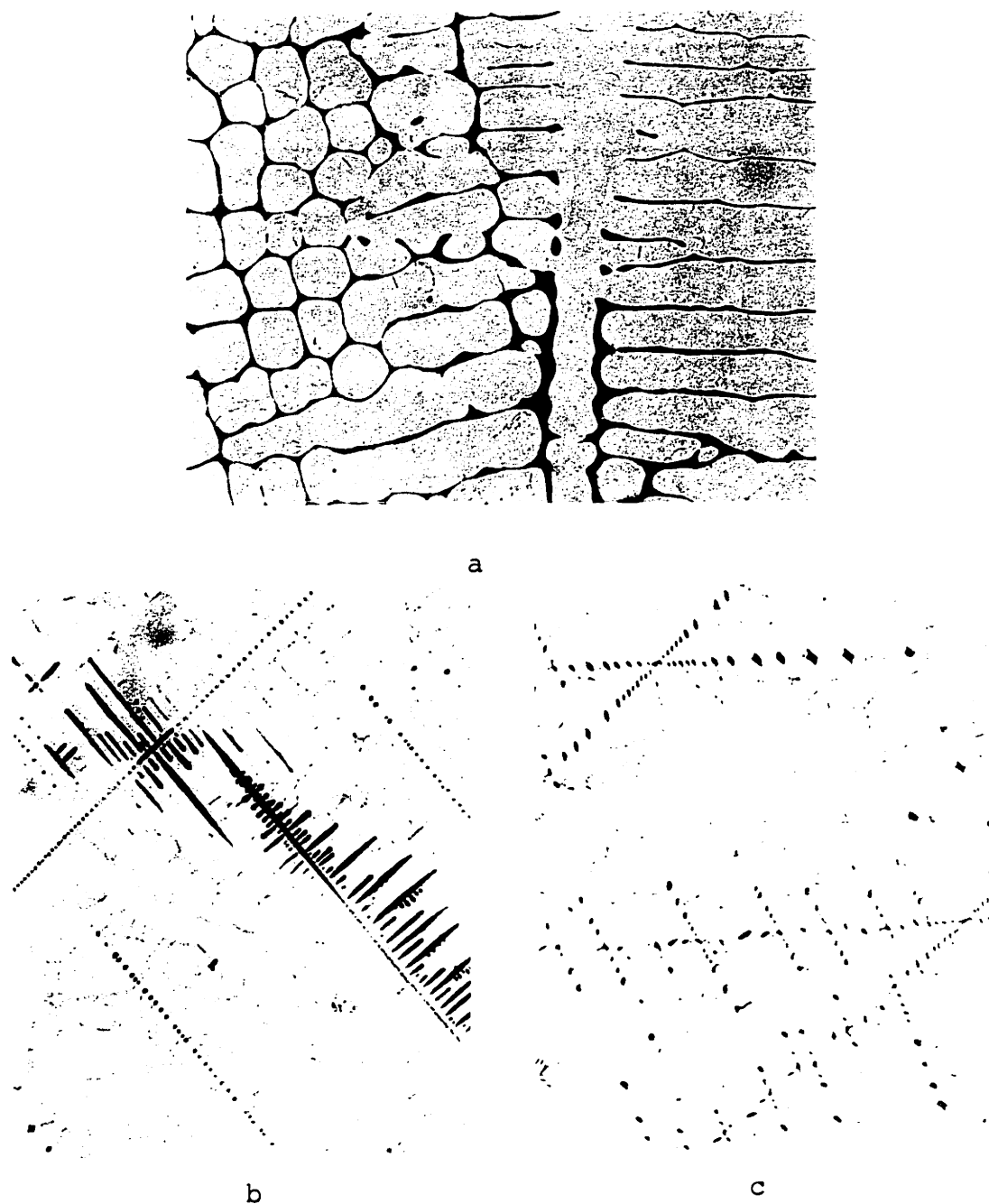


Figure 20: Photomicrographs of sulfide inclusions found in the vacuum-carbon deoxidized Fe-Mn-S system. Table 3.

- a) Alloy 8-6: Sheet-like Type II S sulfide formed at high sulfur levels in the absence of manganese, 100X. 0% Mn, 1.83% S.
- b) Alloy 8-1: Type II R and dendritic sulfides formed when manganese is added to a melt containing approximately 3% S at a temperature just below the L + Q monotectic, 100X.
- c) Alloy 8-1: Another dendrite with a different orientation, 100X. 2.81% Mn, 1.87% S.

TABLE 3.

Alloy	Mn	S	O	C	Other	O/S	Type
8-2	4.51	0.37	0.0009	0.036		0.003	IIR, I, D
29-3	3.64	0.77	0.0018	0.084		0.002	IIR, I/III
8-4	1.13	0.42	0.0027	0.014		0.006	IIR
8-7	2.03	0.78	0.0049	0.020		0.006	IIR, I, D
8-5	4.90	1.01	0.0029	0.023		0.003	IIR, I, D
8-8	2.76	1.18	0.013	0.027		0.011	IIR, I, D
8-9	2.07	1.22	0.0059	0.077		0.005	IIR, I, D
8-10	0.93	1.30	0.0041	0.065	Al = 0.006	0.003	IIR, IIS, I
8-11	3.66	1.30	0.0042	0.078	P = 0.003	0.003	IIR, I, D
8-1	2.81	1.87	0.0027	0.054		0.001	IIR, D, I
8-6	0.00	1.83	0.0073	0.026		0.004	IIS
8-23	0.63	2.62	0.011	0.042		0.004	IIS, IIR, I

Other dendrites in this specimen were apparently very similar to those observed in 32-1, as a comparison of Figure 18c with Figure 20c will show.

### 3. The Fe-Mn-S-O System

The compositions and resulting morphologies of the specimens in this system are presented in Table 4.

Figure 31a shows FeO inclusions in Alloy 5-13, some of which have small areas of included iron. Figures 21b, 21c, and 21d show typical Type I inclusions present in 5-5, 5-7, and 5-6. Some of these clearly have duplex structures. Co-existence of large duplex Type I inclusions and II S inclusions is shown in Figure 22a, a photomicrograph of 5-29. Details of the inclusions are seen in Figures 22b and 22c.

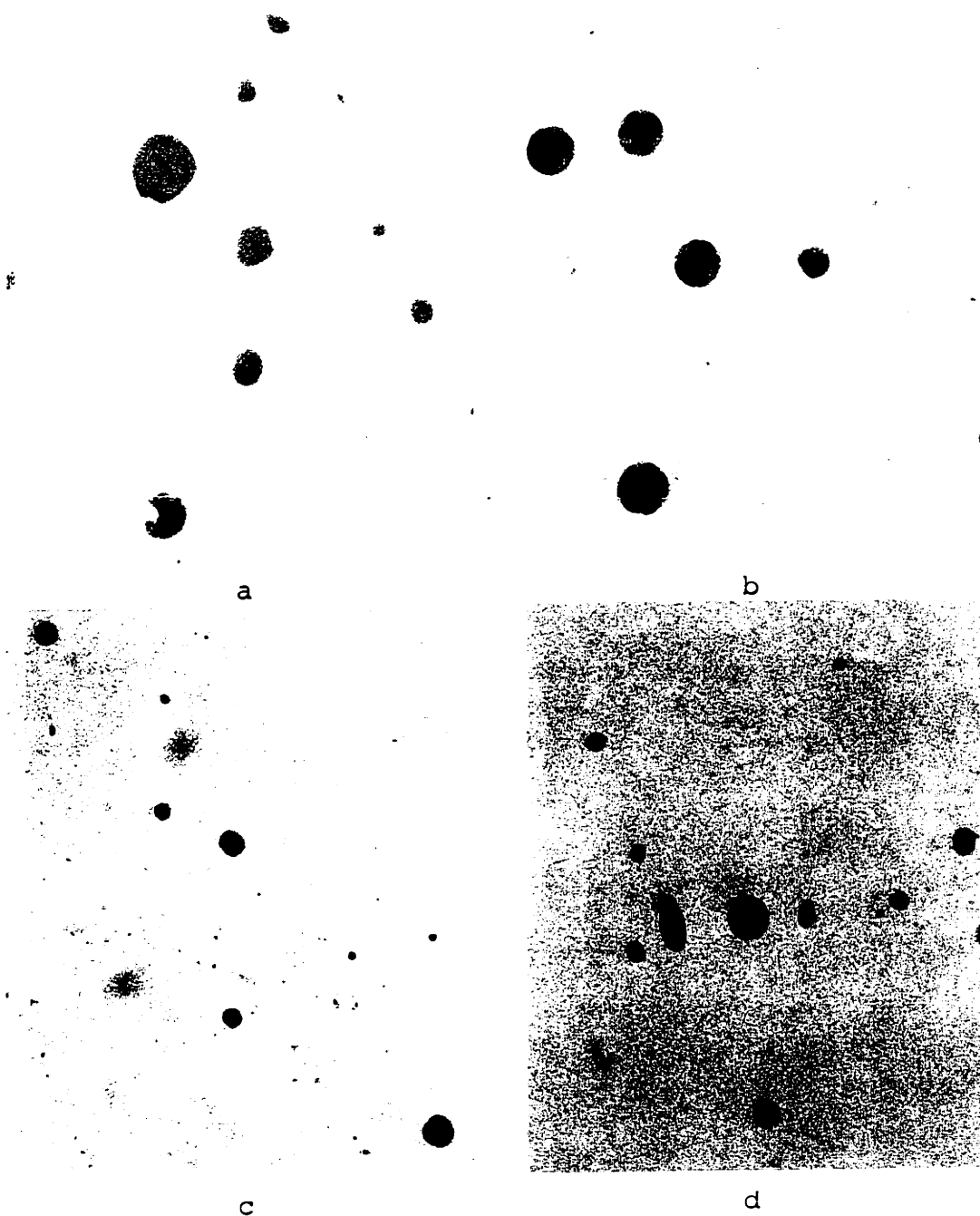
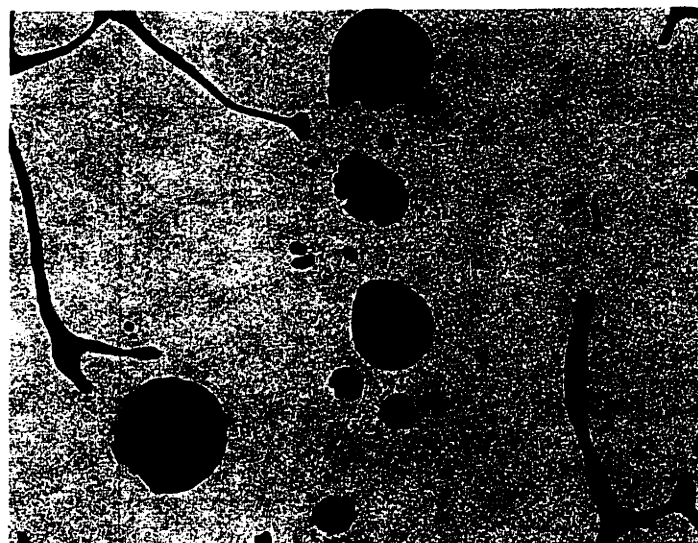


Figure 21: Photomicrographs of inclusions from the Fe-Mn-O-S system. Table 4.

- a) Alloy 5-13: Iron oxide inclusions, one of which is penetrated by iron, 1000X. 0.17% O.
- b) Alloy 5-5: Duplex Type I inclusions of MnO and MnS. Specimen cooled at 1°C/sec. Density of inclusions greater than typical of bulk of specimen. 1000X. 0.12 Mn, 0.07 S, 0.01 O.
- c) Alloy 5-7: Same as Alloy 5-5, but cooled at 8°C/sec., 1000X.
- d) Alloy 5-6: Type I inclusions, 500X. 0.52% Mn, 0.20% S, 0.03% O.



a



b



c

Figure 22: Photomicrograph of inclusions from the Fe-Mn-O-S system. Table 4.

- a) Alloy 5-29: Coexistence of large duplex Type I inclusions consisting primarily of light grey MnS or Q sulfide and Type II S yellow sulfides consisting primarily of FeS, 200X.
- b) Alloy 5-29: Detail of Type II S inclusion above, showing small areas of darker eutectic-like formation, probably containing FeO, 1000X.
- c) Alloy 5-29: Detail of Type I inclusion above, showing dark eutectic-like formation, 1000X. 0.32% Mn, 1.63% S, 0.069% O.

TABLE 4.

Alloy	Mn	S	O	Al(sol)	Al(insol)	O/S	Type
5-13			0.17				I
5-5	0.12	0.07	0.01			0.14	I
5-7	0.12	0.07	0.01			0.14	I
5-6	0.52	0.20	0.029			0.14	I, IIS
5-18		0.67	0.20			0.29	IIS, I
5-28	0.56	1.56	0.033	0.006	0.009	0.02	IIS, I
5-29	0.32	1.63	0.069	0.002	0.001	0.04	I, IIS
5-31	1.89	1.10	0.10			0.09	IIR, IIS, I
5-17		2.78	0.21			0.075	IIS, I
5-19		8.22	0.40			0.05	IIS, I

#### 4. The Fe-Mn-S-C System.

Specimens which fit into this system are listed in Table 5.

TABLE 5.

Alloy	Mn	S	C	O	O/S	Type
26-1	0.83	0.07	3.43	0.003	0.04	III
31-1	2.63	0.15	1.76			III
21-3	2.45	0.24	4.43			III, D
25-2	2.60	0.65	3.66			III, D, I
25-1	2.64	0.66	3.01			D, I, IIF

Type III inclusions are found in all of these specimens except 25-1, where sulfide dendrites extend through large volumes of the melt, and coexist in some areas with the round Type I inclusions containing iron. Typical morphologies are shown in Figure 23, along with brief comments on each.



Figure 23: Photomicrographs of inclusions in the Fe-Mn-S-C system. Table 5.

- a) Alloy 26-1: Various versions of angular Type III inclusions typically seen in this system, 500X. 0.8 Mn, 0.07 S, 3.4 C.
- b) Alloy 21-3: Similar morphologies seen in another alloy, 500X.
- c) Alloy 25-1: Type II F morphology, similar to some also observed in the Fe-Mn-S-Si system, 200X.
- d) Alloy 25-1: Shows that the II F morphology may be connected to coarse Type D inclusions. 2.64% Mn, 0.66% S, 3% C.

A particular morphology found in this system which did not appear in those already discussed is shown in Figures 23c and 23d. The flat sheet-like features of this type of inclusion are somewhat like Type II S. However, they always appeared in clusters bearing a distinct crystallographic relation to each other, which indicates that they may have grown from a single nucleus. Furthermore, they sometimes were observed to grow out of relatively large coarse dendrites (Figure 23d). They have been given the designation II F.

#### 5. The Fe-Mn-S-Si System.

The specimens which contain primarily iron, silicon, manganese, and sulfur are listed in Table 6.

TABLE 6.

Alloy	Mn	S	Si	C	O	O/S	Type
24-1	0.89	0.036	7.97		0.006	0.16	III,
24-2	0.94	0.05	7.97		0.010	0.20	III, IIF
23-2	2.02	0.09	7.60				III,
23-3	1.91	0.11	8.03				III, IIF
30-1	2.62	0.10	8.61				III, IIF
8-19	2.73	0.41	7.41				D, I
8-14	2.04	0.44	7.49	0.063	0.003	0.008	D, III, I, IIF
8-18	3.46	0.49	7.71				D, I
8-15	2.08	0.58	6.76	0.073	0.002	0.004	D, I
8-20	2.01	0.73	8.07				D, III, IIF
27-1	2.58	0.16	7.43		0.018	0.1	I, IIF
27-1	P = 0.004						

Type III inclusions were found in most of these high silicon alloys, except at the higher sulfur levels where dendri-

tic morphologies and the large Type I inclusions with included iron were common. Figures 24-26 show the morphologies observed.

The small black star-like or dust-like particles associated with most of the inclusions in 24-1 and 23-2 are believed to be graphite formed from carbon left over after the carbon boil. They were only observed in these two specimens which were cooled at  $1^{\circ}\text{C}/\text{sec.}$  between  $1490^{\circ}\text{C}$  and  $1350^{\circ}\text{C}$ . Silicon is known to be effective in promoting the formation of graphite in iron.

These high silicon alloys are very sensitive to etching or staining. They generally could not be polished with alumina under distilled water without forming a ring-like pattern such as that shown in Figure 24c. No etch was used to produce this staining. It could usually be avoided by using diamond abrasive in lapping oil, but atmospheric exposure was often sufficient to cause the staining. The Fe-Si phase diagram contains several features which could account for a surface-sensitizing phase change, including a gamma loop, an order-disorder reaction, and a peritectic. The phase change apparently occurs after solidification, and is strain-nucleated. The transformed regions were often observed on both sides of a crack in the brittle specimen or along a scratch caused by rough polishing. For this reason the etch patterns are not useful for outlining the original dendrites. Type III inclusions were usually, but not always, surrounded by one of the stained areas.



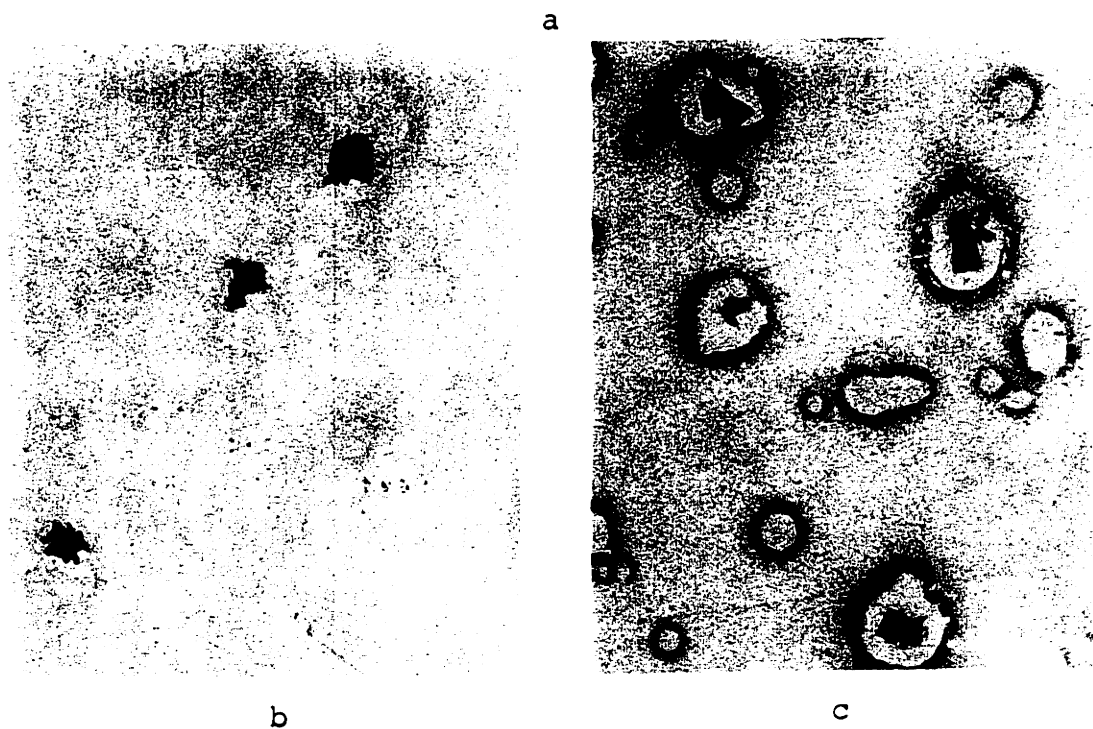


Figure 24: Photomicrographs of inclusions from the Fe-Mn-S-Si system. Table 6.

- a) Alloy 24-1: Type III inclusions, 500X. 0.9 Mn, 0.04 S, 8 Si.
- b) Alloy 23-2: Type III inclusions, 500X.
- c) Alloy 23-2: Type III inclusions and etch pattern caused by unknown factors (see text), 500X. 2% Mn, 0.09% S, 7.6% Si.

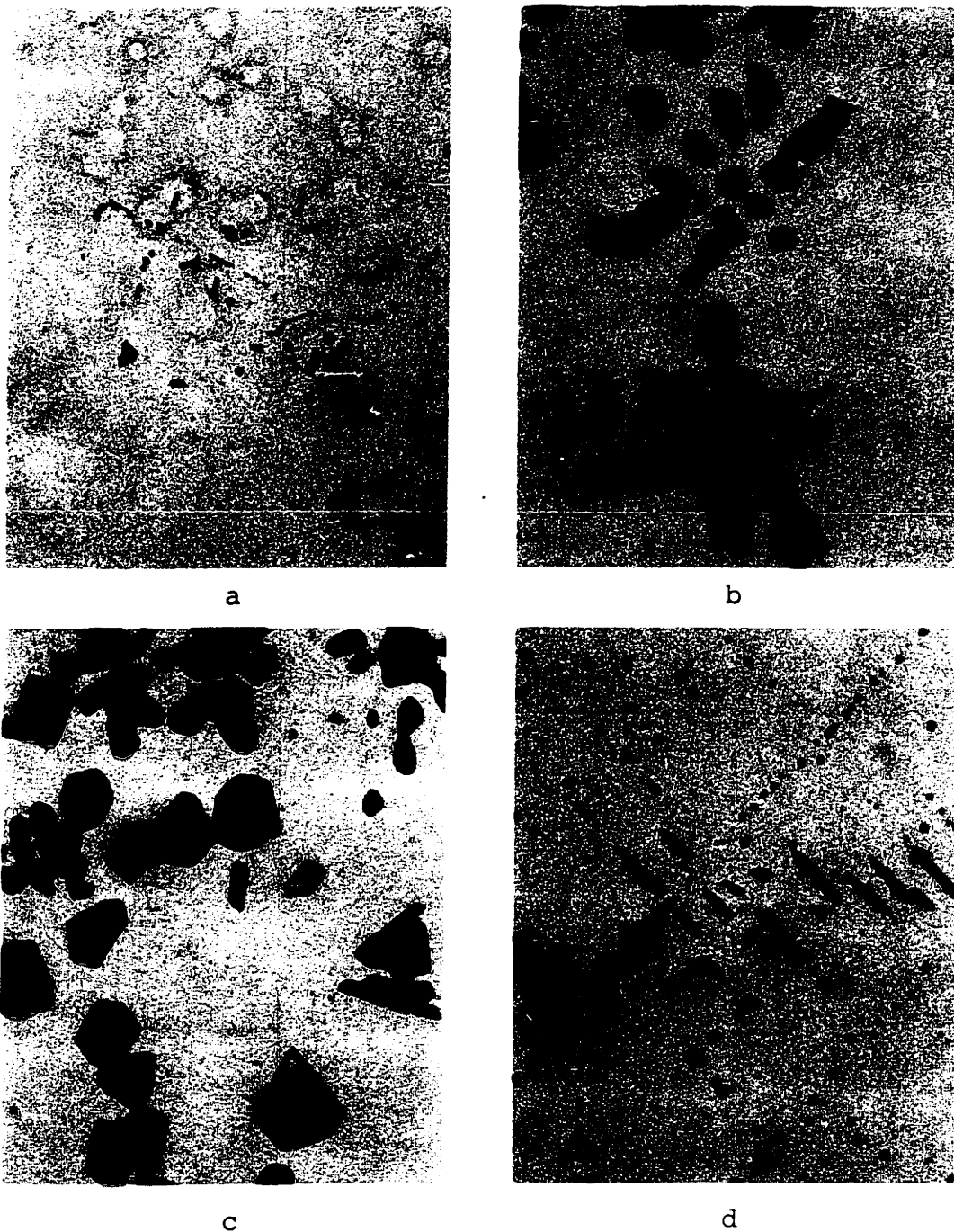


Figure 25: Photomicrographs of inclusions from the Fe-Mn-S-Si system. Table 6.

- a) Alloy 23-3: Type II F morphology, 500X. 1.9 Mn, 0.11 S, 8% Si.
- b) Alloy 8-14: Coarse Type D inclusions in ingot, cooled at 1°C/sec., 500X. 2.04 Mn, 0.44 S, 7.49 Si.
- c) Alloy 8-14: Coarse Type III and Type D inclusions in same ingot, cooled at 1.3°C/sec., 500X.
- d) Alloy 8-15: Fine dendrite MnS inclusions formed in melt cooled at 10°C/sec., 500X. 2.08 Mn, 0.58 S, 6.76 Si.

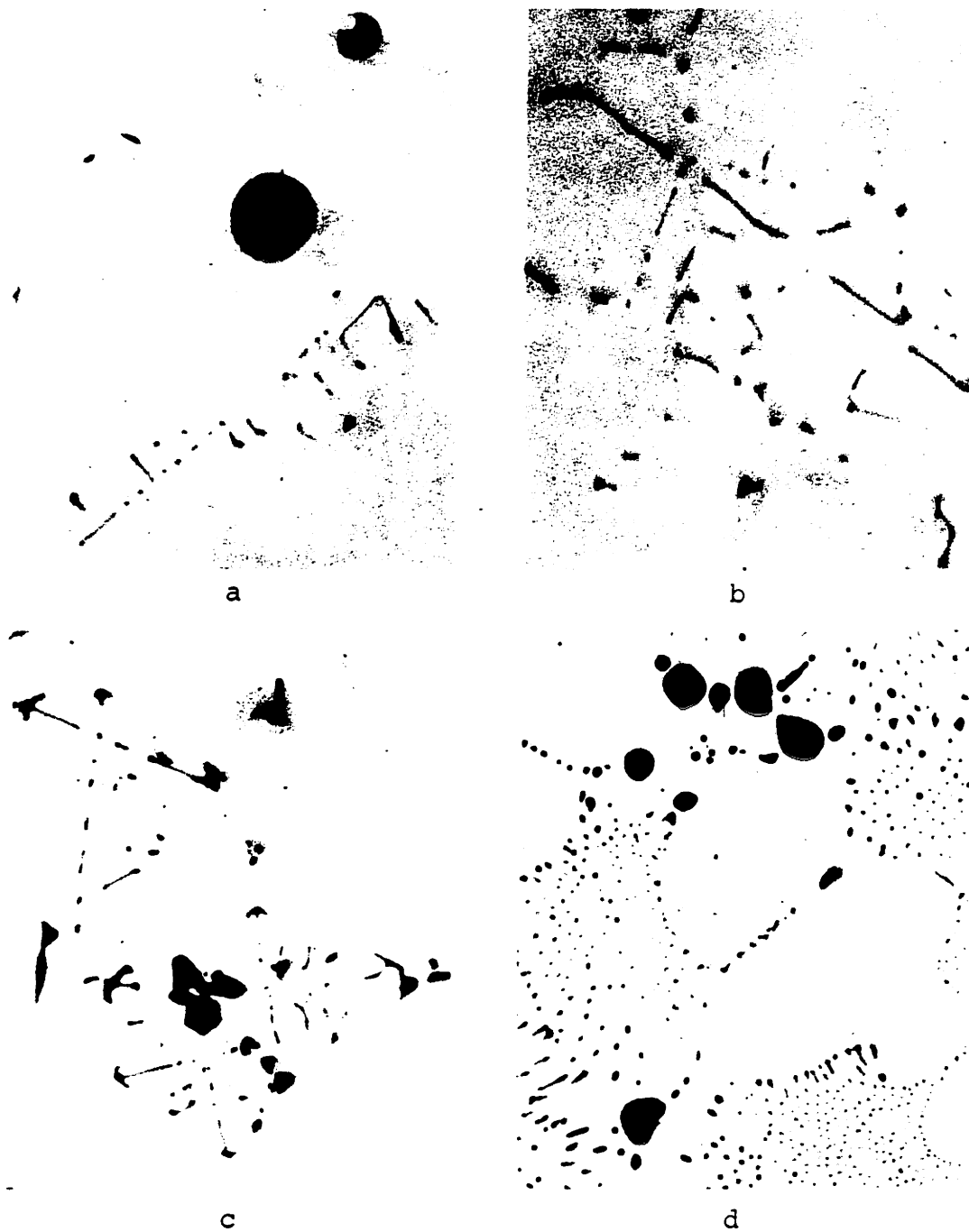


Figure 26: Photomicrographs of inclusions from the Fe-Mn-S-Si system (a,b,c), and from the Fe-Mn-S-Al system (d). Tables 6 & 7.

- a) Alloy 27-1: Type I and II F inclusions may form when oxygen is present, 500X. 2.6 Mn, 0.16 S, 7.4 Si, 0.018 O.
- b) Alloy 27-1: Type II F inclusions, 500X.
- c) Alloy 8-14: Type D and II F inclusions close together, 500X.
- d) Alloy 5-23 (Fe-Mn-S-Al system): Structure resulting from an Mn/Al ratio of 2. Dark  $\text{Al}_2\text{S}_3$  phase has formed, 200X. 1.34% Mn, 0.71% S, 0.73% Al.

Oxygen was deliberately added to 27-1 in order to study the effect on morphology. A number of quite large spherical inclusions resulted (Figure 26a). These possessed a bluish tint, and occasionally contained included iron in small spherical or rod form. The II F morphology was also present (Figure 26b). Silica inclusions were not observed, but a small amount of glass-like slag was present on the surface of the ingot.

#### 6. The Fe-Mn-S-Al System.

Two heats are listed to give a qualitative idea of the effect of aluminum on the sulfide morphology. Their compositions are listed in Table 7.

TABLE 7.

Alloy	Mn	S	Al	O	O/S	Type
5-20		0.09	0.06	0.048	0.53	I, IIS
5-23	1.34	0.71	0.73			IIR, I

Coexistence of the II R MnS inclusions with larger, darker round inclusions consisting largely of  $Al_2S_3$  is shown in Figure 26d. Other morphologies were observed in heats not listed above which are identical to structures reported in the literature.

## 7. The Fe-Mn-S-Si-C System.

Specimens were made in which significant amounts of both silicon and carbon are present. These are listed in Table 8.

TABLE 8.

Alloy	Mn	S	C	Si	O	O/S Al(sol)	Type
28-1	0.59	0.06	0.45	0.46		<0.03	III, IIR
28-2	0.56	0.06	0.41	0.47		0.03	III, IIR
15-1	2.70	0.15	1.56	2.10	0.002	0.013	III, IIF
8-17	1.59	1.16	0.20	2.15	0.005	0.004	IIR, I, D
21-1	2.73	1.25	1.86	1.99			D, I

Type III inclusions found in 28-1 typically appeared as in Figure 27a. Typical examples of the IIR inclusions in this system are shown in Figure 27b. The isolated Type III inclusions of 28-2 appeared to be slightly less angular than in 28-1, but the structures were otherwise identical.

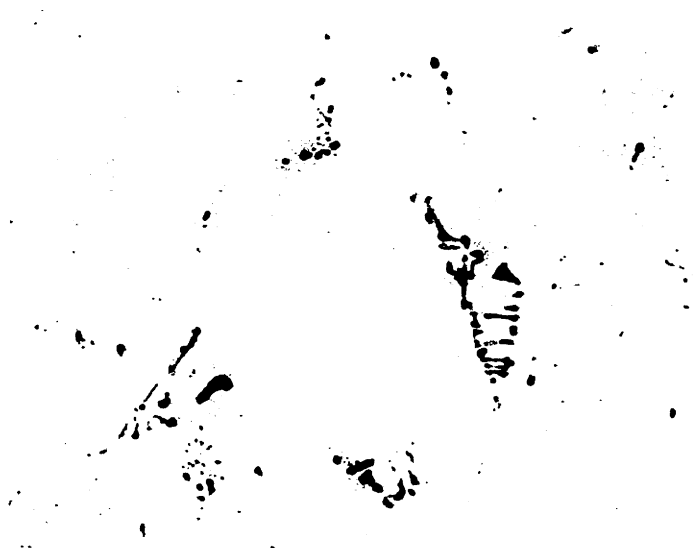
### C. Thermal Effects

#### 1. Introduction

As was described in the section on experimental procedures, several methods were used to control the range of cooling rates in the specimens. Cooling rates in excess of  $10^{\circ}\text{C}/\text{sec.}$  were observed  $3/8"$  from the water-cooled tube in some specimens. The actual rate very near the tube must have



a



b

Figure 27: Photomicrographs of specimens in the Fe-Mn-S-Si-C system. Table 8.

- a) Alloy 28-1: Type III inclusions, 500X.
- b) Alloy 28-1: Type II R inclusions, 200X.  
0.59% Mn, 0.06% S, 0.45% C, 0.46% Si.

been considerably higher than this. These very high cooling rates could not be attained in all specimens because the composition of some were such that slag formed on the surface and coated the quench tube, greatly increasing the interface resistance. However, measured rates of  $6^{\circ}\text{C}/\text{sec.}$  were still obtained  $3/8$ " from the tube in these alloys. By keeping the induction power on during solidification and using a specimen 5 inches long cooling rates from  $0.5^{\circ}\text{C}/\text{sec.}$  to  $100^{\circ}\text{C}/\text{sec.}$  were obtainable in a single ingot. Quantitative relationships between cooling rates and inclusion size or morphology were not sought. Qualitative effects of cooling rate were clearly demonstrated, however.

Prevention of undercooling of the iron phase was accomplished in most samples by nucleation with an iron wire. In some cases this proved impossible because of formation of solid slag phase on the surface of the melt which could not be penetrated. In other cases undercooling of the iron phase was intentionally permitted. The effects are discussed below. Nucleation of the slag phase by means of an MnS coated wire was attempted several times. No effect was observed. This is attributed to the fact that the slag particles are so dispersed that only a few are nucleated. In almost all specimens, therefore, the MnS phase was allowed to freeze or undercool according to its own predisposition.

## 2. Effect of Cooling Rate on Sulfide Morphology.

a) Type I: The effect of increasing cooling rate is to

decrease the size of Type I duplex inclusions in the Fe-Mn-O-S system. Figures 21b and 21c show this effect. Alloy 5-5 was cooled at  $1^{\circ}\text{C}/\text{sec.}$  compared with a rate of  $8^{\circ}\text{C}/\text{sec.}$  for Alloy 5-7.

The Type I inclusions, often containing included iron, which were observed in the systems other than Fe-Mn-S-O exhibited no demonstrable relation of size to cooling rate. They varied considerably in size and in distribution in the melt. When cooling proceeded with the induction power off there was a greater tendency to find them near the top of the ingot but some could generally be found near the sides or bottom also. The volume fraction and average size of these Type I inclusions seemed to depend most clearly on how far into the miscibility gap the initial additions to the crucible placed the overall composition. Figures 28a and 28b show that Type I inclusions in Alloy 25-1 do not change noticeably in size with distance from the quench tube, although the D inclusions become significantly coarser at greater distances and lower cooling rates. A similar independence of size of large Type I inclusions to cooling rate was observed in 8-23.

b) Type D Inclusions: Figures 29a and 29b show that the MnS dendrites become larger at lower cooling rates in Alloy 25-1. Figures 25b and 25d compare the morphology of dendrites in 8-14 and 8-15, cooled at  $1.3^{\circ}\text{C}/\text{sec.}$  and  $8^{\circ}\text{C}/\text{sec.}$ , respectively. The effect is also observed in Alloy 21-1. Curvature of some of the MnS dendrites near the quench tube is shown



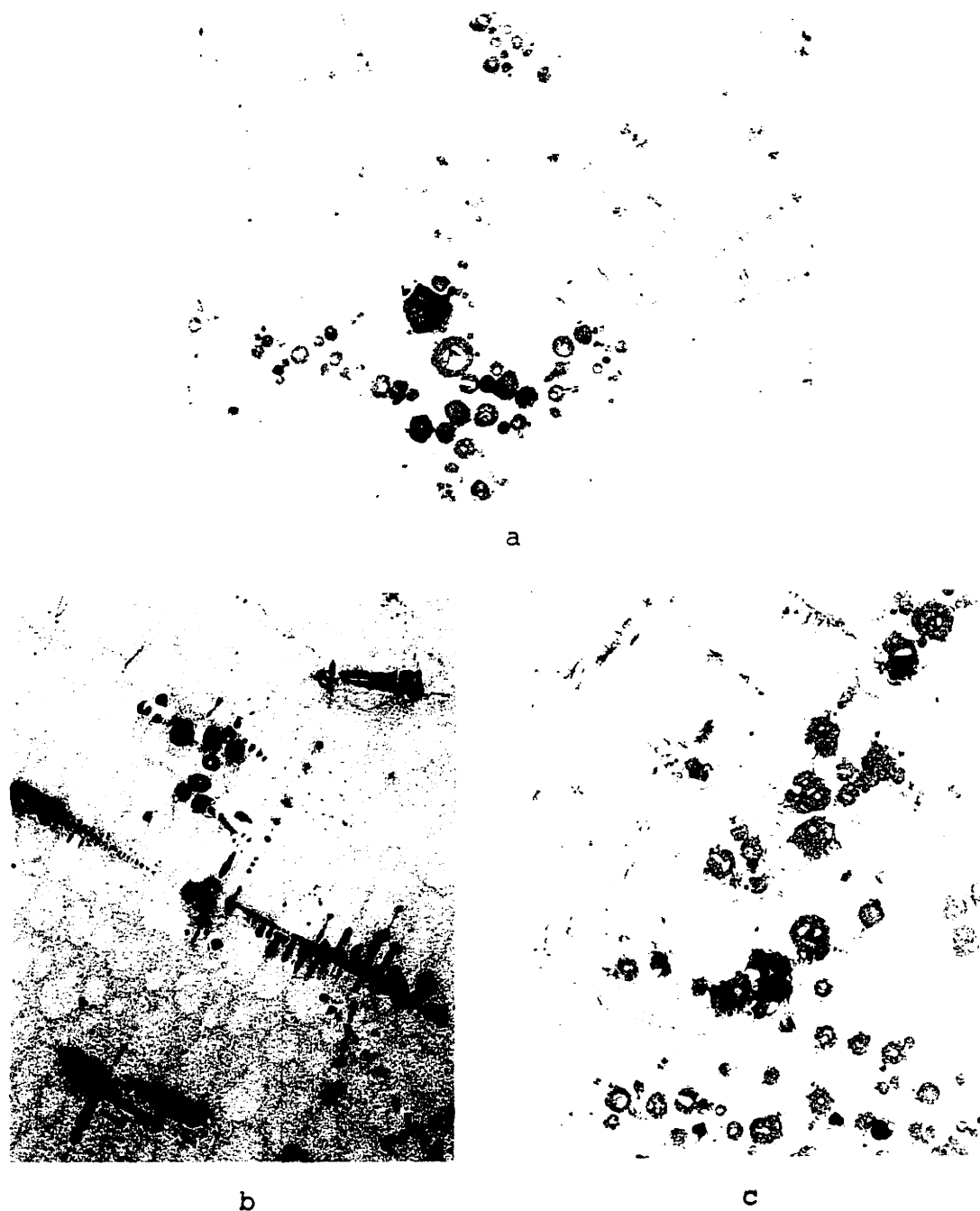


Figure 28: Photomicrographs of Type I inclusions showing effect of cooling rate.

- a) Alloy 25-1: Typical Type I inclusions found 3 millimeters from the quench tube, 100X. 2.64% Mn, 0.66% S, 3.01% C.
- b) Alloy 25-1: Typical Type I inclusions found 1.5 centimeters from the quench tube, 100X.
- c) Alloy 25-1: Nital etch reveals size and position of Type I inclusions versus iron dendrites, 100X.

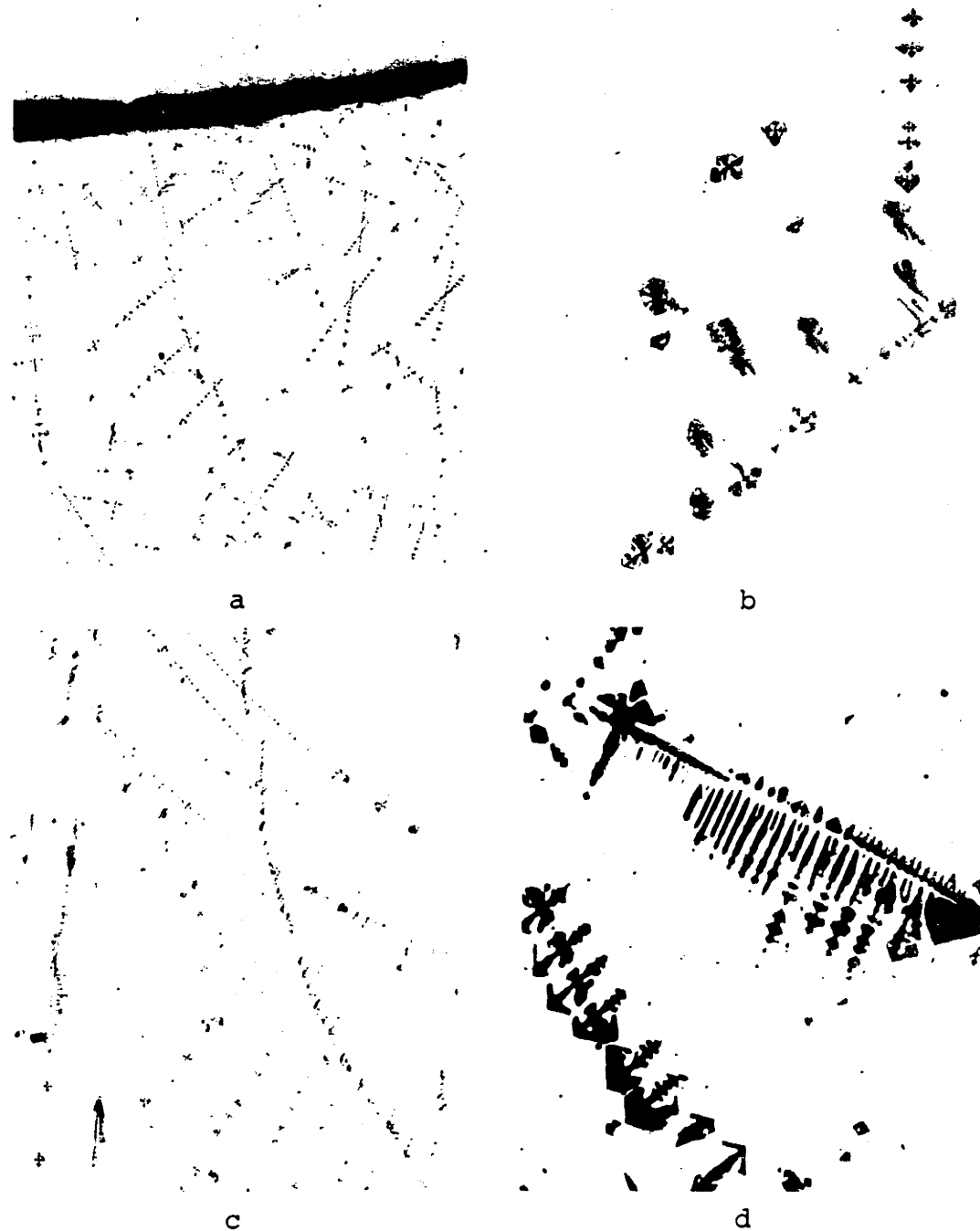


Figure 29: Photomicrographs of Type D inclusions showing effect of cooling rate.

- a) Alloy 25-1: Dendrite structure next to quench tube, shown on top side of picture, 100X. 2.64% Mn, 0.66% S, 3.01% C.
- b) Alloy 25-1: Dendrite structure 1.5 centimeters from tube, 100X.
- c) Alloy 25-1: Shows typical example of curved dendrite near (3 mm.) quench tube, 100X.
- d) Alloy 25-2: Coarse dendrite near top of ingot cooled at 0.8°C/sec., 100X. 2.6% Mn, 0.65% S, 3.66% C.

in Figure 29c. Figure 29d shows the coarse dendrites found near the top of 25-2. Alloy 25-2 was given the same initial addition of manganese and sulfur as 25-1, but was allowed to cool at  $0.8^{\circ}\text{C}/\text{sec}$ . with a small amount of induction power on, instead of being quenched with the water-cooled tube.

c) Type II R Inclusions: Direct comparison of the effect of cooling rate on Type II R inclusions in a single specimen was not made. However, a comparison of the structure of 8-8 which is close to 8-11 in composition will show that increasing the cooling rate from  $1^{\circ}\text{C}/\text{sec}$ . to  $10^{\circ}\text{C}/\text{sec}$ . decreases the size of the rods (Figures 30a and 30b).

d) Type II S Inclusions: Comparison of the photo-micrographs in Figures 30c and 30d will show that the Type II S inclusions in Alloy 8-23 decrease in size as the chill is approached.

e) Type III Inclusions: The angular Type III inclusions are also affected by cooling rate. They are larger when the cooling rate is lower, as shown in Figures 31a and 31b.

### 3. Effect of Undercooling of Metal Phase on Sulfide Morphology

A limited number of specimens were made which demonstrate some of the effects of undercooling. They are discussed below.

a) Type I Inclusions: Alloy 8-5 was cooled from  $1635^{\circ}\text{C}$  at a rate of  $1^{\circ}\text{C}/\text{sec}$ . It did not freeze until  $1440^{\circ}\text{C}$  was reached, and recalesced to  $1490^{\circ}\text{C}$ . Undercooling was therefore at least

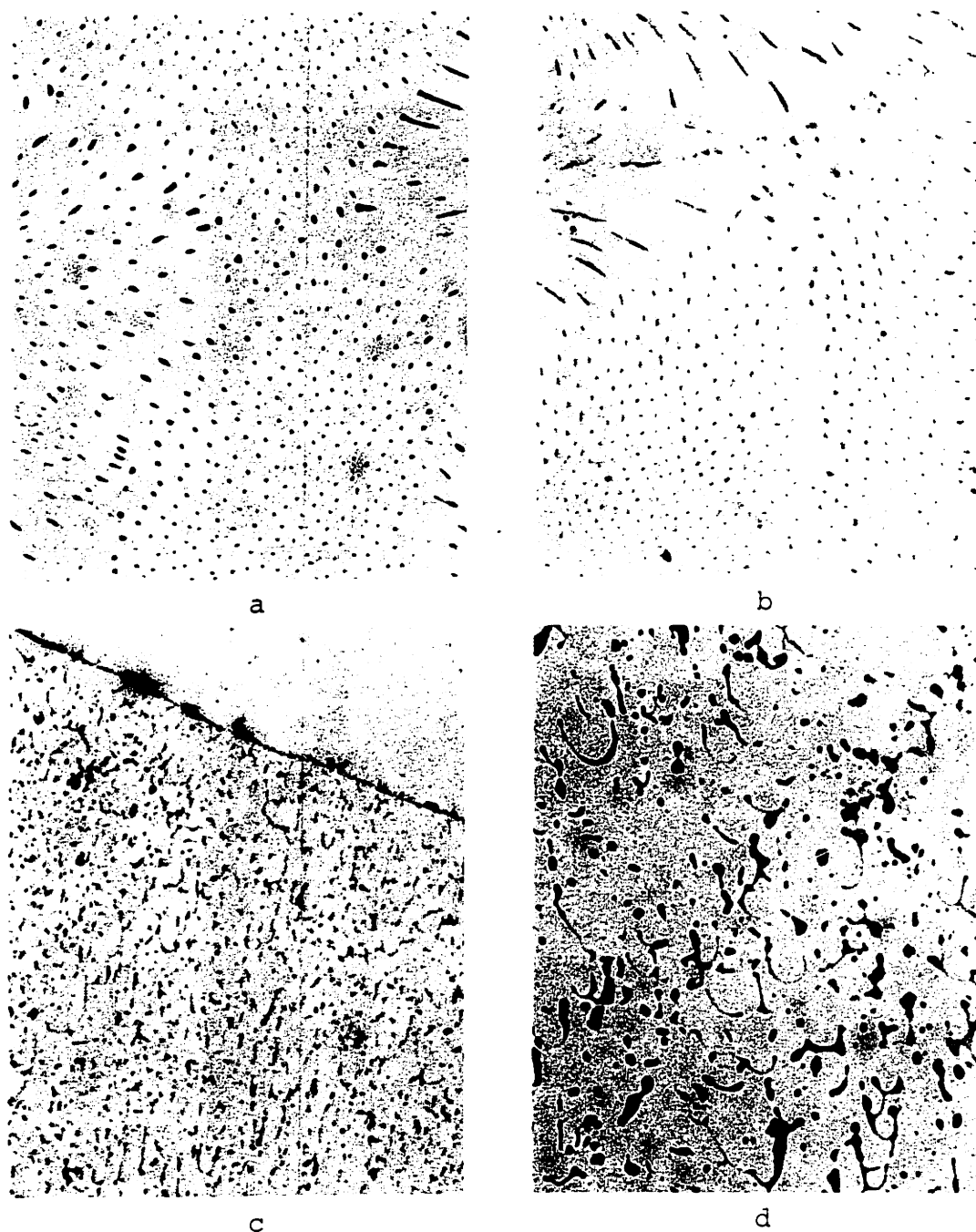


Figure 30: Photomicrographs showing the effect of cooling rate on Type II R and II S inclusions. Table 3.

- a) Alloy 8-8: MnS rod-like inclusions resulting from a cooling rate of  $10^{\circ}\text{C}/\text{sec.}$ , 200X. 2.76% Mn, 1.18% S.
- b) Alloy 8-11: MnS rod-like inclusions resulting from a cooling rate of  $10^{\circ}\text{C}/\text{sec.}$ , 500X. Note that magnification is 2.5 times as great as in Figure 16a.
- c) Alloy 8-23: Type II S inclusions next to chill, 200X.
- d) Alloy 8-23: Type II S inclusions 1.5 centimeters from the chill, 200X. 0.63% Mn, 2.62% S.



Figure 31: Photomicrographs showing effect of cooling rate on Type III inclusions.

- a) Alloy 21-3: Small Type III inclusions. Quench tube was in black area on upper left, 200X.
- b) Alloy 21-3: Type III inclusions located 1.2 centimeters from quench tube, 200X. 2.5% Mn, 0.24% S, 4.43% C.

50°C. However, the size and morphology of the large MnS inclusions is the same as that of Alloy 8-2 which is in the same composition range on the Fe-Mn border of the miscibility gap, but which recalesced only 20°C. No other evidence was found to cast doubt on the independence of the morphology of the large Type I inclusions with included iron from undercooling of the iron.

No study was made of the effect of undercooling on the morphology of the duplex Type I inclusions of the Fe-Mn-S-O system.

b) Type D Inclusions: No systematic study of the effect of iron-phase undercooling on MnS dendrite morphology was made.

c) Type II R Inclusions: The effect of undercooling on the II R inclusions is to decrease their size, as comparison of the fine rods in Figure 19d with those in Figure 45a will show. Both specimens were cooled at approximately 1°C/sec. Alloy 5-25 was prevented from undercooling, while 8-4 was allowed to undercool 100°C.

d) Type II S Inclusions: No experiments were made which enable any statement to be made on the effect of undercooling on Type II S inclusions.

e) Type III Inclusions: No experiments were made which enable any statement to be made on the effect of undercooling on Type III inclusions.

#### 4. Effect of Temperature of Addition of Manganese to the Melt

In order to study the effect of large deviations from equilibrium on sulfide morphology, four specimens were made by adding the manganese to the melt at temperatures below the melting temperature of MnS, instead of adding it at the usual temperature of 1650°C where all phases are liquid.

Alloy 29-1 was made by melting Ferrovac-E and Fe-FeS master alloy together in the crucible under 1/2 an atmosphere of helium. At 1650°C, 0.1% Al was added. The melt was then allowed to cool to 1545°C, at which time the Fe-Mn master alloy was added and the induction power turned off. One minute later the melt was nucleated at 1504°C, and recalesced to 1511°C. A similar procedure was followed with Alloy 29-3. In this case, however, carbon was added to the melt and the vacuum pump was used to lower the pressure to 1000 microns to obtain a carbon boil. The chamber was again back-filled with helium to 1/2 an atmosphere, and the specimen was allowed to cool to 1545°C, when the Fe-Mn master alloy was added. Induction power was shut off, and one minute later the melt was nucleated with a Ferrovac wire. Recalescence again increased the temperature about 6°C, to a maximum of 1496°C. The structure of the resulting sulfides are similar, as is shown by comparing Figure 16b with Figure 19a. The method of deoxidization has apparently had no important affect on inclusion formation in this system, except that the small amount of carbon present in

29-3 may have lowered the freezing temperature of the iron phase.

When more sulfur is present in the melt when the manganese is added, large MnS dendrites form, as in Alloys 8-1 and 32-1. Manganese was added to 32-1 at 1547°C, and to 8-1 at 1590°C. Large Type I inclusions with included iron formed in the latter, but none were found in 32-1. The morphology of the D inclusions, however, was very similar (Figures 18c and 20c).

For a third approach to the problem of Type D and Type I morphology as a function of thermal history, the following procedure was followed: manganese and aluminum were added to the melt at 1630°C, which was then allowed to cool down to the freezing point at 1508°C with moderate induction power on. This required approximately 6 minutes. The Type II R inclusions were present as usual, but the D and I inclusions were mostly concentrated near the top and sides of the ingot. The D inclusions are coarser than in 8-1 and 32-1, and are much less extensive (Figure 16c versus 20c).

##### 5. The Effect of Solid-State Transformations.

The object of the present research was to study the morphology of as-cast structures and not to consider the effect of thermal or thermo-mechanical processing after the initial solidification. However, a few experiments were carried out to determine whether relatively small differences in the time spent in various phase fields during the initial solidifica-



tion would have an effect on the structure observed at room temperature. This was really an attempt to determine the relative importance of phase transformation events which occur after solidification and those which occur prior to and during solidification.

Alloy 5-26 was cooled at  $1^{\circ}\text{C}/\text{sec}$ . from the completely liquid state. According to the phase diagram, it spent approximately 1 minute in the  $\delta$ -Fe region. Alloy 5-30, however, was held for 10 minutes at  $1450^{\circ}\text{C}$  in the  $\delta$ -Fe region and then rapidly quenched. Examination of Figures 17a and 18b will show that there is no apparent difference between the two structures which can be attributed to the holding time or cooling rate after solidification. Slightly more II R inclusions are present in 5-30, as would be expected from its slightly higher MnS content. Several other specimens were made to investigate this problem, and visible differences did not occur. It is concluded that cooling rates in the solid state of the order of those used in this study have little or no effect on the observed structure. This does not preclude the possibility that changes could occur over longer treatment times, at different compositions, or on a sub-microscopic scale.

## VII. INTERPRETATION OF EXPERIMENTAL RESULTS.

### EVALUATION OF SOLIDIFICATION MODELS. FRACTURE.

#### A. Introduction

Proposed models for solidification were developed in Chapter IV, and the results of experiments designed to test these models were reported in Chapter VI. The present chapter is a discussion of the experimental results and the conclusions which may be drawn from them.

#### B. The Systems Fe-Mn-S, Fe-Mn-S-O, and Fe-Mn-S-Al.

##### 1. The Fe-Mn-S System

No difference was observed between sulfide forms resulting from deoxidation by means of a carbon-boil rather than addition of aluminum. Comparison of Table 2 with Table 3 will show that the same compositions in the two systems result in identical morphologies. This may be confirmed by examination of Figures 16-20. Dahl<sup>17</sup> and Salter and Pickering<sup>73</sup> found evidence that alumina particles may act as heterogeneous nuclei for Type III inclusions. This leads one to expect easier nucleation of sulfide in aluminum deoxidized systems than in carbon-boil ones. What likely occurs, however, is that decomposition of the crucible walls during the carbon boil raises the level of alumina or aluminum in the melt to such a level that there are always sufficient numbers of nuclei present even in the carbon-boil melts for easy

heterogeneous nucleation. Repetylo, Olette, and Kosakevitch<sup>74</sup> found, for example, that suspensions of alumina particles smaller than 20 microns could remain in a stirred metal bath for more than 20 minutes after the addition of aluminum. Further, Alloy 8-9, which was deoxidized by means of a carbon-boil at 1650°C contained 0.006% soluble aluminum, even though no aluminum had been added. Such amounts of aluminum could easily combine after the boil but prior to solidification with trace amounts of oxygen present in the furnace atmosphere or in alloying additions. Whatever the explanation, the experimental observation is important for the present research: the method of deoxidation (aluminum or carbon-boil) had no detectable effect on inclusion morphology. Results obtained by one deoxidation method are therefore taken as being interchangeable with those obtained by the other method.

#### Solidification on the Fe-Mn Side of the Fe-MnS Line

An expected path of solidification in this region of the Fe-Mn-S system was developed in Chapter IV and was schematically diagrammed in Figures 8, 9 and 10. The validity of this model will now be established by comparing it with the experimental alloys, starting with a simple example of eutectic solidification such as Alloy 5-25.

The initial composition of Alloy 5-25 places it in the Fe + L field at a position near that of Figure 8a. Manganese sulfide is expected to form a eutectic with the iron phase after initial solidification has enriched the remaining liquid

sufficiently. Type II R inclusions surrounding the primary iron dendrite arms are the resultant eutectic morphology (Figure 45a). Figure 32 is a sketch showing how they form. Confirmation of the curved solidification path in Figure 8a would require electron microprobe analysis of the dendrite arms plus quantitative analysis of the amount of eutectic which formed. However, the validity of the assumption of differential segregation of manganese and other elements during solidification is so well documented in the literature<sup>75,76</sup> that such analysis was not deemed necessary. Undercooling of the iron phase may easily occur but was generally prevented in the present research by nucleation with an iron wire. The extent of undercooling or nucleation barriers for the sulfide phase cannot be determined from specimens 8-4 or 5-25.

Because of the narrowness of the  $L_m + MnS$  region it is not known whether the composition of any of the experimental alloys fell in this region. However, many of them were just inside the miscibility gap and should follow the path of Figure 10 if the assumptions of the solidification model are correct. Among the experimental alloys in this region are 8-7, 8-8, 8-9, 8-11, 8-13, 8-2, and 8-5. Type II R inclusions are present in all of these specimens. The new phases which are present are Type D and the Type I with included iron, which evidently form prior to reaching the eutectic.

In Chapter VI the size of Type I inclusions formed at high Mn + S levels was shown to be independent of the rate of

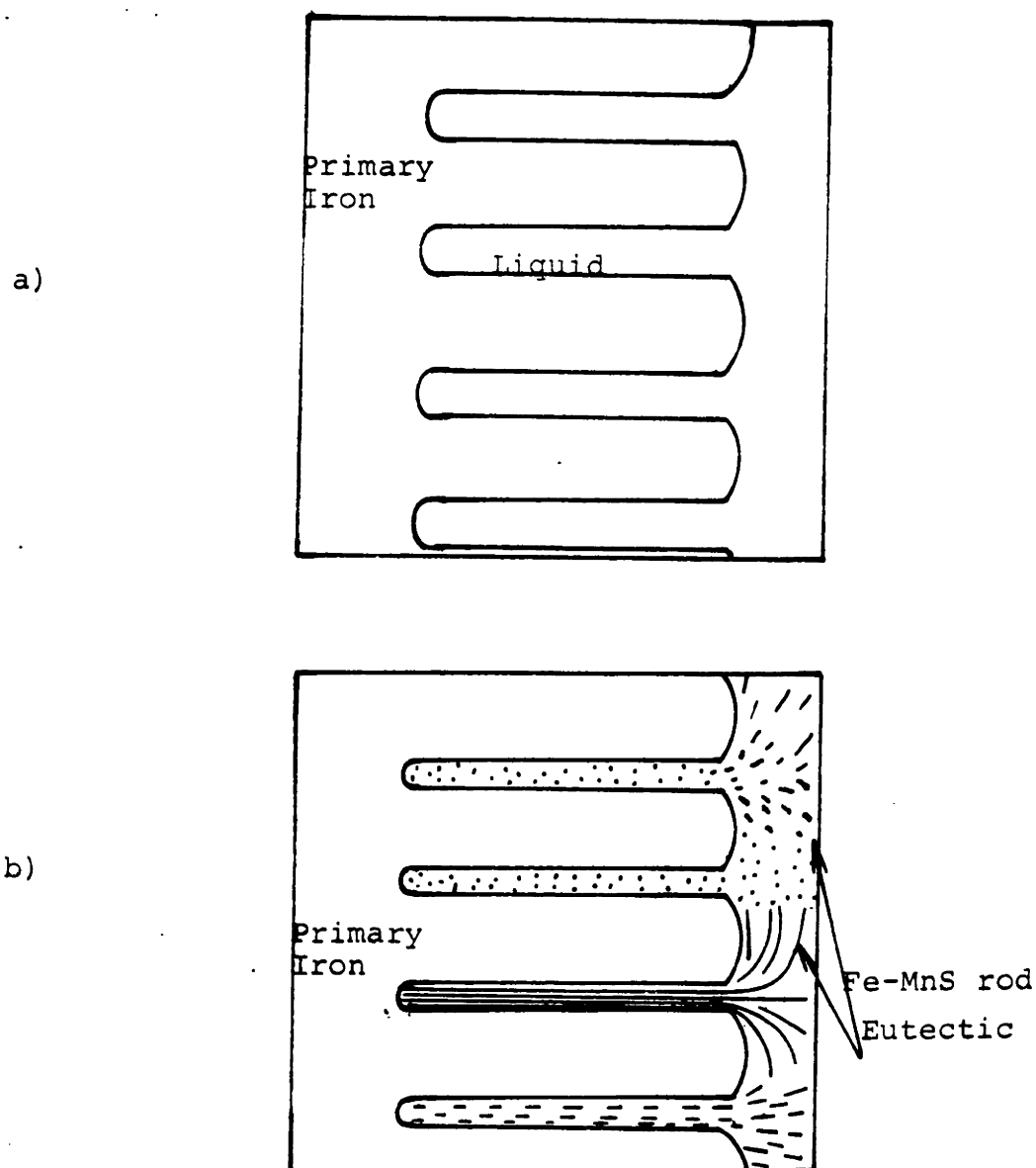


Figure 32: Schematic illustration of the formation of Type II R rod eutectic.

- a) Primary iron dendrite arms surrounded by liquid enriched in manganese and sulfur.
- b) Eutectic nucleates and grows to fill up dendrite interstices and interdendritic liquid. Note that eutectic rods do not generally grow across from one thickening dendrite arm "platelet" to the next one, but instead grow parallel to the platelets. They may branch out and change orientation as they grow.

cooling below the miscibility gap and of undercooling of the iron phase. This is reconfirmed by examination of Figure 28 which shows that the size of the iron and MnS dendrites bear no relationship to the size of the round inclusions. In this particular specimen, Alloy 25-1, the Type I inclusions showed a fairly random distribution throughout the melt because strong stirring was caused by applying induction power of about 12 k.w. until the water-cooled tube was introduced into the melt. In heats cooled with the power off, these Type I inclusions are preferentially distributed near the top of the melt, although some may also be found near where sulfide has formed a thick layer on the crucible walls or thermocouple protection tube. Many of the Type I inclusions are much larger than the distance between dendrite centers at the cooling rates used in these experiments. This is demonstrated in Figure 28c, where the round inclusions are seen to be independent of the iron dendrites. Although Alloy 25-1 is a high-carbon melt it must serve to give some idea of the dimensions under discussion, since the outlines of the original dendrites in the pure Fe-Mn-S system are not revealed by etching. The very large size of the present Type I inclusions, plus their independence of the dendritic structure rules out the possibility that they formed as solid state precipitates, as a result of segregation between dendrite arms, or as solids after solidification of iron starts. They are slag droplets which form in the  $L_s + L_m$  region above

1610°C. When the  $L_s + L_m + MnS$  tie-triangle forms at  $T_1$  (Figure 10), they can begin to solidify, rejecting iron and manganese into the remaining liquid phases. If the barrier for nucleation of solid sulfide from liquid slag is low there will be no undercooling of the slag droplets. Vogel<sup>26</sup>, however, has proposed that the included iron in the slag droplets is an indication that they have been undercooled, and may even have formed after solidification of iron has begun. Conceivably, this may be true in some instances, despite the fact that slag undercoolings of over 100°C are implied. However, Vogel's model implies that nucleation of undercooled liquid sulfide in liquid iron is easier than nucleation of equilibrium solid sulfide. The existence of such large undercooling is contradicted by the following experimental facts: When manganese is added to a melt containing sulfur at a composition on the borders of the miscibility gap and at a temperature below the freezing point of manganese sulfide, many transition Type I/III inclusions form. None of these contain included iron. When manganese is added to a melt containing enough sulfur to place it well within the miscibility gap at the same temperature large dendrites form (Alloy 32-1). Type I inclusions, with or without included iron are completely absent. This implies that solid sulfide can easily form in the melt at far less than 100°C undercooling. Their morphology depends upon the degree of supersaturation of the melt. Solid Type I and Type I/III morphologies occur when

the solubility limit in liquid iron on the  $L_m + \text{MnS}$  surface at the particular temperature is only slightly exceeded (Alloys 29-1, 29-3). Larger excesses are relieved by dendritic growth into the melt (Alloy 32-1). Liquid slag particles do not form when manganese is added at these temperatures. However, at temperatures just above the monotectic ( $1580^\circ\text{C}$ ) liquid slag can form, as in 8-1. When the temperature then falls below the monotectic the slag droplets freeze, along with slag on the surface and crucible walls. Dendrites grow into the melt from these sites to accommodate the decreasing solubility of the melt for MnS. Such manganese sulfide dendrites were observed in all melts which intersected the miscibility gap on this side of the phase diagram. Type I inclusions with included iron were observed in all of those ingots which were heated into the all-liquid  $L_s + L_m$  region. They were not observed in those ingots (29-1, 29-3, 32-1) which did not exceed the  $L_m + \text{MnS}$  temperature range after manganese was added. According to Vogel's model, liquid Type I inclusions which solidify with occluded iron should form in these alloys as well since he believed they could even be supercooled to below the melting point of the iron phase. According to the present research, this seems very unlikely.

Further experimental evidence that undercooling of the manganese sulfide droplets is small is shown in Figure 18a. The photomicrograph shows the growth of several stubby dendritic extensions from an inclusion. This can only occur



after the droplet has solidified, while the temperature is still in the  $L_m + MnS$  region, and while rejection of solute from the melt is occurring. The iron phase in this specimen undercooled only a few degrees. Such structures were fairly common in the other specimens of this series as well.

The appearance of the droplets implies that when they freeze liquid iron intrusions are formed. The following mechanism is proposed for the formation of such structures: Nucleation of the solid sulfide occurs at the iron-slag interface. Heat rejection and solute redistribution considerations cause solidification to proceed along the inside surface of the droplet, forming a crust of solid sulfide. Before the crust is completely formed, or shortly afterwards, solidification shrinkage causes the metal to surge through a hole formed in the surface. Intrusions of iron in the shape shown in Figures 17c and 19c which look like the pestle from a mortar-and-pestle set, and which are associated with smaller particles of iron on each side are frequently observed. These latter may be caused by turbulence or eddy effects which occur when the liquid iron flows through the crust to fill the interior shrinkage. The smaller droplets of iron observed away from the major intrusion may have nucleated to accept excess iron and manganese in regions too far from the surface or intrusion for rapid diffusion. A further indication which supports the possibility of such a model of slag droplet solidification is the fact that the head or "grinding surface"

of the "pestle" often forms a concentric circle with the outside surface, indicating that this is how far the crust grew before intrusion occurred. Finally, the fact that such intrusions actually are connected with the liquid outside is shown in Figure 16d.

In summary, the conclusions which may be drawn about solidification on the manganese-rich side of the phase diagram are as follows: The Type I inclusions with included iron are slag droplets which freeze with little undercooling when the temperature falls below the monotectic. In the  $L_m + \text{MnS}$  region precipitation of MnS occurs by addition onto existing solid slag particles or by growth of MnS dendrites. Type II R inclusions are part of a eutectic which forms when the eutectic valley is reached. When MnS dendrites or Type I slag inclusions are present, nearby iron dendrites can nucleate and then grow by depositing sulfide on these pre-existing sites rather than by organizing into rod eutectic colonies. The result is that near such MnS sinks, the surrounding phase is not 100% eutectic, but shows iron dendrite arms surrounded by small amounts of the rod eutectic (see Figure 20c, for example). The course of solidification drawn in Figure 10 is evidently essentially correct.

#### Solidification on the Fe-FeS Side of the Fe-MnS Line

Because of the uncertainty about the true form of the equilibrium phase diagram on the Fe-FeS side of the Fe-Mn-S system an accurate description of the course of solidification

in this region is much more difficult. A few simple cases will be discussed first.

Alloys 5-21, 5-27, and 8-6 all lie very close to or on the Fe-FeS binary. According to the models developed for either Wentrup's or Vogel's phase diagram these specimens should contain the Fe-FeS eutectic in the interdendritic spaces (Type II S inclusions). The structure of the iron dendrites is very clearly outlined by sulfide in the low-oxygen alloy 8-6 (Figure 20a). The sulfide liquid has spread over the iron phase so that it completely surrounds the dendrite arms. Van Vlack<sup>60</sup> found that manganese and oxygen both have the effect of increasing the interfacial energy between a sulfur-rich melt and solid iron, thereby reducing the spreading tendency and causing the sulfide to become less sheet-like and more spherical. This effect is observed in the case of Alloy 5-21 (Figure 16a) which possesses a much higher O/S ratio than 8-6, although oxide phase is not visible so that it fulfills the definition of "deoxidized" used here. Alloy 5-27 possesses a lower O/S ratio than 5-21 (0.03 vs. 0.09), but the expected tendency to revert to the completely sheet-like morphology of 8-6 is apparently negated by 0.02% Mn content. The result is that a few round inclusions form in addition to the sheet-like ones.

Alloys 5-26 and 5-30 both lie near the known boundaries of the miscibility gap and along the stoichiometric Fe-MnS line. Since the maxima of the miscibility gap and the eutectic

lie to the right of this line the phase diagram surfaces slope toward the Fe-FeS side of the diagram and the models developed for solidification in this region should be applicable. Alloy 5-26 is in the region of initial composition "1" in Figure 11, but closer to the eutectic than shown. The structure is expected to contain primary iron dendrites plus large amounts of eutectic. According to Vogel's phase diagram and the solidification path shown in Figure 11, the structure should contain a large volume fraction of rod eutectic formed at relatively high temperatures plus small fractions of sulfide formed as the ternary eutectic is approached. It may be expected at some level of substituted iron in the Q sulfide that the rod eutectic structure may break down, possibly because of a lowering of the interfacial energy caused by the dissolved FeS. The structures of Alloys 5-26 and 5-30 conform to such expectations (Figures 17a and 18b). Sheet-like FeS sulfides and serrated sheets consisting of a mixture of FeS and Q sulfide are found in the boundaries between eutectic colonies. The morphologies present in specimens 5-26 and 5-30 are consistent with Vogel's phase diagram and the assumptions made in drawing Figure 11.

Wentrup's phase diagram and the solidification model under consideration also predict structures for alloys in the composition range of 5-28 and 5-30 which are consistent with the experimental results. The high manganese contents of 5-26 and 5-30 probably place them in the region of the

four-phase plane designated by the open circle in Figure 12. Large volume fractions of rod eutectic are expected to form, followed late in solidification by partial dissolution of Q sulfide and formation of FeS-rich slag between the eutectic colonies. Some structures which might be considered evidence of partial dissolution of the rod eutectic are the thickened ends of some eutectic rods (Figure 18b). However, this structure could also be the result of breakdown of the rod eutectic caused by increasing sulfur content in the melt under Vogel's model. Furthermore, it is also seen in alloys on the Fe-Mn side of the diagram where such sulfide remelting is not expected (Figures 19b and 30a).

Alloy 8-23 lies very near in composition to initial composition "2" in Figure 11. Very small amounts of slag phase were present on parts of the top surface of the ingot, but not enough to coat the quench tube (Figure 30c). The miscibility gap and eutectic lie very close together here, but do not touch, according to Vogel's investigation. Melts solidified from this composition should contain sulfide solidified along the eutectic valley. A coarse degenerate channel structure rather than the classic rod colonies is one conceivable morphology. The melt consists of 100% eutectic. It must reject solid sulfide and iron as the temperature falls and the remaining liquid becomes enriched in sulfur. The expected structure is present near the quench tube in Alloy 8-23 (Figure 30c). Even under the high thermal

gradients existent there it is quite irregular. Degeneracy increases at the lesser gradients one-half inch from the tube (Figure 30d). Hook-like morphologies which are probably cup-shaped in three dimensions result where liquid sulfide near the ternary eutectic evidently cuts off further growth of the iron phase. Vogel's interpretation of the phase diagram is supported by the structure observed in Alloy 8-23.

The composition of Alloy 8-23 should place it on the edge of the miscibility gap of Wentrup's phase diagram. The initial phases which should form are solid iron and liquid slag. A clear cut dendritic structure should result with fairly large spherical inclusions either pushed into the interdendritic fillings, or entrapped at various stages of solidification per Yarwood. This is not observed and indicates that the model of Wentrup is incorrect.

Alloy 8-10 also lies on the border of the miscibility gap, but is intermediate in manganese content between 8-23 and 5-30. Areas of rod eutectic are surrounded by elongated Q sulfides and Type II S FeS inclusions. Evidently the rod eutectic breaks down into a degenerate structure as the manganese content of the liquid decreases. Such a breakdown is shown in Figures 33a and b. The serrated Type II S inclusions observed in Alloy 5-26 and 5-30 (Figure 17a) form between colonies of rods. In these regions the iron and sulfur content of the remaining liquid has been increased so rapidly by segregation in the final stages of solidification that

the degenerate Q-sulfide rods do not have room to develop. These structures are consistent with the degenerate eutectic model discussed above for Vogel's version of the phase diagram. The dendritic iron structure and spherical slag particles which would be expected to form on a four-phase plane are not observed.

In summary, the above discussion indicates that the model of the Fe-MnS phase diagram in which the eutectic passes close to the miscibility gap but does not intersect it (Vogel's model) is the correct one. It is further concluded that the solidification diagram of Figure 11 and the assumptions on which it is based are essentially correct. A sulfide morphology which occurs on this side of the phase diagram but not on the Fe-Mn side is Type II S. These inclusions are the result of precipitation in the interdendritic spaces along the eutectic late in solidification. They form as sheet-like duplex (Fe, Mn)S-FeS sulfides when small concentrations of manganese are present. At larger manganese levels, Type II R inclusions form instead.

## 2. The Fe-Mn-S-O System

The transition from Type II R to Type I morphology is a function of several variables, the most important of which is the oxygen level. It may be noted, however, that Alloys 5-26 and 5-30 which have relatively high O/S ratios of 0.08 and 0.03 showed no metallographic evidence of oxide formation

(Figure 17d). On the other hand, Alloys 5-28 and 5-29 with O/S ratios of 0.02 and 0.04 formed large slag particles consisting primarily of manganese sulfide with included eutectic manganese oxide structures (Figures 22a and c). The difference between these pairs of specimens is their Mn/S ratios, with the former pair containing near the stoichiometric ratio and the others less than this. Manganese would be expected to decrease the tendency to form the Type I duplex slag inclusions during solidification, at least at high sulfur levels where segregation is not extensive, because of its effect on the phase diagram. That expectation is confirmed by the behavior of Alloys 5-29, 5-28, 5-26, and 5-30. Manganese increases the melting temperature of the Q sulfide which forms at a given O/S ratio. This moves the  $L_m + Q + Fe + L_s$  and  $Fe + L_s + L_m$  regions shown in Figure 7 to higher O/S ratios making their intersection less likely. A borderline case is Alloy 5-31 (Figures 33c and d), which contains the duplex  $L_s$  phase as do 5-28 and 5-29. The composition of this alloy would place it in the miscibility gap of the pure Fe-Mn-S system. Visible oxide is found only in large spherical, primarily MnS inclusions in 5-31, because the oxygen and sulfur are more strongly bonded to the manganese than to iron. Dendritic sulfides do not form, evidently because oxygen has lowered the sulfide melting temperature to near the iron liquidus. Large amounts of Type II R inclusions do form, however, as well as some of the degenerate rod and II S types.



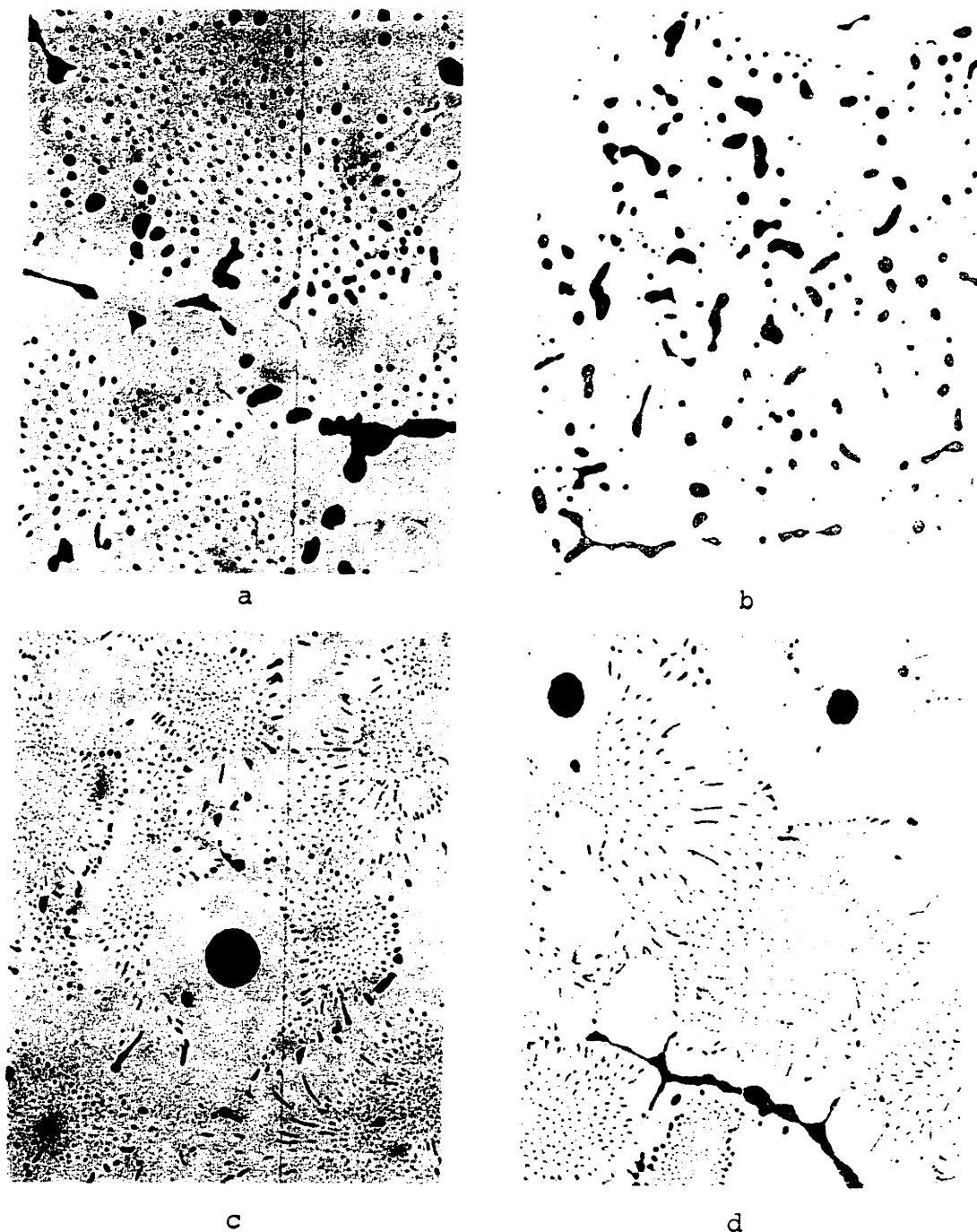


Figure 33: Structures observed on the Fe-FeS side of the Fe-Mn-S diagram.

- a) Alloy 8-10: Transition between regular and degenerate rod morphology, 500X. 0.93% Mn, 1.3% S.
- b) Alloy 8-10: Degenerate rod morphology, 500X.
- c) Alloy 5-31: Oxide-bearing slag inclusion, surrounded by Type II R inclusions, 200X.
- d) Alloy 5-31: Rod eutectic and duplex serrated Type II S inclusions, 200X. 1.89% Mn, 1.1% S, 0.10% O.

The melt composition intersects the  $L_s + L_m$  region in Figure 5 with most of the oxygen taken up by the initial slag droplets. The  $L_m + L_s + Q$  region is entered just above the iron liquidus and then the  $Fe + L_m + Q + L_s$  region is entered, resulting in precipitation of Type II R inclusions. At the end of solidification some of the serrated Type II S inclusions form since the Mn/S ratio is on the Fe-FeS side of the Fe-Mn-S ternary. Except for a few of the Type I inclusions, the structure is very similar to that of Alloy 8-10. These observations show that modification of the various morphologies with changing oxygen content is gradual on the Fe-FeS side of the eutectic maximum.

When the sulfur content is low and the Mn/S ratio is close to or exceeds the stoichiometric value, the  $Fe + L_s + L_m$  region is intersected (Figure 5) after some segregation has taken place. Slag droplets form in the interdendritic spaces and are subsequently entrapped by growing iron dendrites. These are Type I inclusions.

At the high O/S values such as those found in Alloy 5-5 the oxide phase becomes visible (Figure 21b). Note that separate oxide phase is not visible in Alloy 5-6 (Figure 21d), although the O/S ratio is equal to that of 5-5. This is believed to result from the difference in partition ratios for oxygen and sulfur. Because of the lower initial sulfur concentration of Alloy 5-5 the slag phase does not form in that specimen until later in solidification when the O/S ratio

has been increased by differential segregation of oxygen and sulfur. The solubility limit of MnS for MnO is then exceeded.

These observations indicate that the phase diagram sections presented in Figures 5, 6, and 7 are useful for understanding precipitation of Type I inclusions in iron and for rationalizing the oxygen dependency of the Type I to Type II transition. The transition is not a highly sensitive function of oxygen content at high sulfur levels. At low sulfur levels small changes in the oxygen content will have a more noticeable effect because of its larger effect on the O/S ratio.

### 3. The Fe-Mn-S-Al System

A brief investigation was made to confirm the conclusions of Dahl, Hengstenberg, and Düren<sup>17</sup> that excess aluminum alone is insufficient to cause Type III inclusions and to extend their results to different compositions. The results of two melts which were chemically analysed, and several others which were not, indicate that their conclusion is correct. When excess aluminum is added to melts with or without manganese a duplex morphology which turns very dark on exposure to the air is observed. This is evidently some sort of mixed aluminum sulfide with a melting point below that of pure MnS.

Type III inclusions are not expected to form in the Fe-Mn-S-Al system either on the basis of the phase diagram discussed in Chapter III, Section E or as a result of the solid-

ification models discussed earlier in this chapter. They are not observed.

#### 4. Additional Observations on the Fe-Mn-S, Fe-Mn-S-O, and Fe-Mn-S-Al Systems

Type III inclusions, except for the transition Type I/III inclusions formed under highly non-equilibrium conditions, were not found in the Fe-Mn-S, Fe-Mn-S-O, or Fe-Mn-S-Al systems. Additions of excess aluminum did not produce Type III inclusions but formed instead a very dark form of duplex or multiplex aluminum-manganese or aluminum-manganese-iron sulfide of approximately spherical morphology (Figure 26d). Long holding periods such as those employed by Van Vlack<sup>61</sup> to obtain liquid intergranular sulfides were not used. The morphology he obtained does not in any case meet the present definition of Type III inclusions, and does not look like the Type III sulfides presented by Sims<sup>13</sup> or Lichy<sup>15</sup>. The faces of Van Vlack's angular inclusions are concave or convex rather than planar as required by the definition used here. Furthermore, he did not obtain them in the as-cast condition.

It is therefore concluded that Type III inclusions are not formed in the pure Fe-Mn-S system, or by additions of oxygen or aluminum. Elements such as carbon and silicon are responsible for Type III formation.

### C. Type III Inclusions

In Chapter IV, Section D calculations were made of the effect of segregation during solidification on the manganese, sulfur, silicon and carbon content of the remaining liquid. Predictions were made that solid sulfide would begin to precipitate at specific fractions solid, or, in some cases, even before the beginning of iron solidification. The experimental results, reported in Tables 5, 6, and 8, show that the morphologies which can form are the usual spherical slag droplets, rods, and dendrites plus two new morphologies which have been designated Type III and Type II F. A more detailed examination of the formation of these inclusions follows.

The purpose of studying some of the highly alloyed specimens prepared in this research will be made clearer if the problem and necessity of locating the original, as-cast dendrite arms is considered. The positions of these iron dendrite arms are useful for studying the role of microsegregation in causing Type III inclusions to precipitate. The original  $\gamma$ -iron dendrite structure of low-carbon alloys is, however, frequently impossible to delineate by etching, particularly when highly reactive sulfides are embedded in the polished surface. Silicon-bearing alloys are even more difficult to delineate by usual metallographic methods. One solution to the problem is to utilize the Fe-Fe<sub>3</sub>C eutectic as a permanent marker for the original  $\gamma$ -iron interstices and the readily etched pearlite as a marker for the dendrite arms.

This requires an initial melt composition of 2.06% C or greater. The high carbon requirement has several features. One advantage is that at the Fe-Fe<sub>3</sub>C eutectic, graphite saturation of the melt is fairly closely approached so that the solubility values of Figure 14 should be reasonably applicable to this region. Another advantage is that values of 2.06% C, and, for example, 3% Mn and 0.5% S will frequently be approached by commercial alloys towards the end of solidification. Therefore, the inclusions which are found near the center of dendrite arms in the high-carbon experimental alloys would be expected to be forming at the same composition as those precipitating near the end of solidification in segregated regions of commercial alloys. This provides a convenient method of isolating the important later stages of solidification for more detailed study.

In order to understand the full range of morphologies which can result in high carbon and high silicon alloys we will consider first compositions in the range of Examples 1 and 2 in Table 1. Actual experimental alloys which fall in this category are 25-1 and 25-2 (Table 5), 8-19, 8-14, 8-18, 8-15, and 8-20 (Table 6). Alloy 21-1 (Table 8), containing moderate amounts of both carbon and silicon apparently also falls into this category based upon its similar structure. Alloy 25-1 was quenched by means of the water-cooled tube and therefore provides a range of cooling rates in the same specimen. Alloy 25-2 was slowly cooled at 1°C/sec., resulting

in a total solidification time of about 12 minutes. For comparison, the high-silicon alloys 8-14 and 8-15 were cooled at  $1^{\circ}\text{C}/\text{sec.}$  and  $8^{\circ}\text{C}/\text{sec.}$  respectively. These four provide a basis for comparison. The major difference between them is that the silicon alloys were liquid only to a temperature of about  $1380^{\circ}\text{C}$  while the stronger effect of carbon maintained the liquid state at  $1130^{\circ}\text{C}$ . Despite this, the morphologies observed under varied conditions are very similar.

The course of solidification in these alloys will now be considered starting with the all-liquid region and proceeding to lower temperatures. The Type I slag inclusions which formed in the miscibility gap are present in all four ingots. When cooling rates are high (25-1, 8-15), primary dendrites form and grow throughout the melt. These have already been shown in Figures 25d and 29a, b, and c. Intermediate cooling rates away from the chill in 25-1 produce dendrite coarsening. In the slowly cooled alloys, 25-2 and 8-14, considerable coarsening occurs (Figures 25b and 29d) to the extent that the dendrites only appear in a few places in the ingot and are very large. Note that the dendrites in the high-carbon alloys are considerably more faceted than in 8-14 and 8-15. This is attributed primarily to the strong effect of carbon in reducing final solubility of sulfur in the last liquid to solidify. Dendrites in 25-1 and 25-2 are therefore growing in a more dilute solution, which promotes faceting in the last stages of solidification at

dilutions not attained in 8-14 and 8-15. The effect is apparently not dependent upon growth rate in the high carbon alloys, 25-1 and 25-2, which show faceting over the range of cooling rates obtained. However, the high silicon alloys do show a variation in faceting with cooling rate (Figures 25c and d). The reasons for this difference in faceting of the dendrites have not been determined.

Slowly-cooled Alloy 8-15 contained large dendrites and angular Type III inclusions (Figures 25b and c), Type II F inclusions (Figure 26c), and a wide range of smaller Type III inclusions. A model which reconciles and explains these observations is presented in Figure 35. Coarsened dendrites, solidified slag particles, and large angular inclusions float towards the surface, to the extent permitted by electromagnetic stirring and convective turbulence. As the temperature falls, solubility of sulfur in the melt declines and more MnS precipitates on existing inclusions if any are present nearby. By the time the first iron dendrites form the melt is quite dilute with respect to sulfur. The original sulfides are soon isolated from many of the dendrite interstices by growing iron and are unable to take up the excess sulfur rejected into the melt during growth of the iron. Nucleation and growth of more solid MnS must occur in the interstices. The experimental evidence shows that this sulfide can have two basic morphologies. It may form sufficiently far ahead of the thickening iron dendrite "platelets" to grow as a



"divorced" eutectic which acts as a sink for rejected sulfur. This mode produces an angular morphology characteristic of dilute solution growth, Type III. With the saturation sulfur levels under consideration the inclusions should nucleate soon after iron precipitation starts, if not prior to it, and therefore be distributed fairly evenly across the dendrite arms and between them. Their expected locations are shown in Figure 35. Another possible mode is cooperative growth\* of the iron and sulfide phases to produce Type II F inclusions. Primary sulfide dendrites can nucleate this morphology (Figure 23d) in carbon-rich alloys, and probably also in silicon-rich alloys (Figure 26c). Such nucleation of Type II F does not appear necessary, however, because colonies were often observed far from any other visible sulfides in Alloy 25-1.

The conclusion that Type II F inclusions form as a result of cooperative growth of the sulfide and iron phases is supported by the following observations: For the most part, the secondary iron dendrite arms form a regular pattern. Figure 34a shows, however, that where the Type II F morphology occurs the iron dendrite arms grow in irregular shapes and directions. The Type II F morphology was always observed to occur within an iron dendrite arm, never in the region of the Fe-Fe<sub>3</sub>C eutectic. In contrast, the primary MnS dendrites were not observed to be favored sites for growth of iron

---

\*Cooperative growth is defined here as simultaneous growth into the melt of two phases which are in physical contact.



a



b



c



d

Figure 34: Photomicrographs of Alloy 25-1 showing the relative positions of sulfide inclusions and the iron dendrites. Light etch with 1% Nital. 2.64% Mn, 0.66% S, 3.01% C.

- a) Association of Type II F inclusions and the iron dendrites which form prior to the Fe-Fe<sub>3</sub>C eutectic, 100X.
- b) Cross-section of a Type II F inclusion, 500X.
- c) Same as b.
- d) Shows that iron dendrites grow independently of the primary MnS sulfide dendrites, in contrast to the Type II F morphology, 100X.

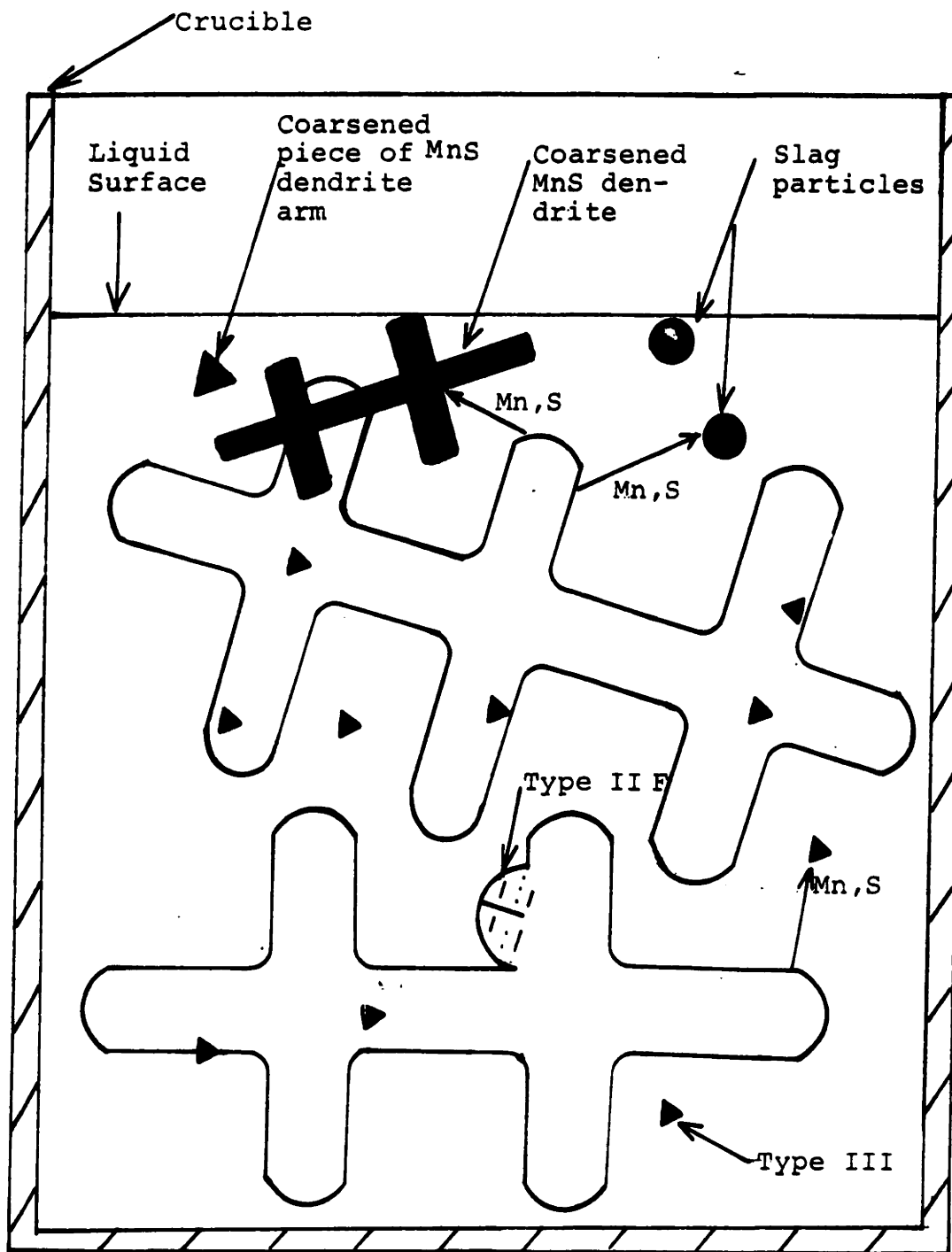


Figure 35: Formation modes of Type I, D, III and II F inclusions in high carbon or high silicon melt.

dendrites (Figure 34d). This makes it less likely that Type II F inclusions formed before the iron phase and were subsequently surrounded by it, because the usual sulfide dendrites would then also be expected to be favored sites for iron growth. A sketch of the processes which are occurring is shown in Figure 36. It is concluded that Type II F inclusions are a form of pseudo-binary eutectic in which cooperative precipitation of iron and sulfide occurs as a result of undetermined factors. They sometimes nucleate on large sulfide dendrites (Figure 23d) and are frequently observed in high-silicon alloys (Figures 26a, b, and c).

Neither Type III nor Type II F inclusions appear in the rapidly cooled parts of 25-1 or in 8-15 where fine MnS dendrites are present. It may be remembered that in the pure Fe-Mn-S system the presence of such dendrites greatly reduced the amount of rod eutectic which formed (Figure 20c). In the high carbon and silicon systems under consideration increased sulfur activity in the melt apparently causes all dissolved MnS which could form the Type II F or III inclusions to precipitate out on preexisting dendrites when cooling rates are high. At slower cooling rates, as in parts of Alloy 25-1, MnS dendrite coarsening occurs, increasing the diffusion distances to the nearest sulfide dendrite and possibly raising some local concentrations to levels needed to nucleate or grow the Type II F morphology. Such a condition has already been represented in Figure 36.

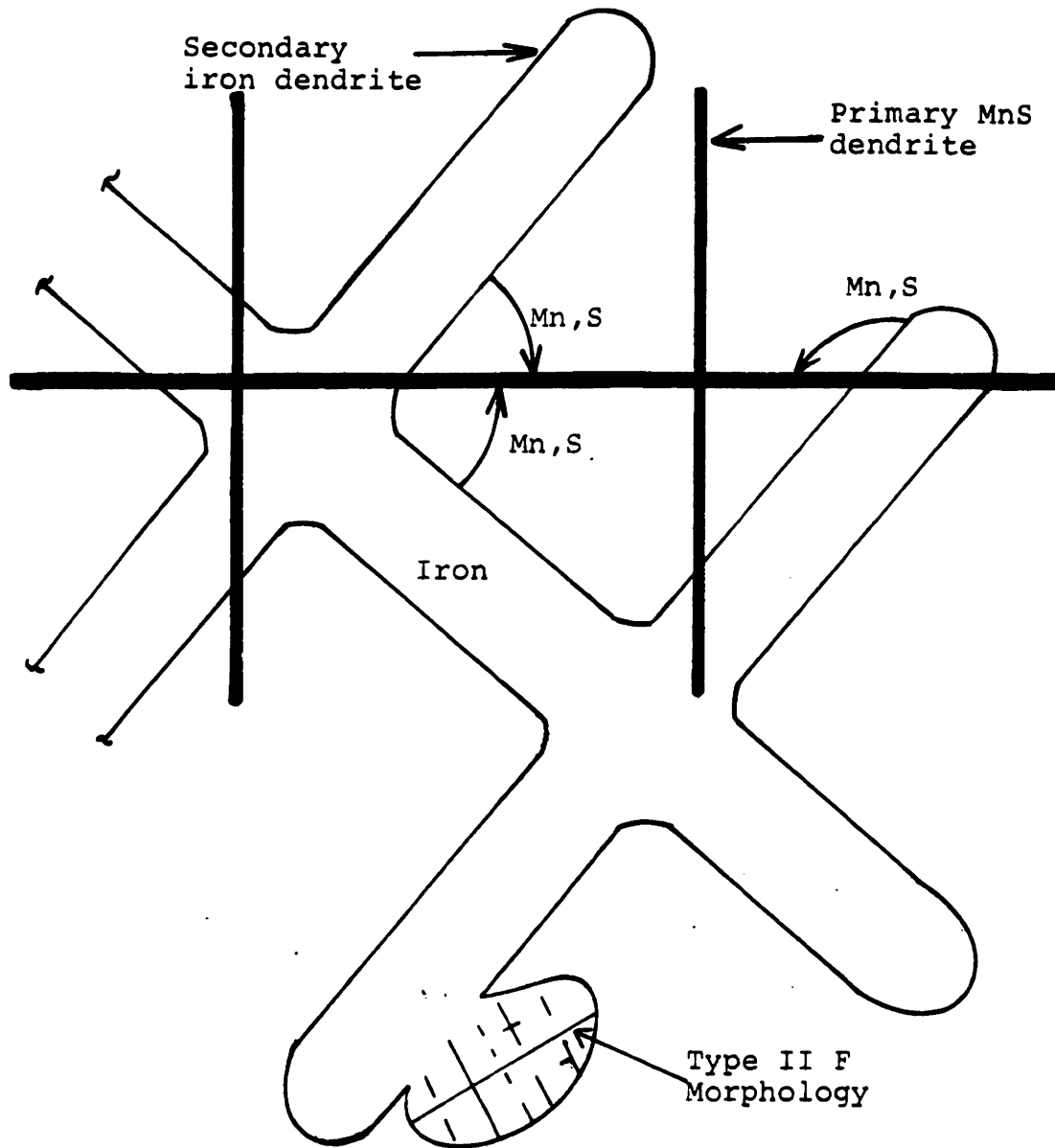


Figure 36: Model for solidification in high carbon or high silicon alloys where primary MnS dendrites form. Cooling rate in the range of  $4^{\circ}\text{C}/\text{sec}$ . Sulfide dendrites serve as sinks for manganese and sulfur rejected into melt by solidifying iron, but diffusion is rapid enough so that the coprecipitating phases are "divorced" or separated. Type II F structures precipitate by cooperative growth. Therefore they provide an easy growth mode in irregular directions, and are analogous to Type II R eutectic.

The proportion of Type III versus Type II F inclusions is apparently dependent on cooling rate. Alloys 23-2 and 24-1 were slowly cooled and produced only Type III. Alloys 23-3 and 24-2 were rapidly cooled by means of the water-cooled tube. A significant proportion of Type II F resulted. The rapid quench apparently suppressed the nucleation and growth of Type III inclusions. An example of coexistence of both types was shown in Figure 25a, which is from a section of the ingot quite far from the quench tube. This dependence of the Type III  $\rightarrow$  Type II F or Type II R transition on cooling rate was also observed by Mohla and Beech<sup>20</sup>.

Type II R inclusions were not observed in high carbon and/or silicon alloys. These alloys have a low sulfur solubility because of the effect of carbon and silicon. Conversely, Type II F inclusions are not found where the sulfur level in the liquid may reach relatively high levels as in Alloy 28-1 (Figure 27a and b) or in the alloys studied by Mohla and Beech. These compositions are in the range of commercial alloys. Type III inclusions can coexist with either II R or II F but not with both at the same time. The relative proportion of II and III inclusions in a particular ingot is dependent on cooling rate. It is concluded that the Type II R and II F inclusions are both the result of cooperative growth of the iron and sulfide phases. The Type II F morphology grows in a more dilute solution resulting in a faceted structure. The II R  $\rightarrow$  II F transition is

probably a fairly smooth function of carbon and silicon concentration. The inclusions in Figure 27b are apparently such a transition morphology. Conventional rods were found elsewhere in the same ingot. The alternative, divorced growth mode results in the precipitation of Type III inclusions.

The local solidification conditions which result in Type III formation rather than cooperative II R or II F growth are not known, except that they are influenced by cooling rate changes. However, Type III inclusions may be found close to Type II R or II F inclusions in the same ingot, which implies that cooling rate is not the only factor determining the dominant morphology. Type III inclusions along with Type II R (Figure 27) are less sharply angular and faceted than those found in high carbon and silicon alloys. This is consistent with the expectation that the Type II R and III inclusions in the low carbon and silicon alloys are precipitating from relatively sulfur-rich liquid with less tendency to cause faceting.

Confirmation of the model of dilute solution growth of Type III inclusions may be found by considering Alloy 21-3. Many Type III inclusions precipitated and rose to near the top of the ingot near where a water-cooled tube was inserted into the melt. This demonstrates that Type III can be the primary phase when the carbon content is high and sulfur content is low. These inclusions were of a larger size class

than those shown in Figure 31, which precipitated over a lower range of temperatures and sulfur content as iron dendrites began to form, and were therefore cooling rate dependent. Figure 37a shows several small inclusions entrapped at the center of a subsequently formed iron dendrite. The angularity of inclusions found near the quench tube indicates that faceting is a function of sulfur concentration, not of the cooling rate.

According to the calculations made for alloys of the composition of Example 4, Table 1, Type III inclusions should begin to precipitate by the time 35% solid iron is reached. Alloy 26-1 was made to test this prediction. Figures 37b and c show that the calculations have predicated the precipitation of Type III inclusions correctly. None were found in the center of dendrites as was the case in Alloy 21-3, but some were found fairly near the dendrite centers.

Example 5 in Table 1 predicts Type III formation. This is confirmed by Alloy 24-1 which is of a similar composition (Figure 37d). Transition of these inclusions to Type II F at higher cooling rates has already been discussed.

The late formation of sulfide inclusions predicted in Example 6 is observed in Alloys 28-1 and 28-2. Figures 38a and 43 show the coexistence of Type III and II R inclusions, which corresponds to the coexistence of Type III and II F inclusions at higher initial carbon and silicon levels. This example also shows the additive effect of carbon and



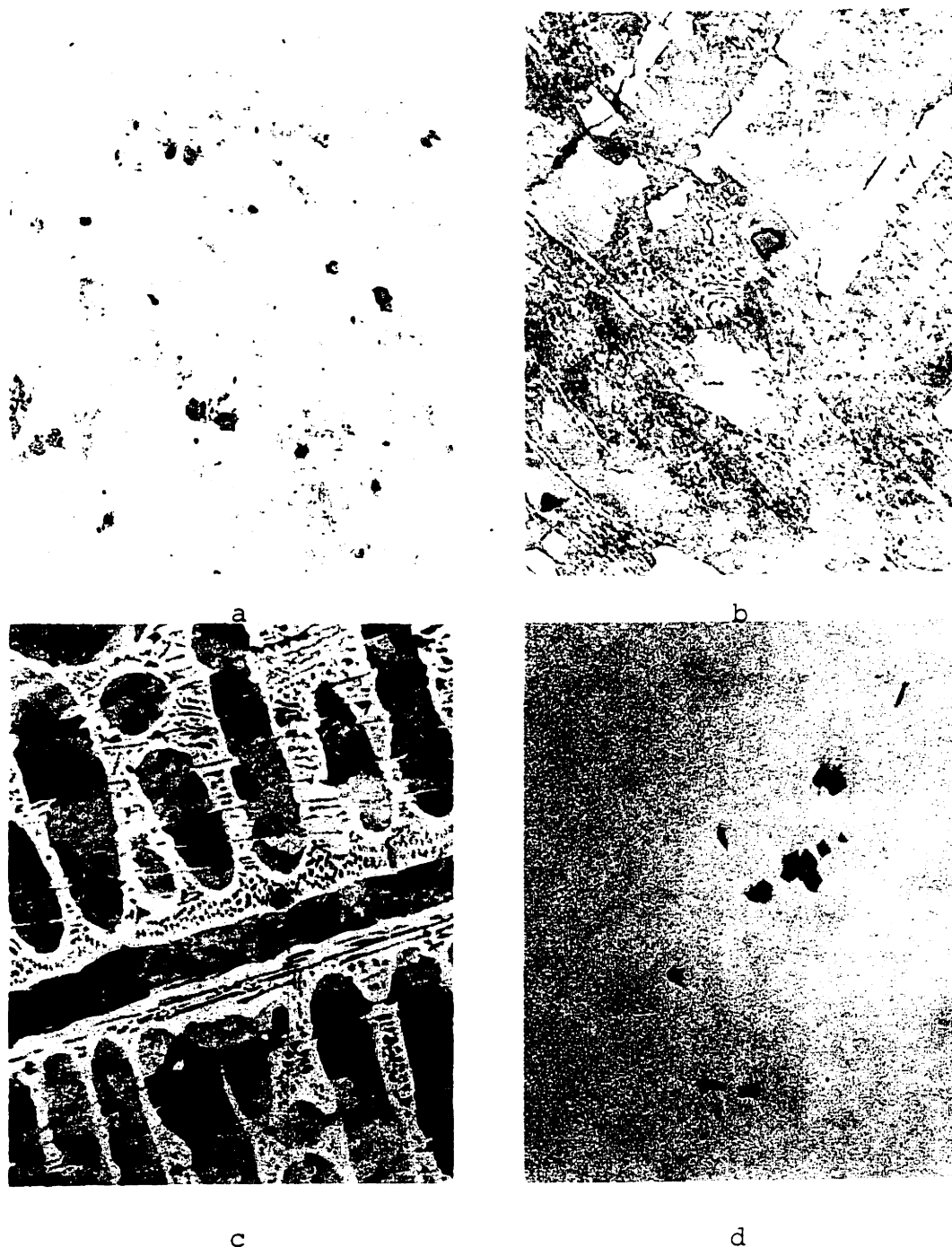
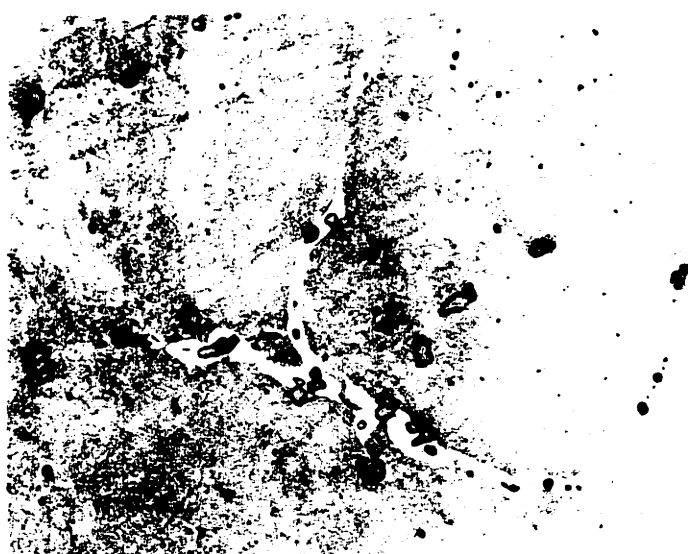


Figure 37: Type III inclusions found in alloys of the compositions used as examples in Table 1.

- a) Alloy 21-3: Type III inclusions at center of an iron dendrite, 250X. 2.5% Mn, 0.24% S, 4.4% C (Example 1).
- b) Alloy 26-1: Type III inclusion formed after precipitation of iron and entrapped by growing dendrite, 500X. (Example 4).
- c) Alloy 26-1: Same as b), but also shows Type III inclusion in interdendritic space, 200X. 0.83 Mn, 0.07 S, 3.4 C.
- d) Alloy 24-1: Type III inclusions formed at a slow cooling rate, 500X. 0.89% Mn, 0.036% S, 8% Si (Example 5).



a



b

Figure 38: Alloy 28-2 showing angular-irregular rod Type II R inclusions coexisting. Nital etch. 0.56 Mn, 0.06 S, 0.45 C, 0.46 Si.

- a) Type III inclusions formed in lower left area and Type II R along austenite grain boundary leading off to right, 500X.
- b) Ferrite forming on austenite grain boundaries does not reveal location of interdendritic segregation zones at this composition. The dark spots next to many of the inclusions are holes left when part of an inclusion segment is pulled out during polishing. 200X.

silicon is promoting Type III formation at low sulfur levels.

Entrapment of Type III inclusions by growing iron dendrites is shown in Figure 39. The horizontal line parallel to the top edge of one of the inclusions is a sulfide platelet, which was a faceted morphology occasionally observed in these high carbon alloys.

As a result of these investigations it is concluded that Type III inclusions are the result of dilute solution growth of manganese sulfide caused by high carbon or silicon levels which decrease solubility of sulfur in the liquid metal. High carbon and silicon levels may be present initially, or may result from segregation of these elements into the interdendritic liquid during solidification. Type III inclusions may therefore either be the primary solid phase or a "divorced eutectic," depending upon the initial carbon, silicon, manganese, and sulfur levels. If other additional elements are present in the melt which can further increase the activity of sulfur, formation of Type III inclusions may occur at even lower sulfur contents than those considered here. Some of these elements are phosphorous, calcium, cerium, and lanthanum. Chromium and some other elements may also have the same effect.

#### D. Fracture Research

##### 1. Effect of Morphology on Physical Properties

The test bar experiments were aimed at obtaining fracture

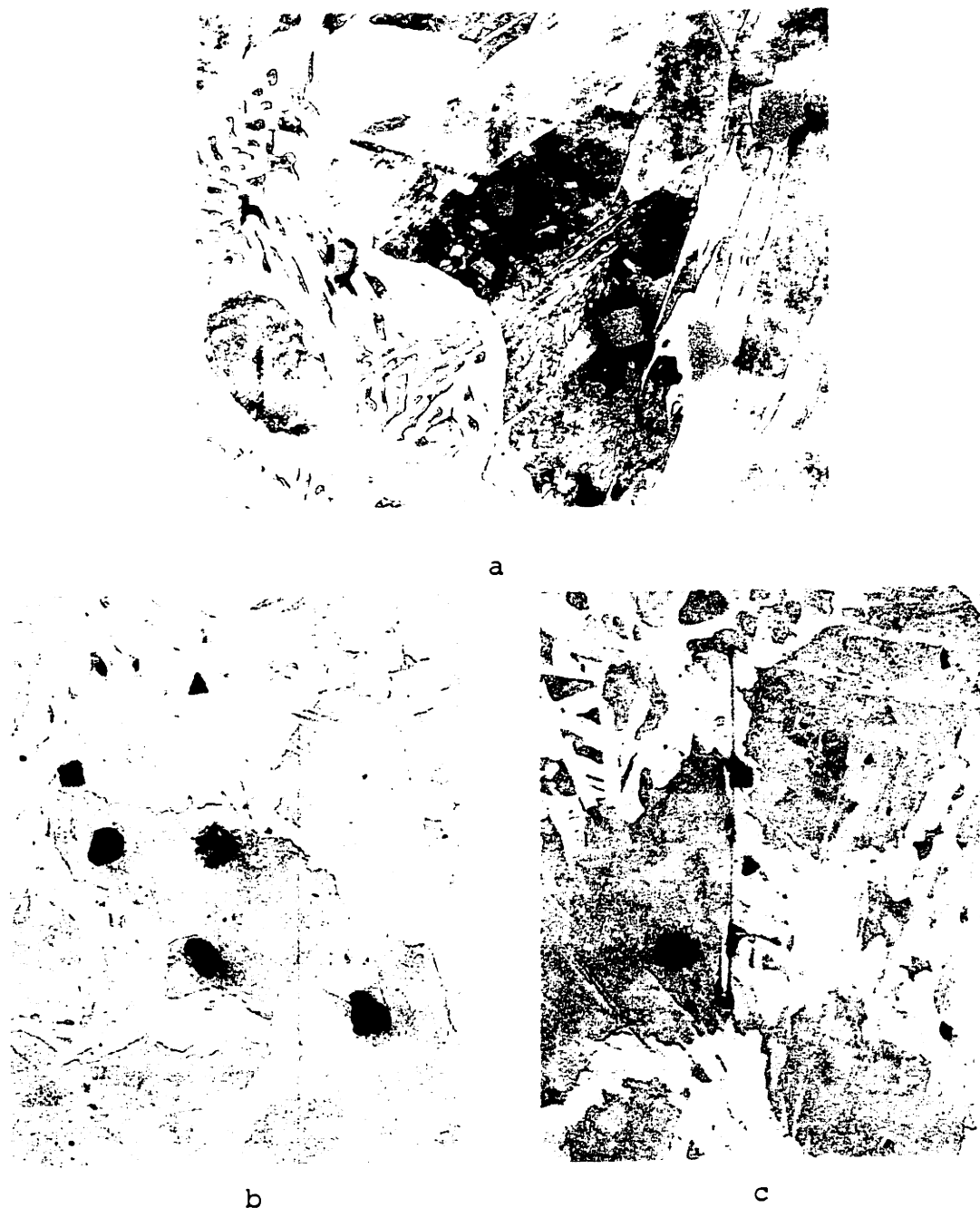


Figure 39: Type III inclusions in Alloy 25-2.

- a) Shows random location of Type III inclusions with respect to iron dendrites and Fe-Fe<sub>3</sub>C eutectic, 500X.
- b) Same, 200X.
- c) Horizontal line is an MnS platelet which apparently grew off of the square Type III inclusion, 200X.  
2.6% Mn, 0.65% S, 3.66% C.

surfaces for examination and not for properties' studies. However, a few observations can be made with respect to properties, which are listed in Table 9, along with the compositions of the specimens.

The large increase in volume fraction of inclusions between Alloys 5-5 and 5-6 does not have a detrimental effect on yield strength and ultimate tensile strength. In fact, these properties increase, probably due to a solid solution hardening effect. The presence of the inclusions makes itself felt in limiting plastic flow. The inclusions are potential nucleation sites for crack formation, and their overall distribution may be such as to assist in crack propagation. This appears in the large decrease in reduction in area between 5-5 and 5-6 although Type I inclusions are the only morphology present in either. The decrease in ductility continues in the case of Alloy 5-25, which contains only Type II R inclusions, but the effect cannot be separated here from the increased volume fraction of inclusions. The change in morphology is expected to have its greatest effect on impact strength, which was not measured.

Alloys 15-1 and 28-1 were extremely brittle, especially the high carbon and high silicon alloy, 15-1. Their physical properties are probably overwhelmingly influenced by the properties of the matrix itself and are less sensitive to inclusion morphology than alloys which have been given controlled heat treatment. Note that Alloy 28-2, which

silicon is promoting Type III formation at low sulfur levels.

Entrapment of Type III inclusions by growing iron dendrites is shown in Figure 39. The horizontal line parallel to the top edge of one of the inclusions is a sulfide platelet, which was a faceted morphology occasionally observed in these high carbon alloys.

As a result of these investigations it is concluded that Type III inclusions are the result of dilute solution growth of manganese sulfide caused by high carbon or silicon levels which decrease solubility of sulfur in the liquid metal. High carbon and silicon levels may be present initially, or may result from segregation of these elements into the interdendritic liquid during solidification. Type III inclusions may therefore either be the primary solid phase or a "divorced eutectic," depending upon the initial carbon, silicon, manganese, and sulfur levels. If other additional elements are present in the melt which can further increase the activity of sulfur, formation of Type III inclusions may occur at even lower sulfur contents than those considered here. Some of these elements are phosphorous, calcium, cerium, and lanthanum. Chromium and some other elements may also have the same effect.

#### D. Fracture Research

##### 1. Effect of Morphology on Physical Properties

The test bar experiments were aimed at obtaining fracture

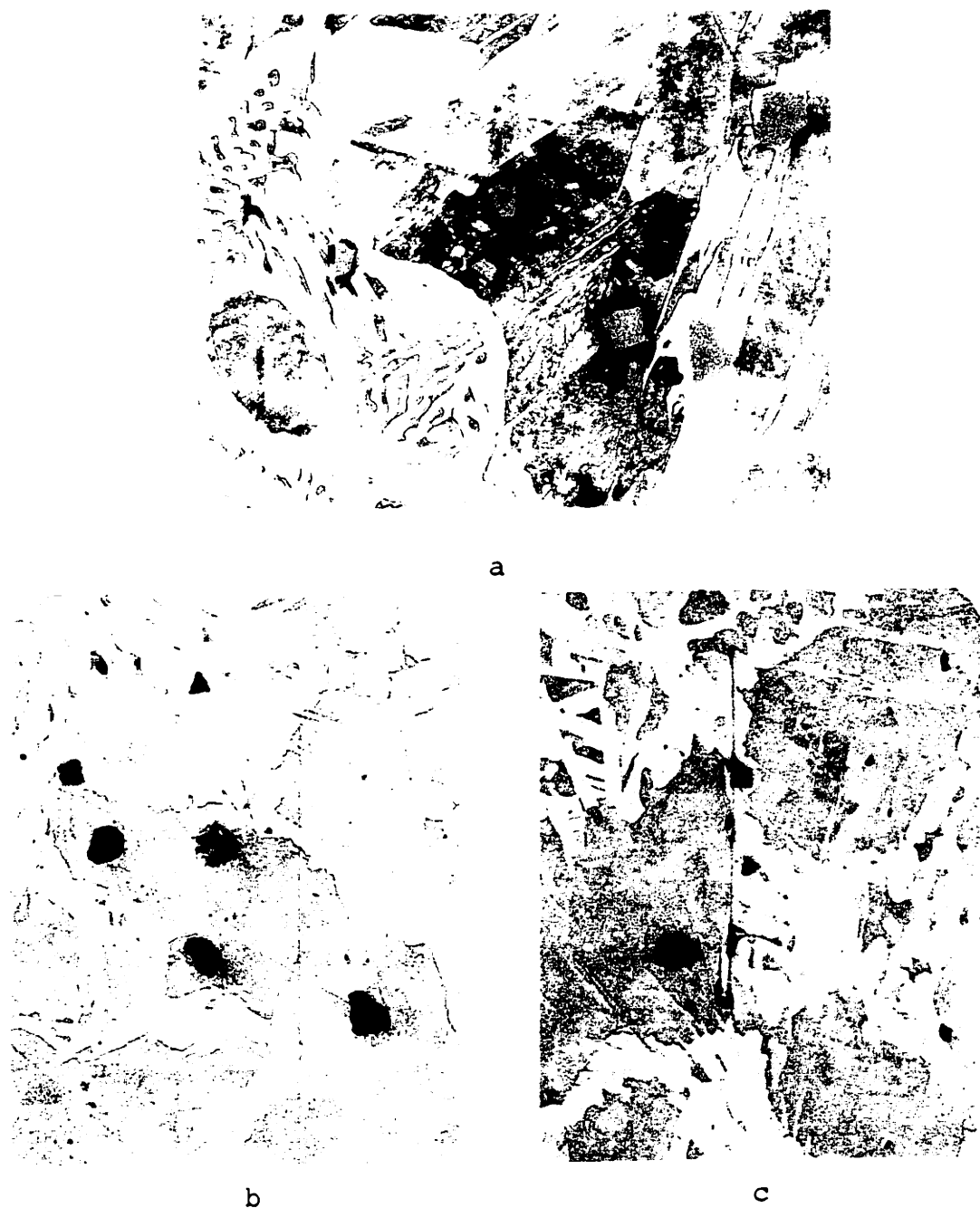


Figure 39: Type III inclusions in Alloy 25-2.

- a) Shows random location of Type III inclusions with respect to iron dendrites and Fe-Fe<sub>3</sub>C eutectic, 500X.
- b) Same, 200X.
- c) Horizontal line is an MnS platelet which apparently grew off of the square Type III inclusion, 200X.  
2.6% Mn, 0.65% S, 3.66% C.

surfaces for examination and not for properties' studies. However, a few observations can be made with respect to properties, which are listed in Table 9, along with the compositions of the specimens.

The large increase in volume fraction of inclusions between Alloys 5-5 and 5-6 does not have a detrimental effect on yield strength and ultimate tensile strength. In fact, these properties increase, probably due to a solid solution hardening effect. The presence of the inclusions makes itself felt in limiting plastic flow. The inclusions are potential nucleation sites for crack formation, and their overall distribution may be such as to assist in crack propagation. This appears in the large decrease in reduction in area between 5-5 and 5-6 although Type I inclusions are the only morphology present in either. The decrease in ductility continues in the case of Alloy 5-25, which contains only Type II R inclusions, but the effect cannot be separated here from the increased volume fraction of inclusions. The change in morphology is expected to have its greatest effect on impact strength, which was not measured.

Alloys 15-1 and 28-1 were extremely brittle, especially the high carbon and high silicon alloy, 15-1. Their physical properties are probably overwhelmingly influenced by the properties of the matrix itself and are less sensitive to inclusion morphology than alloys which have been given controlled heat treatment. Note that Alloy 28-2, which



TABLE 9.

Alloy	Wt %				psi x 10 <sup>-3</sup>			Elonga- tion	Reduction in Area	%
	Mn	S	O	C	Si	Al	Y.S.			
5-5	0.12	0.07	0.01				19.6	28.0	36.2	96
5-6	0.52	0.20	0.029				20.0	32.6	19	25
5-25	1.50	0.51	0.0046			0.053	19.3	27.2	10	-
15-1	2.70	0.15	0.002	1.56	2.10		111	111	0	0
28-2	0.56	0.06	-	0.41	0.47	0.03	61	92	5	-

contain mostly Type II R inclusions is more ductile than the Type III-bearing specimen, demonstrating that inclusion morphology is only one of many factors influencing fracture behavior.

## 2. Inclusion Shrinkage

Figure 40b shows dimples or depressions found on the surface of some Type I inclusions. This is convincing evidence that these inclusions were still liquid when the metal solidified around them in accordance with the theory of Type I formation developed earlier in this Chapter. Figure 44a shows a similar depression found in an inclusion on the polished surface of an undeformed piece of Alloy 5-6. The dimples are therefore caused by solidification shrinkage when the inclusions freeze as liquid droplets entrapped within solid iron. Pure MnO inclusions have a higher melting point than iron, so that shrinkage when they solidify is in-filled by the iron (Figure 21a), as is the case for the large Type I slag inclusion in the deoxidized system (Figure 17c). The present Type I inclusions, which are the variety observed in commercial alloys, contain an appropriate proportion of oxygen and sulfur so that they freeze after the iron and therefore are not in-filled.

Thermal expansion, mentioned above, is another factor which causes inclusion shrinkage and may be important in determining properties. MnO is known to have a similar

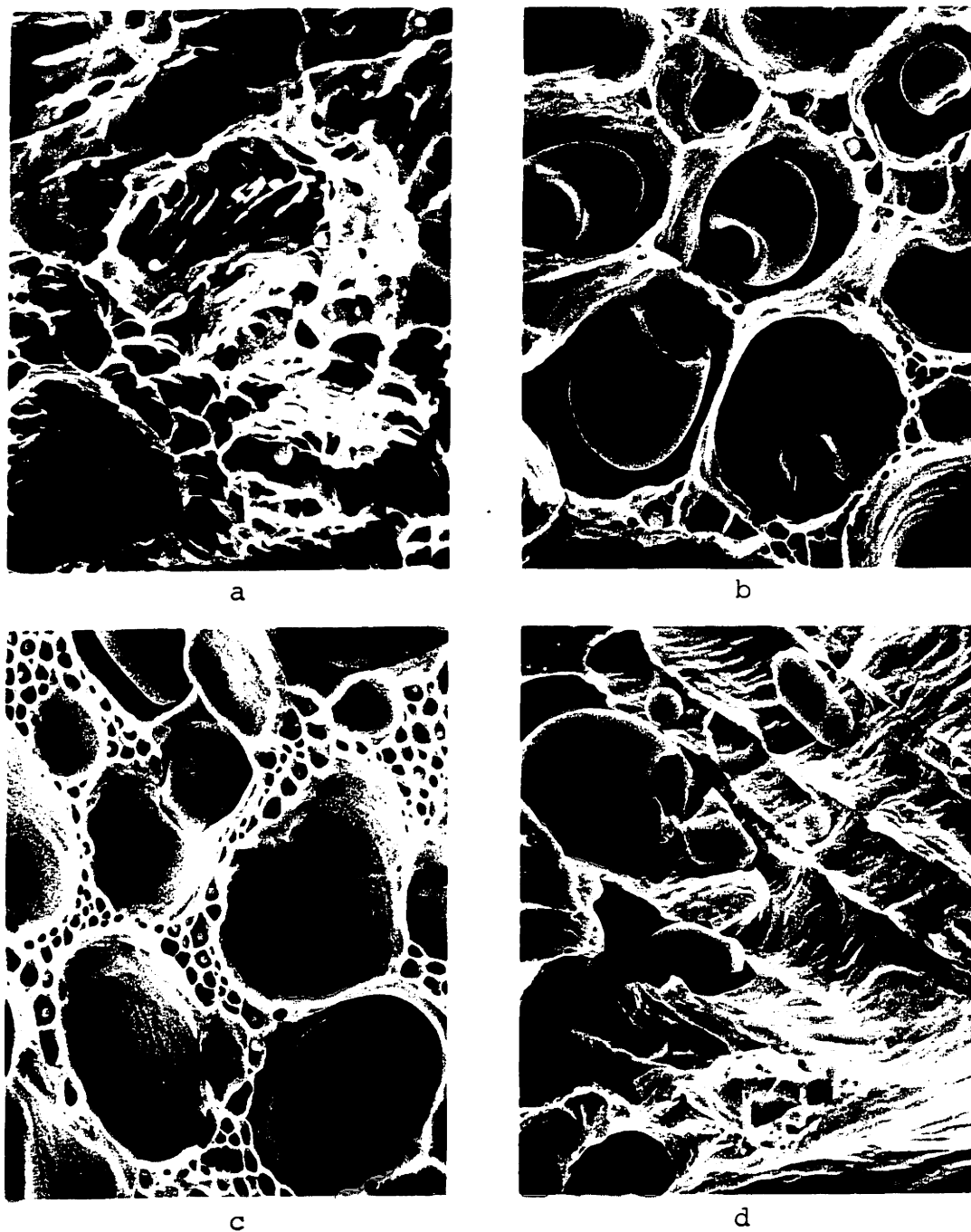


Figure 40: Scanning electron microscope pictures of Type I inclusions in fracture surface of Alloys 5-5 and 5-6. Table 9.

- a) Alloy 5-5: Dimples and a few small Type I inclusions, 1600X.
- b) Alloy 5-6: Large Type I inclusions with shrinkage depressions, 1600X.
- c) Alloy 5-6: Large irregular Type I inclusions surrounded by regions containing many smaller spherical inclusions, 1600X.
- d) Alloy 5-6: Fractured and displaced Type I inclusions at border between necked region and fracture surface. Direction of tension is diagonal from lower right to upper left, 1550X.

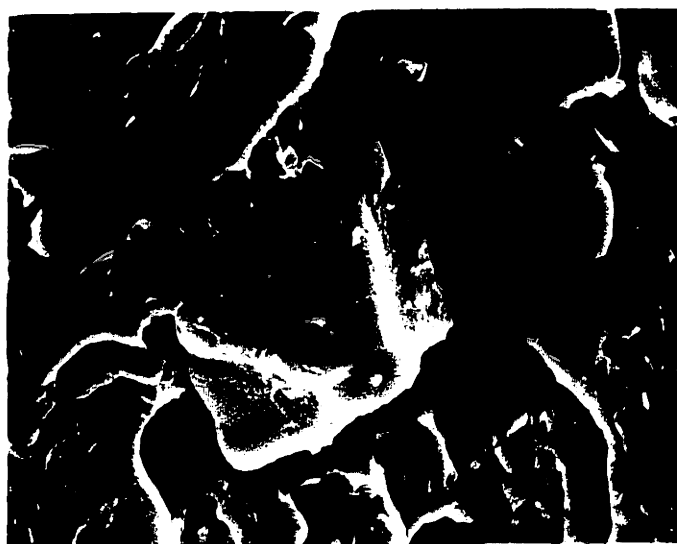


Figure 41: Scanning microscope pictures of fracture surface of Alloy 5-25, containing Type II R inclusions. Table 9.

- a) Eutectic colony growth pattern, 290X.
- b) Same, 680X.
- c) Shows that Type II R inclusions are rods. At intersection of two colonies a single row of rods with their own orientation often appears, as seen here, 725X.
- d) Enlargement of ends of rods in a colony which grew normal to plane of paper. Note apparent cleavage feature of rods, and that the cleavage planes are the same for all. This indicates that they all grew from one nucleus, 7225X.



a



b

Figure 42: Inclusion morphology in Alloy 15-1. Table 9.

- a) Photomicrograph of polished surface of as-cast ingot. Note large gaps between metal and inclusion, and that pieces have apparently been broken off during polishing, 500X.
- b) Scanning electron microscope picture of an apparently cubic inclusion (Type III) found in the fracture surface of a test bar. The matrix-inclusion separation is also present here. The metal broke with almost no plastic deformation, 2700X.

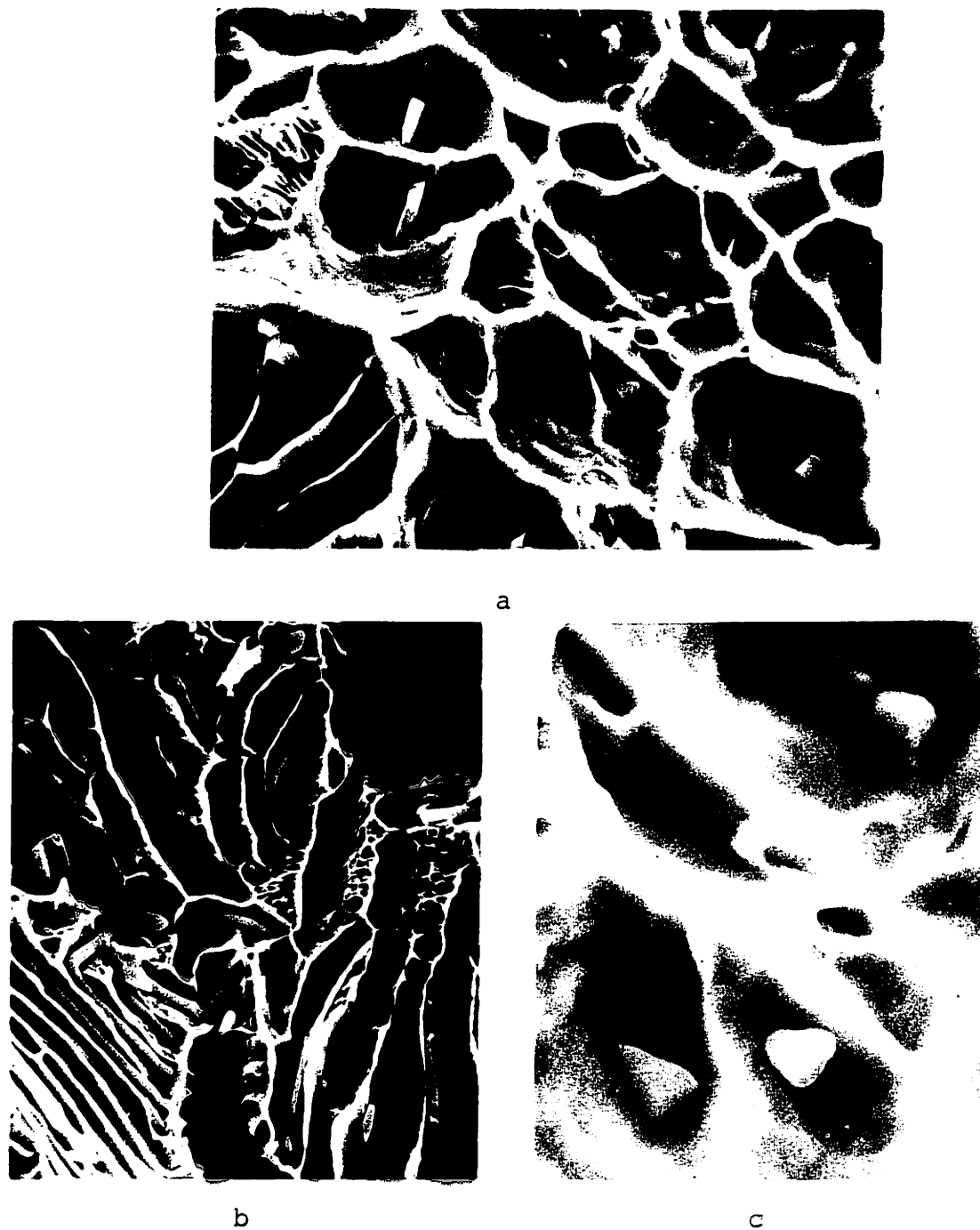


Figure 43: Scanning microscope pictures of inclusion morphology in fracture surface of Alloy 28-2. Table 9.

- a) Coexistence of angular Type III inclusions with rod-like inclusion, 3160X.
- b) Dominant Type II R morphology found in fracture surface, 1560X.
- c) Type III inclusions, 7800X.

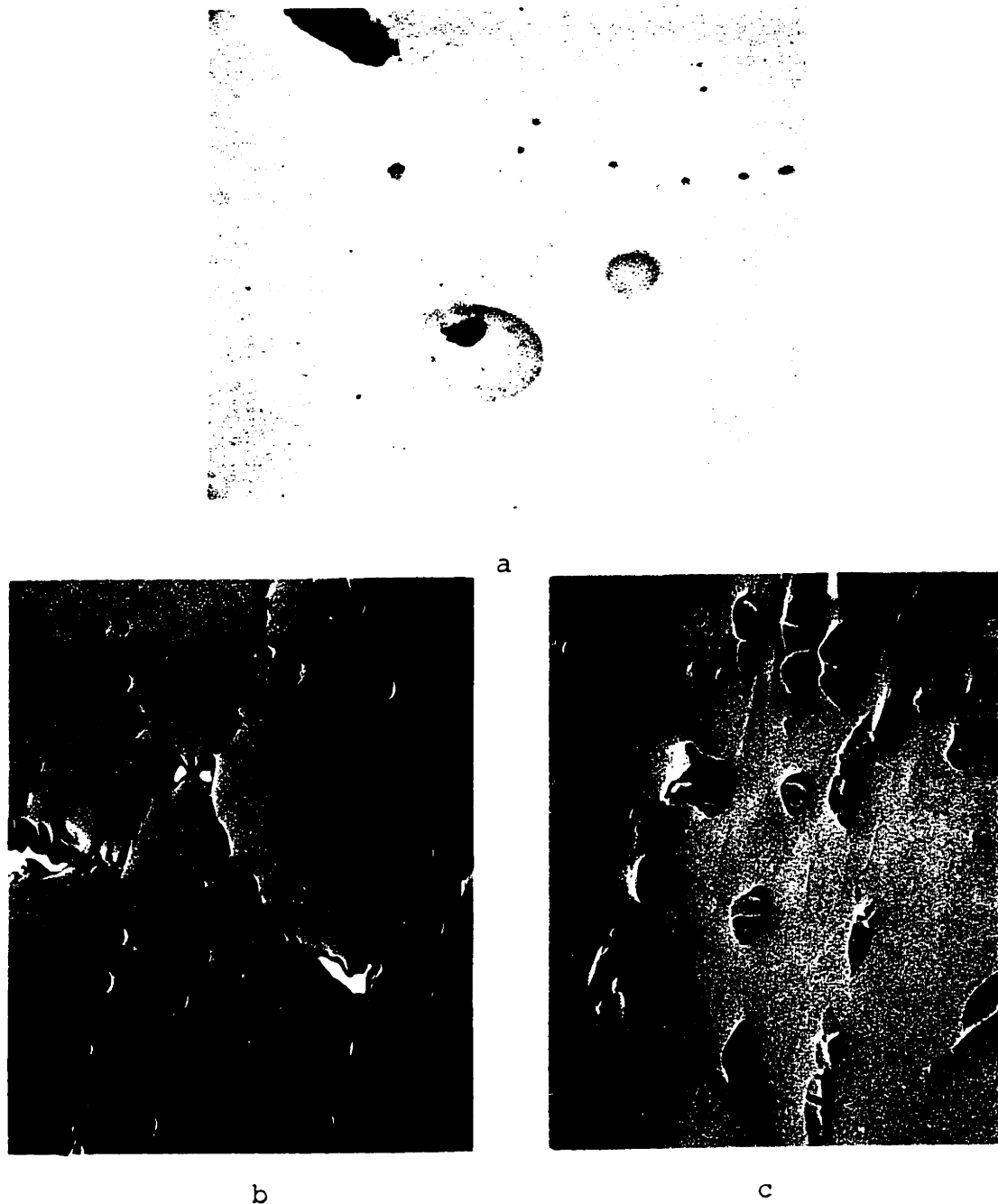


Figure 44: Scanning microscope pictures of polished surface of Alloy 5-6. Table 9.

- a) Undeformed test bar: Shows that dimples in large Type I inclusions are not caused by deformation of the matrix, 2000X.
- b) Deformed area in necked region next to fracture surface: Shows serrated fracture path joining a series of inclusions. Tensile direction is parallel to long edges of picture, 200X.
- c) Area near b): Shows fractured inclusions and void formation caused by plastic flow, 500X.

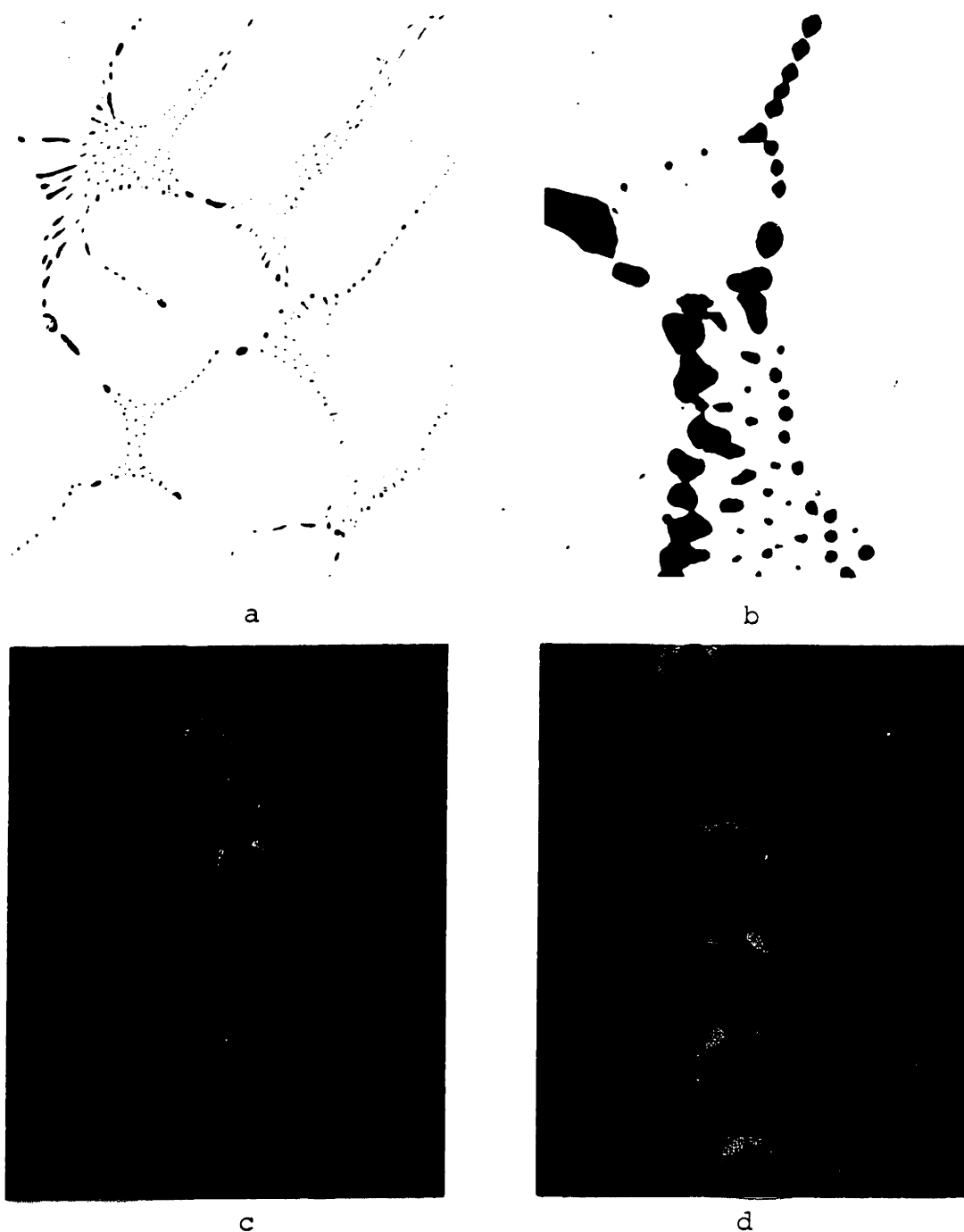


Figure 45: Fracture mode caused by Type II R inclusions in Alloy 5-25. Table 9.

- a) Photomicrograph of Type II R inclusions in undeformed specimen, 250X.
- b) Photomicrograph of polished surface of test bar pulled until necked. Tensile direction from left to right. Shows incipient cracks and start of fracture path connecting rod inclusions, 750X.
- c) Scanning microscope photograph of crack growth from voids formed around rods. Same tensile direction as b), 2000X.
- d) Same as c): Shows that the rods have been separated from the matrix, 5000X.



coefficient of thermal expansion to that of iron, while MnS shrinks more rapidly<sup>81</sup>. Type I inclusions, containing some MnO as well as MnS, may be more able to retain contact at the interface than Type II R rods consisting of pure MnS, especially since the latter must maintain coherence over the length of the rod. It seems probable, however, that both types are separated from the matrix at room temperature and act as voids until deformation of the metal causes it to press against them. The voids around Type II R inclusions provide a more closely spaced and extensive (lengthwise) set of stress risers and therefore are more detrimental to ductility.

The Type III inclusions in Alloy 15-1 were very difficult to retain in the surface when polishing in contrast to the other alloys containing Type III. They were either very soft and crumbly or were separated from the matrix by shrinkage after solidification. The latter appears to be the case. Figure 42b shows the separation which existed between inclusion and matrix in the fracture surface. Because of the extreme brittleness of the metal the fracture path did not follow a path joining inclusions. Whereas in all the other cases the area fraction of inclusions in the fracture surface was much higher than on a random polished surface, this was not the case in Alloy 15-1. Little or no deformation occurred around those inclusions which were observed, and angular holes were found where others had apparently rested before falling out at fracture. The principle of inclusion shrinkage is

demonstrated by this behavior. The angular morphology of Type III inclusions is also revealed in the scanning microscope pictures.

### 3. Eutectic Formation

Research by others in the Fe-C system has revealed, by a laborious polishing-down process, that the carbide phase in pearlite is interconnected and actually consists of a single crystal of  $\text{Fe}_3\text{C}$  growing in a cooperative inter-penetrating manner with the iron. Each colony represents one nucleation event for each phase. A similar situation is expected to occur in the case of rod eutectics. The scanning electron microscope reveals this to be the case. Figure 41d shows that the rods have fractured by cleavage along cubic crystallographic planes. Furthermore, the cleavage planes are parallel. These rods were part of a single colony. Other colonies were fractured on internally parallel planes but those planes were of a different orientation than the ones shown here. The only way this can occur is if the sulfides in each colony are part of the same sulfide crystal. It is therefore concluded that the rods are interconnected and that they grew from a single nucleus.

### 4. Deformation and Fracture of Inclusions. Crack Propagation.

Figure 44c shows that Type I inclusions may be fractured by compressive stress during the process of deformation. The

demonstrated by this behavior. The angular morphology of Type III inclusions is also revealed in the scanning microscope pictures.

### 3. Eutectic Formation

Research by others in the Fe-C system has revealed, by a laborious polishing-down process, that the carbide phase in pearlite is interconnected and actually consists of a single crystal of  $\text{Fe}_3\text{C}$  growing in a cooperative inter-penetrating manner with the iron. Each colony represents one nucleation event for each phase. A similar situation is expected to occur in the case of rod eutectics. The scanning electron microscope reveals this to be the case. Figure 41d shows that the rods have fractured by cleavage along cubic crystallographic planes. Furthermore, the cleavage planes are parallel. These rods were part of a single colony. Other colonies were fractured on internally parallel planes but those planes were of a different orientation than the ones shown here. The only way this can occur is if the sulfides in each colony are part of the same sulfide crystal. It is therefore concluded that the rods are interconnected and that they grew from a single nucleus.

### 4. Deformation and Fracture of Inclusions. Crack Propagation.

Figure 44c shows that Type I inclusions may be fractured by compressive stress during the process of deformation. The

picture was taken in a plastically deformed region. Voids may be seen associated with some of the inclusions. These mechanically created voids occurred without exception on the tensile side of the inclusions. They often formed sharply pointed conical voids pointing in the direction of tension. The voids were most angular and large when they were found at the ends of inclusions which had been deformed by compressive stresses during yield, but which had not fractured. When an inclusion was broken local deformation was able to occur by separation of the two halves and formation of a void between them. The ends of the inclusion remain much more nearly in contact with the matrix than in the case of an unfractured inclusion, and sharply pointed voids do not form. Rounded voids on the tensile side are sometimes observed with fractured inclusions. These were presumably formed prior to fracture of the inclusion. As deformation proceeds the voids around the inclusion may grow until they join, forming a large crack and causing fracture (Figure 44b).

Figure 45 shows how the process occurs with Type II R inclusions. Because the inclusions are close together and lined up in a row the associated voids can grow directly from one to another (Figure 45c). Type I inclusions first form conical voids on the tensile sides, which cannot easily grow normal to the tensile direction unless another similar void has formed nearby. Such a situation is preexistent in the case of Type II R inclusions. Furthermore, when the

voids along the rods grow together they probably do so along a considerable length, sweeping out a large area of separated metal. Voids around Type I inclusions, being essentially point sources rather than line faults, open up a much smaller area when joining with other inclusions, unless a number can cooperate. When these factors are considered it is easy to see why Type II inclusions are so detrimental to ductility and impact strength. Just a few of them in a row can open up a very large crack.

## VIII. DISCUSSION

### A. Inclusion Formation

#### 1. Type I Inclusions

Type I sulfides (with one exception noted later) are spherical inclusions which contain oxygen and are found in the interdendritic regions of commercial alloys with appropriate concentrations of sulfur and oxygen. Depending upon the overall composition they may consist of one or more phases. Examples of the Type I inclusions obtained in this research are shown in Figures 21 and 22a and c.

There is general agreement in the literature that Type I inclusions result from the presence of oxygen in the melt<sup>5,13,14,17,19</sup>. A few attempts have been made to explain this effect. Hilty and Crafts<sup>29</sup> generated some quantitative data on the Fe-Mn-S-O system, and Dahl et al<sup>17</sup> proposed a model for Type I formation based upon a pseudo-ternary Fe-MnS-MnO phase diagram. The present research has undertaken a qualitative consideration of the Fe-Mn-S-O quaternary. Three isothermal sections at 1% Mn are derived and presented in Figures 5, 6, and 7. Modification of these diagrams by manganese content changes are also considered. The conclusion which has been drawn is that although Hilty and Crafts'<sup>29</sup> diagram is qualitatively incorrect in some of its details, and although Dahl's model is somewhat oversimplified, the mechanism of Type I formation they imply is essentially correct. This mechanism is the secondary precipitation of low-melting slag droplets containing manganese, iron, oxygen, and sulfur due to segregation in the

interdendritic regions. The small spherical droplets are subsequently entrapped by the thickening dendrite arms, resulting in their observed interdendritic distribution. There is evidence that they are usually still liquid when entrapped. This is based upon solidification shrinkage depressions on their surfaces observed with a scanning electron microscope (Figure 40).

It has also been shown here that at higher sulfur levels than are common in commercial alloys oxide-bearing Type I inclusions can form as a primary liquid slag phase which coexists with Type II R and Type II S inclusions. These morphologies are discussed further in the next section of this Chapter.

A third type of spherical sulfide inclusion was obtained in the present research which forms under conditions not found in commercial alloys (Figure 17c). These inclusions were designated Type I here because of their spherical morphology. They do not require oxygen for their formation, as do the usual Type I's, and are the exception noted above. They result when the miscibility gap in the Fe-Mn-S system is intersected (Figure 10). This requires sulfur levels higher than those usually present in commercial alloys. The Type I morphology consists of nearly stoichiometric manganese sulfide, and freezes at a higher temperature than iron. If the melt is not stirred they float to the surface. It has been shown that these slag droplets freeze with little undercooling. A mechanism of freezing has been proposed which can account for the occluded iron often contained in them.

## 2. Type II R Inclusions

Rod eutectic Type II R inclusions have been shown to result from precipitation along the line of two-fold saturation adjacent to the Fe-Mn side of the Fe-Mn-S system. They result from cooperative growth\* into the interdendritic liquid of solid MnS and solid iron, as sketched in Figure 32. Figure 8b shows the path on the phase diagram taken by the liquid. Examples of these inclusions are shown in Figures 19d and 30a and b. Type II R inclusions can also form for a limited distance along the line of two-fold saturation on the Fe-FeS side of the diagram before generating into irregular rods and sheetlike Type II S inclusions when the liquid becomes sufficiently depleted of manganese. This transition is discussed further in the next section. An example is shown in Figures 33a and b.

The present research utilizes both aluminum additions and a vacuum-carbon boil as methods of deoxidation to convert inclusion morphology from Type I to Type II R. Sims, Saller and Boulger<sup>9</sup> had concluded that this transition was a function of oxygen level. Dahl, Hengstenberg and Duren<sup>17</sup> have also concluded the same thing. The present research is the first which uses high-purity materials and vacuum-melting techniques to confirm this oxygen dependency for a large range of sulfur and manganese compositions, and over a range of cooling rates.

---

\* Cooperative growth is defined here as simultaneous growth into the melt of two phases which are in intimate physical contact.



The oxygen levels which have been obtained are lower than those achieved by most of the other researchers. Elliot<sup>85</sup> has pointed out that the theoretical equilibrium deoxidizing power of the oxygen-carbon and oxygen-aluminum reactions are rarely approached in practical situations. Nevertheless the oxygen levels attained here in deoxidized melts are generally within an order of magnitude of those in zone-refined iron. They are an order of magnitude less than those used by Dahl<sup>17</sup> in his research.

It has been shown here that at high sulfur levels not usually present in commercial alloys oxide-bearing Type I, and pure Type II R, and Type II S inclusions can all coexist in the same ingot (Figures 33c and d). The oxide phase is concentrated in the Type I inclusions which are primary slag droplets resulting from the intersection of a miscibility gap. Type II R and Type II S inclusions subsequently form when the iron begins to precipitate. This sequence of events is explained in terms of qualitative sections of the Fe-Mn-S-O quaternary (Figures 5, 6 and 7). Formation of the usual Type I secondary droplets without Type II R inclusions is also explained in terms of these diagrams. The Type I to II R transition in this latter case is a sensitive function of oxygen content, as found by Sims and Dahle<sup>5</sup>, because at the low sulfur levels applicable small changes in oxygen level have a large effect on the important O/S ratio. At larger sulfur levels the transition to the "deoxidized" state is more gradual.

### 3. Type II S Inclusions

Type II S sulfides are irregular sheet-like inclusions which form along the line of two-fold saturation on the Fe-FeS side (Figure 11). As was pointed out above, Type II R inclusions also form to a limited extent along this line when the composition is near the maximum in the iron corner. When the Mn/S ratio falls below a value which has not been precisely determined, the cooperative growth mode which produces these rod inclusions breaks down and they degenerate into irregular rods and finally at low manganese levels into the irregular sheet-like structure which has been designated Type II S. The Type II S inclusions are formed in the dendrite interstices. They may be duplex in structure, with part of the sheet consisting of FeS and part of a mixed (Fe, Mn)S sulfide. The mixed sulfide tends to be more bulky or spherical in shape than FeS, leading to a serrated appearance in some cases with bulges of the mixed sulfide connected by a sheet of the iron sulfide phase (Figures 17a and 18b). The classic Type II S morphology in which a film of sulfide completely surrounds the dendrite arms is obtained when manganese is absent (Figure 20a). If small amounts of manganese are present this morphology may still be obtained, but as the manganese content rises further (Mn, Fe)S begins to precipitate as a chunky or bulky solid phase in the interdendritic liquid and the sulfide is no longer a smooth film.

Yarwood<sup>31</sup> has thoroughly studied the Fe-S-O system, and has also come to the conclusion that the sulfide sheet morphology results from solidification at compositions along or near the Fe-FeS binary. He found that O/S ratios greater than 0.05 in the Fe-S-O system produce some spherical inclusions through the intersection of a miscibility gap. Sims, Saller and Boulger<sup>10</sup> suggested the possibility that lowered surface tension is responsible for spreading of the sulfide between the dendrite arms. Van Vlack<sup>59</sup> found that oxygen increased the surface energy of sulfide liquid between iron grains held for several hours at 1200°C. Such an effect probably does have some effect on allowing the final liquid which solidifies to spread between dendrite arms rather than to ball up somewhat into thicker and less extensive sheets in both the Fe-S-O system and the present Fe-Mn-S system. Nevertheless, the primary reason for the Type II S morphology is that it forms from the last liquid to solidify in the sheet-like interdendritic interstices.

Little attention has been given in the literature to sulfide formation on the Fe-FeS side of the Fe-Mn-S diagram. This may have been due in part to the fact that the phase diagram in this area was not even qualitatively known. The present research has developed evidence for a version of the phase diagram in which the eutectic valley is not intersected by the miscibility gap. This diagram is in opposition to the version commonly used in the literature to describe sulfide

behavior<sup>15,25,27,29</sup>, and agrees with a version originally proposed by Vogel<sup>26</sup> (Figures 2 and 3). The commonly accepted diagram, in which the miscibility gap intersects the eutectic, leads to the expectation that liquid slag droplets would form in the liquid metal when the four-phase plane is encountered. Such droplets are expected to be spherical, and to be entrapped by the thickening iron dendrite arms in the manner observed by Yarwood<sup>31</sup> in the Fe-O-S system. When alloys in the appropriate composition range are solidified, however, such droplets are not observed. Directional solidification produces instead a coarse degenerate mixed sulfide eutectic which is parallel to the heat flow direction and is consistent with the expected structure in the Vogel version (Figure 30c). When thermal gradients are small the structure becomes even more irregular and divorced eutectic particles of irregular composition and shape precipitate, along with Type II S duplex morphologies (Figure 30d).

#### 4. Type II F Inclusions

Type II F inclusions (faceted Type II inclusions) consist of somewhat irregular arrays of sulfide platelets which form at high carbon and silicon levels. An example of this morphology is shown in Figure 23c. They have not been reported elsewhere in the literature.

Evidence has been presented that the structures represent a form of cooperative growth which occurs at compositions also producing Type III inclusions. Formation of the angular Type III inclusions is described later. The details of Type II F formation are not completely understood. However, experimental evidence indicates that they are the dilute solution analog of Type II R, resulting from the presence of carbon and silicon. The tendency to precipitate along specific crystallographic planes has been related in the literature<sup>78</sup> to growth from a dilute solution, among other factors. The relative amounts of Type II F and Type III inclusions is dependent upon the cooling rate. This behavior is discussed further in the next section.

##### 5. Type III Inclusions

Type III inclusions are angular sulfides resulting from dilute solution growth in alloys containing carbon, silicon, or other elements which strongly decrease the solubility of sulfur. Examples of this morphology are shown in Figure 23a and b. Evidence has been presented here that the inclusions can be the primary solid phase in very high carbon alloys. However, in all important commercial alloys they precipitate by a divorced growth mechanism as the secondary phase in the dendrite interstices after segregation of manganese, sulfur, carbon, silicon, etc., has caused the limit of sulfur solubility to be reached. They grow as a separated

or "divorced" phase in a region of two-fold saturation and are frequently entrapped by the thickening iron dendrite arms (Figures 37b and c). They do not occur in the pure Fe-Mn-S system.

Dahl<sup>17</sup> proposed that Type III inclusions are the primary solid phase. He proposed that carbon or silicon make this possible by reducing the solubility of sulfur and extending the liquid state to lower temperatures. This would cause a typical alloy composition which would have fallen in the primary iron region and resulted in Type II R inclusions without carbon or silicon now to fall in the region of primary precipitation of sulfide. His model does not explain why angular sulfides instead of dendrites result, why Type II R inclusions do not form when iron begins to solidify, or how Type III inclusions could form at the relatively low alloy compositions observed commercially.

The present research has found that dendrites can in fact occur when sulfur levels are high enough so that the field of primary MnS precipitation is intersected. This is discussed further in the next section. In most cases Type III inclusions do not form as the primary phase but as a "divorced" eutectic in the interdendritic segregation zones. Their angular shape is the result of growth in a dilute solution. Dahl's essential idea of the effect of carbon and silicon on the sulfide solubility is seen to be correct. However, the present research has corrected a few false

conclusions he drew and has elucidated the solidification processes involved. It has also extended the study of Type III formation to lower phosphorous and oxygen levels.

It was mentioned earlier that cooling rate has an effect on the relative amounts of Type III and Type II F inclusions. Higher cooling rates favor the proposed cooperative growth mode producing Type II F inclusions, although both types may be found together in the same region of an ingot where cooling rates are uniform. This implies that cooling rate is not the only factor involved. It is not known what other variables are important.

Mohla and Beech<sup>20</sup> have observed a similar effect of cooling rate on the transition from Type III to Type II R inclusions at relatively low carbon and silicon levels. Type II R are favored by high cooling rates as are the II F inclusions of the present research. This supports the concept that II R and II F inclusions result from a similar mechanism, cooperative growth of the sulfide and iron phases, whereas Type III inclusions result from divorced or separated growth at lower cooling rates. Type II R inclusions transform to the more faceted, crystallographically oriented Type II F morphology if carbon or silicon levels are increased, causing the sulfide to precipitate from a more dilute solution.

Type III inclusion growth requires that the melt exceed its saturation level of sulfur. At high concentrations

of carbon and silicon this may occur just prior to formation of iron dendrites, resulting in primary precipitation of Type III inclusions. Type II R and II F however can only be secondary since they require simultaneous formation of iron. In almost all cases, Type III inclusions are also secondary. The two basic types, II and III, may therefore be said to result from different modes of simultaneous precipitation of solid iron and solid sulfide. One mode is cooperative and requires physical contact while the other mode is divorced and separate.

The presence of aluminum was found to be unnecessary for the formation of Type III inclusions. This is in agreement with the results of Dahl<sup>17</sup>. Sims<sup>13</sup> has reported, however, that additions of more than 0.01% Al can sometimes convert Type II inclusions to Type III in commercial alloys. This evidently results not from any deoxidation effect, or from formation of aluminum sulfide, but from the effect of aluminum on sulfur activity in the melt. Aluminum, and also phosphorous, are known to increase the activity coefficient of sulfur. Their effects are considerably weaker than those of carbon and silicon, and they are unable by themselves to produce Type III inclusions. However, they are able to reinforce and add to the effect of carbon and silicon already present. This is probably responsible for the transformations cited by Sims. Other elements present in commercial melts, such as calcium and chromium, have been



shown by Salter and Pickering<sup>73</sup> to partially replace manganese in some Type III inclusions. Calcium sulfide probably has a higher melting point than MnS and lower solubility in the melt because of its higher free energy of formation, thereby encouraging precipitation of solid sulfide. Type III formation in commercial alloys is seen to be a complex phenomena. However, the principles of microsegregation, activity coefficient changes, and "divorced" eutectic growth developed for here for the carbon and silicon-bearing systems can be successfully extended to understand precipitation in the more complex systems.

#### 6. Type D Inclusions

Type D inclusions are manganese sulfide dendrites which form as a result of the decreasing solubility of manganese and sulfur in the melt along the  $L_m + \text{MnS}$  surface just below the miscibility gap (Figure 9). The dendrites can be very extensive and penetrate through large volumes of the melt (Figure 20b and c). Such large sulfide dendrites have not been reported previously in the literature. They coarsen and become less extensive when held in the  $L_m + \text{MnS}$  region.

When the temperature reaches the eutectic valley after falling along the  $L_m + \text{MnS}$  surface the liquid then contains sufficient manganese and sulfur so that it should solidify as 100% rod eutectic. If the sulfide dendrites are present,

however, only small amounts of the Type II R inclusions are observed to form (Figure 20c). Most of the eutectic sulfide evidently is able to precipitate on preexisting nearby MnS dendrites in a form of "divorced" eutectic solidification. This means that the sulfide dendrites continue to grow for at least a limited distance along the eutectic valley. It also demonstrates that "divorced" or non-cooperative growth of iron and MnS is possible along the line of two-fold saturation (eutectic valley along the Fe-Mn side of the Fe-Mn-S system).

Decreased cooling rates cause the dendrites to coarsen (Figure 16c versus 20c). When significant amounts of carbon or silicon are present this may occur to such an extent even at moderate cooling rates that some attain a chunky and angular morphology similar to Type III inclusions (Figure 25c). Silicon, and especially carbon, allow faceting of the dendrites to occur (Figures 29b and d). Such faceting was not observed in the pure Fe-Mn-S system. In high carbon alloys the faceting is not discernibly affected by variations in cooling rate (Figure 29), but the reverse is true in high silicon melts (Figure 25). Silicon, and especially carbon, strongly reduce sulfur solubility in the melt, causing it to precipitate from a dilute solution. This is believed to be the cause of faceting of the sulfide dendrites in the carbon-rich melts. The weaker effect of silicon on sulfur solubility may be one factor responsible for the cooling rate dependency of faceting in that system.

## B. Fracture

The morphology of some of the inclusions discussed above was revealed by examining the fracture surface of test bars by means of a scanning electron microscope.

Increasing the volume fraction of Type I inclusions caused little change in yield strength, but a large reduction in ductility. The inclusions themselves were revealed to have solidification shrinkage depressions on their surfaces. This is further evidence that they were still liquid slag droplets when entrapped by the iron. Deformation of the metal in the necked region caused a number of them to fracture, demonstrating that deformability of these inclusions is not as high as would be expected from the data of Kiessling<sup>81</sup>. Perhaps a solid solution hardening effect of dissolved oxide is responsible for making these inclusions unexpectedly hard and brittle.

The orientation of cleavage planes of fractured Type II R rods indicates that all the rods in a colony grew from a single nucleus and consist of a single sulfide crystal. This is analogous to the growth of pearlite from single nucleation sites.

## IX. SUMMARY AND CONCLUSIONS

1. Spherical sulfide inclusions result from the presence of oxygen which lowers the melting point of the sulfide so that a slag phase is formed instead of the eutectic which occurs in deoxidized ingots. These inclusions have been designated Type I. They are found between the dendrite arms because they precipitate as a secondary liquid phase in the enriched segregation zones. As a very rough approximation they form when the initial O/S ratio is greater than 0.05, although their appearance is also a function of the overall manganese and sulfur contents.

At higher levels of manganese and sulfur than are found in commercial alloys, a different sort of spherical sulfide inclusion forms. These inclusions result from the intersection of a miscibility gap in the deoxidized Fe-Mn-S system at temperatures above the melting point of iron. They freeze before the iron liquidus is reached and often contain included iron.

If the same high levels of manganese and sulfur are present but deoxidation is not complete the spherical slag inclusions may consist of a duplex MnO-MnS structure and coexist with the eutectic morphologies found in fully deoxidized ingots. Such a situation occurs at O/S ratios in the range of 0.02-0.09. Higher manganese levels require higher O/S ratios for the occurrence of the duplex spherical

sulfides. The particular structures observed are again a complex function of the initial manganese, sulfur, and oxygen levels. Transformations between the different morphologies can be qualitatively understood on the basis of sections of the Fe-Mn-S-O quaternary which have been derived in this research.

2. The formation of rod-like MnS inclusions, designated Type II R, has been explained in terms of the Fe-Mn-S ternary phase diagram. They result from simultaneous solidification of iron and MnS along the line of two-fold saturation near the Fe-Mn binary. They also may form to a limited extent along the line of two-fold saturation on the Fe-FeS side. However, when the composition of the remaining liquid becomes depleted in manganese during solidification the rod morphology becomes degenerate and breaks down into elipsoidal and irregular shapes, and finally into duplex (Fe, Mn)S - FeS sheets designated Type II S. The liquid composition at which the rods become degenerate is uncertain but there is some evidence that this occurs when the segregated liquid reaches the range of 0.75% Mn and 2% S. When the initial manganese content is low enough only the duplex (Fe, Mn)S-FeS and FeS sheets are observed. A unique value cannot be placed on the initial sulfur level and Mn/S ratio which will cause this because the effect of differential segregation of manganese and sulfur must be considered. Nevertheless, it may be stated that when the manganese level is sufficiently low,

solid sulfide does not form until near the ternary eutectic when the sulfur-enriched liquid has assumed the sheetlike form of the interdendritic spaces. This results in the sheetlike Type II S morphology.

3. Angular or faceted sulfides occurring in deoxidized commercial alloys have been designated Type III in the literature and also here. They result from segregation of manganese and sulfur together with elements such as carbon or silicon which decrease sulfur solubility and extend the liquid state to lower temperatures. The inclusions precipitate as a "divorced" eutectic growing in a solution which is relatively dilute with respect to sulfur. They are not the primary phase previous workers had concluded, unless the manganese, sulfur, carbon, and/or silicon levels are well above those usually encountered commercially. Further, they are not the result of strong deoxidation as commonly believed. Deoxidation is a necessary precondition, but Type III inclusions do not form in the pure Fe-Mn-S system, indicating that this is not the only requirement. The other precondition is the presence in the melt of an element such as silicon or carbon which strongly lowers sulfide solubility.

4. A sulfide morphology not previously reported in the literature has been studied. This morphology consists of arrays of crystallographically related platelets and rods, and is designated Type II F. Evidence is presented that it

is an alternate form to Type III, resulting from simultaneous growth of iron and MnS in physical contact as opposed to "divorced" growth of the two phases which leads to Type III. All the factors which favor one growth mode over the other are not fully understood. However, it is shown here that the Type II F morphology is favored over Type III by increasing the cooling rate. Evidence is also presented that Type II F inclusions are a modification of Type II R caused by high carbon or silicon levels which require the sulfide to precipitate from a dilute solution.

5. Limited studies of the Fe-Mn-S and Fe-Mn-S-O phase diagrams have been made. One conclusion which has been drawn is that the miscibility gap on the Fe-FeS side of the phase diagram does not intersect the eutectic valley. This conclusion contradicts the Fe-Mn-S phase diagram frequently presented in the literature.

Qualitative sections of the Fe-Mn-S-O quaternary have been derived and used to rationalize the transition between Type I and Type II inclusions.

6. A few test bars containing the various inclusion morphologies have been fractured and examined with a scanning electron microscope. Some conclusions which are drawn are summarized below.

The effect of inclusion volume fraction and morphology on yield and ultimate tensile strength in the Fe-Mn-S and

Fe-Mn-S-O systems is small. However, elongation and reduction of area are strongly decreased by increasing volume fractions of either Type I or Type II R inclusions. The relative effectiveness of the two morphologies was not studied.

Separation at the inclusion-matrix interface may occur as a result of inclusion shrinkage during solidification, or as a result of different rates of thermal expansion between the matrix and inclusion.

All the rods in a Type II R eutectic colony nucleate and grow from a single source.

During deformation conical voids form on the tensile sides of Type I inclusions. As fracture proceeds these cracks widen, then expand sideways to join voids around other inclusions, forming a propagating fracture surface. Type I inclusions frequently were observed to have fractured during deformation in the necked region.

Fracture in specimens containing Type II R inclusions also tends to follow a path through groups of inclusions. However, propagation across a series of rods is easier than between separated individual Type I inclusions.



## X. SUGGESTIONS FOR FUTURE WORK

1. More quantitative knowledge of the Fe-Mn-S and Fe-Mn-S-O systems would enable quantitative predictions to be made of the transition between Type I and Type II inclusions. This would be useful in reliably controlling properties which depend on sulfide morphology.

2. Growth of the rod eutectic inclusions would be an interesting topic for further study. The manganese composition of the surrounding iron phase is expected to increase as growth of the colony proceeds along the line of two-fold saturation on the Fe-Mn side of the phase diagram. This could be studied with a combined electron microprobe-scanning electron microscope apparatus. The manganese level at which the rods become degenerate on the Fe-FeS side of the diagram could also be established by such an apparatus.

3. The factors, other than cooling rate, which control the Type III-Type II R and Type III-Type II F transitions are a possible subject for additional study. If the sulfide can be made to grow as Type III instead of as Type II, deoxidized alloys of improved impact properties can be obtained.

BIBLIOGRAPHY

1. R. Kiessling and N. Lange, Non-Metallic Inclusions in Steel, Iron and Steel Institute, Special Reports No. 90 (1964), No. 100 (1966), and No. 115 (1968).
2. C.E. Sims and G.A. Lillieqvist, Trans. AIME, (1932), 100, 154.
3. C. Benedicks and H. Lofquist, Non-Metallic Inclusions in Iron and Steel, (1930), Chapman and Hall, London.
4. B.F. Comstock, Iron Age, (Dec. 4, 1924), p. 1477.
5. C.E. Sims and F.B. Dahle, Trans. Amer. Foundrymen's Association, (1938), 46, 65-104.
6. S. Urban and J. Chipman, Trans. ASM (1935), p. 645-671.
7. A. Gagnebin, Trans. Amer. Foundrymen's Association, (1938), 46, 133-155.
8. W. Crafts, J. Egan and W. Forngeng, Trans. AIME, (1940), 140, 233.
9. C.E. Sims, H. Saller and F. Boulger, Trans. Am. Foundry Soc., (1949), 57, 233.
10. C.E. Sims, H. Saller and F. Boulger, Trans. AIME, (1949), 185, 814.
11. C.E. Sims, AIME Elec. Furn. Proc., (1952), vol. 10, pp. 152-171.
12. W. Crafts and D. Hilty, AIME Elec. Furn. Proc., (1953), vol. 11, pp. 121-150.
13. C.E. Sims, Trans. AIME (1959), 215, pp. 367-393.
14. C.E. Sims and C. Briggs, AIME Elec. Furn. Proc., (1959), vol. 17, pp. 104-124.
15. W.J. Lichy, G.C. Duderstadt and N.J. Samways, Journal of Metals, (1965), vol. 17, no. 7, pp. 769-775.
16. H. Hirai, T. Araki, S. Matsukuma and Y. Kojima, Tetsu To Hagane, (1965), vol. 15, no. 4, pp. 816-819. (Brutcher Translation H.B. No. 6695).

17. W. Dahl, H. Hengstenberg and C. Düren, Stahl und Eisen. (1966), vol. 86, no. 13, pp. 782-795. (Brutcher Translation H.B. No. 6928).
18. J. Beech, B.A. Hands and P.P. Mohla, Metallurgia, (1967), 76, pp. 175-179.
19. P.P. Mohla and J. Beech, The British Foundryman (Dec. 1968), pp. 453-460.
20. P.P. Mohla and J. Beech, Jour. of the Iron and Steel Institute, (Feb. 1969), pp. 177-180.
21. C.A. Duckwitz, E. Forster, H. Richter, Archiv Eisenhuttenwesen, (1968), vol. 39, no. 5, pp. 333-338.
22. T.Z. Kattamis and M.C. Flemings, Army Materials and Mechanics Research Center, Contract No. DA-19-020-AMC-5443 (X), Final Report for October 1966-December 1967.
23. O. Meyer and F. Schulte, Archiv Eisenhuttenwesen, (1934-1935), pp. 187-195.
24. F. Körber and W. Oelsen, Stahl und Eisen (1936), 56, pp. 441-444.
25. H. Wentrup, Technische Mittelungen Krupp, (1937), 5, pp. 131-152.
26. R. Vogel and W. Hotop, Archiv Eisenhuttenwesen, (1937), vol. 11, pp. 41-54. (Brutcher Translation H.B. No. 459).
27. E. Schurmann, Giesserei, (1961), 48, pp. 481-487.
28. D.C. Hilty and W. Crafts, Trans. AIME, (1952), 196, p. 1307.
29. D.C. Hilty and W. Crafts, Trans. AIME, (1954), 200, pp. 959-968.
30. E. Schurmann and I.O. von Hertwig, Giesserei Techn.-Wiss. Beihefte, (1962), 14, no. 1, pp. 31-36.
31. J. Yarwood, Massachusetts Institute of Technology, Metallurgy Department, Ph.D. thesis (1968), p. 71.
32. H.C. Chao, Y.E. Smith and L.H. Van Vlack, Trans. AIME, (1963), 227, p. 796.

33. R. Vogel, C. Uschinski and U. Theune, Archiv Eisenhuttenwesen, (1941), 14, pp. 455-462.
34. E. Schurmann and I.O. von Hertwig, Giesserei Techn.-Wiss. Beihefte, (1962), 14, no. 2, pp. 63-70.
35. A. Norro and S. Lundquist, Jernknotorets Annaler, (1946), vol. 130, no. 3, pp. 118-126. (Brutcher Translation H.B. No. 1833).
36. R. Vogel and F. Hillen, Archiv Eisenhuttenwesen, (1942), 15, pp. 551-555.
37. J.P. Morris and R.C. Buehl, Trans. AIME, (1950), 188, pp. 317-322.
38. J.P. Morris and A.J. Williams, Trans. Amer. Soc. for Metals, (1949), 41, pp. 1425-1439.
39. J.P. Morris and R.C. Buehl, Trans. AIME, (1950), 188, p. 1349.
40. D.C. Hilty and W. Crafts, Trans. AIME, (1950), 188, pp. 425-436.
41. D.C. Hilty and W. Crafts, Trans. AIME, (1950), 188, pp. 1346-1347.
42. D.C. Hilty, Jour. of Metals, (1966), 18, pp. 201-204.
43. D.C. Hilty and W. Crafts, Trans. AIME, (1950), 188, pp. 414-424.
44. J.R. Brown, Jour. of the Iron and Steel Institute, (1967), 205, pp. 154-157.
45. C.W. Sherman, H.I. Elvander and J. Chipman, Trans. AIME, (1950), 188, pp. 334-340.
46. J. Chipman, J.B. Gero and T.B. Winkler, Trans. AIME, (1950), 188, pp. 341-345.
47. F. Körber and W. Oelsen, Mitt. Kais. Wilhelm Inst., Eisenforsch., Dusseldorf (1932), 14, 181.
48. A.U. Seybolt, Trans. AIME (1954), 200, pp. 641-644.
49. A.U. Seybolt, Trans. AIME (1954), 200, pp. 979-982.

50. E.T. Turkdogan, S. Ignatowicz, and J. Pearson, Jour. of the Iron and Steel Institute, (1955), 180, pp. 349-354.
51. N.G. Ainslie and A.U. Seybolt, Jour. of the Iron and Steel Institute, (1960), 194, pp. 341-350.
52. N.G. Ainslie, R.E. Hoffman and A.U. Seybolt, Arca Metallurgica, (1960), vol. 8, pp. 523-527.
53. N.G. Ainslie, V.A. Phillips and D. Turnbull, ibid., pp. 528-538.
54. I.S. Brammer and R.W.K. Honeycombe, Jour. of the Iron and Steel Institute, (April 1964), pp. 335-342.
55. J.D. Baird and J.M. Arrowsmith, Jour. of the Iron and Steel Institute, (March 1966), pp. 240-247.
56. E.J. Paliwoda, Trans. ASM, (1955), vol. 47, pp. 681-691.
57. R.B.G. Yeo, Journal of Metals, (June 1967), pp. 29-32.
58. R.B.G. Yeo, Journal of Metals, (July 1967), pp. 23-27.
59. L.H. Van Vlack, Trans. AIME, (1951), 191, pp. 251-259.
60. A.S. Keh and L.H. Van Vlack, Trans. AIME, (1956), 206, pp. 950-958.
61. L.H. Van Vlack, O.K. Riegger, R.J. Warrick and J.M. Dahl, Trans. AIME, (1961), 221, pp. 220-228.
62. T.L. Joseph and W.F. Holbrook, Bureau of Mines, RI3240, (1934).
63. I.S. Brammer and R.W.K. Honeycombe, Jour. of the Iron and Steel Institute, (1962), 200, pp. 1060-1067.
64. R. Kiessling and C. Westman, Jour. of the Iron and Steel Institute, (1966), 204, pp. 377-379.
65. M. Hansen, Constitution of Binary Alloys, (1958), McGraw-Hill, New York.
66. Z. Shibata, Sci. Rep. Tohoku University, (1928), vol. 7, pp. 279-289.
67. F.N. Rhines, Phase Diagrams in Metallurgy, (1956), pp. 178, 207, McGraw Hill, New York.

68. H. Wentrup, Carnegie Scholarship Mem., (1935), 24, p. 118.
69. C.W. Sherman and J. Chipman, Trans. AIME, (1952), 194, pp. 597-602.
70. T. Rosenqvist and B.L. Dunicz, Trans. AIME, (1952), 194, pp. 604-608.
71. H. Hanemann and A. Schildkotter, Archiv Eisenhüttenwesen, (1929-1930), vol. 3, No. 6, pp. 427-435.
72. R. Vogel and G. Ritzau, Archiv Eisenhüttenwesen, (1931), vol. 4, No. 11, pp. 549-556.
73. W.J.M. Salter and F.B. Pickering, Jour. of the Iron and Steel Institute, (1969), 207, pp. 992-1002.
74. O. Repetylo, M. Olette, and P. Kozakevitch, Journal of Metals, (May 1967), pp. 45-49.
75. M.C. Flemings, Trans. AFS, (1964), 72, pp. 353-362.
76. M.C. Flemings, The Solidification of Metals, Jour. of the Iron and Steel Institute, Publication 110, (1968), pp. 277-288.
77. C.J. Smithells, Metals Reference Book, (1962), Butterworth Inc., Washington, D.C.
78. W.A. Miller and G.A. Chadwick, The Solidification of Metals, Jour. of the Iron and Steel Institute, Publication 110, (1968), pp. 49-56.
79. D. Saratovkin, Dendrite Crystallization, translated by Consultants Bureau, Inc., New York (1959).
80. T.Z. Kattamis, J.M. Coughlin, and M.C. Flemings, Trans. Met. Soc., AIME, (1967), vol. 239, pp. 1504-1511.
81. R. Kiessling, Journal of Metals, (October 1969), pp. 48-54.
82. K.A. Jackson and J.D. Hunt, Acta Metallurgica, (1965), 13, pp. 1212-1215.
83. J.W. Cahn, Acta Metallurgica, (1960), 8, pp. 554-562.
84. R. Mehrabian and M.C. Flemings, accepted for publication in Trans. Met. Soc. AIME.

85. J.F. Elliot, *Le Vide*, No. 135 (Mai-Juin 1968), pp. 123-150.
86. T.Z. Kattamis and M.C. Flemings, *Trans. Met. Soc. AIME*, (November 1966), vol. 236, pp. 1523-1532.

## APPENDIX A

### Experiments on Fe-Mn-S Ternary

#### Experimental Techniques

Experimental techniques were identical to those described in Chapter V since the same alloys which were used for the morphology studies were also deemed applicable for use in this discussion of the Fe-Mn-S ternary.

As was pointed out in Chapter V the inherent limitation on the accuracy of the two-pen recorder used in these experiments is about  $\pm 5^{\circ}\text{C}$  because of the factor of ink-line width alone. However, it was also pointed out that the actual voltage put out by the thermocouple usually lay within the width of the line. Other factors such as thermal lag in steep temperature gradients during rapid temperature changes can probably account for an error of  $\pm 10^{\circ}\text{C}$  in some rapidly cooled specimens in the present series of experiments.

No difference was found in the liquidus temperature at a level of 1% sulfur when melting was done in a silicon rather than an alumina crucible. Alloy 5-3, a 1% sulfur alloy melted in alumina and Alloy 4-3, a 1% sulfur alloy melted in silicon, solidified at  $1500^{\circ}\text{C}$  and  $1496^{\circ}\text{C}$  respectively. These are within the limits of the accuracy of the temperature recorder. Furthermore, they agree within the limits of reading accuracy of the diagram with Hansen's<sup>65</sup>



value for the liquidus temperature at this composition. The liquidus temperatures of Alloy 4-2 (0.1% S) and Alloy 4-4 (11% S) are 1524°C and 1380°C respectively. These values are also in close agreement with Hansen's phase diagram.

### Results

The liquidus temperatures of interest are listed in Table A-1, along with the alloy number and composition. The data are presented graphically in Figure A-1. The alloys of series 4 were melted in silica crucibles, while those in series 5 were melted in alumina crucibles.

### Discussion

The results of the present research are presented in Figure A-1. A few isotherms of the liquidus are drawn. These are based upon a limited number of data points, but they do clearly show the expected tendency of the eutectic temperature to drop much more rapidly on the Fe-S side than on the Fe-Mn side. The 1490°C isotherm on the Fe-Mn side is speculative, except that it must intersect the Fe-Mn binary about 10% Mn. The alloys 5-30, 8-23, 8-7, 8-13, 8-11, 8-5, and 29-2 are in the miscibility gap at the quench temperature of 1650°C, as is evidenced by the formation of slag on the surface of the ingot and entrapped in the melt. No slag is found near the surface of specimen 8-10, indicating that it lies just outside of the miscibility gap. Freezing of the slag which formed on 5-30, 8-23, 8-7, 8-13, 8-11,

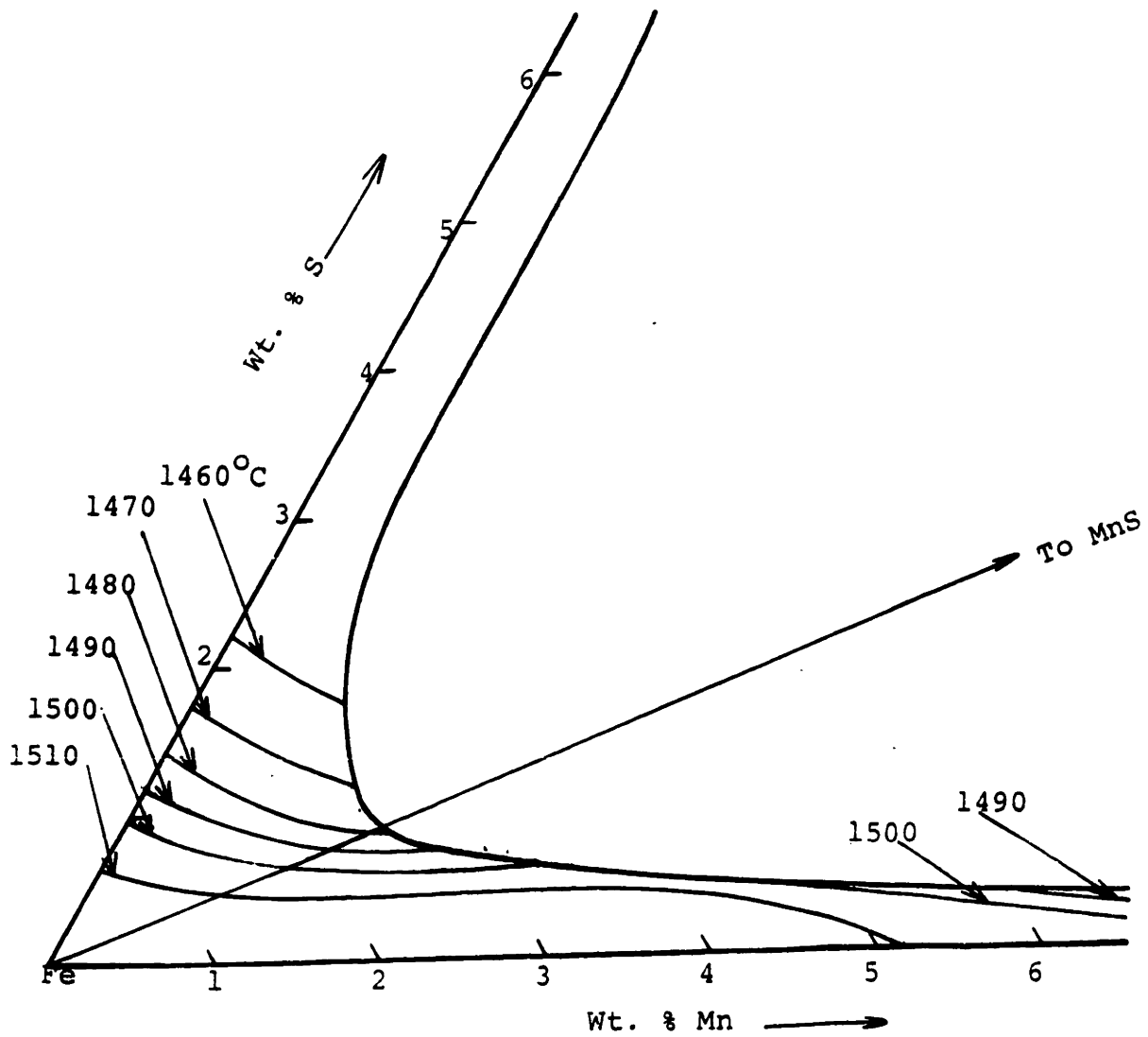


Figure A-1: Liquidus isotherms and eutectic plotted from data in Table A-1.

29-2, and 8-5 is not detectable by the temperature recorder because of the small amount present.

Examination of Table A-1 will show that the alloys contain up to 0.07% oxygen. It is to be emphasized that the specimens used were part of a series intended to show the effects of various oxygen-sulfur ratios on sulfide morphology. Other specimens with higher oxygen contents have been eliminated from consideration here. Examination of the known phase diagrams for Fe-O show that an oxygen level of 0.07% can cause a maximum reduction of about 5°C in the freezing temperature. The small amounts of carbon used for a vacuum carbon boil in some specimens may have a similar effect. However, comparison of 8-13 (Al-deoxidized) with 29-3 (carbon deoxidized) shows that this effect cannot be very large. The following statements can be made:

- 1) Depression of the freezing point by oxygen and carbon in the alloys used in this study is less than the error in measurement;
- 2) Data generated at compositions previously studied by other researchers is in agreement with published results;
- 3) Data generated at new compositions varies in an expected manner and with a magnitude greater than the experimental error. Therefore, the results reported in Table A-1 and Figure A-1 are significant and valid.

In summary, it may be concluded that the eutectic valley reaches a maximum in the iron corner of approximately 1510°C

at a composition near 3% Mn and 0.50% S. From this point it falls quite rapidly toward the Fe-FeS side, while remaining on a fairly level plateau to at least the 5% Mn level on the Fe-Mn side.

TABLE A-1.  
Liquidus temperature as a function of composition

Specimen #	Liquidus Temperature (°C)	Composition (Wt. %)		
		Mn	S	O
5-20	1523	-	0.12 (nom. *)	-
29-1	1511	3.22	0.40	-
29-2	1509	3.72	0.45	-
5-3	1500	-	1.00 (nom.)	-
8-13	1498	3.18	0.82	0.0016
29-3	1496	3.64	0.77	0.0018
4-3	1496	-	1.00 (nom.)	-
8-7	1494	2.03	0.78	0.005
8-8	1490	2.76	1.18	0.013
8-5	1490	4.90	1.01	0.0029
5-26	1486	1.30	0.78	0.06
5-27	1481	0.02	1.41	0.043
5-30	1480	1.42	0.87	0.029
5-31	1478	1.5 (nom.)	0.9 (nom.)	0.03 (nom.)
5-29	1468	0.32	1.63	0.069
5-28	1466	0.56	1.56	0.033

\* Nom. = Nominal percentage of added component.

## APPENDIX B

### The Fe-Mn-O-S System

Very little quantitative data is known on the Fe-Mn-O-S system. Hilty and Crafts<sup>29</sup> speculated on the probable features of the system, based upon expected modifications of the associated ternaries. Experimental results in one part of the system corresponded to their expectations.

### Representation of Four Component Systems

Before discussing their diagram and data further it is appropriate to consider how such a system could be represented. The Fe-Mn-O-S system could be completely described as an infinite series of isothermal quaternary tetrahedra at infinitesimal temperature differentials. Each tetrahedron would describe the phase relations and tie-lines at one temperature only. A shorter series of such tetrahedra at reasonable temperature intervals would suffice for practical purposes. Each face of these tetrahedra would represent an isothermal cut of one of the pure ternary systems; Fe-O-S, Fe-Mn-S, Mn-O-S, Fe-Mn-O. Figure B-1 is a qualitative example of how such a diagram would look for the Fe-Mn-O-S system at 1600°C. Details of the Fe-Mn-O and Mn-O-S faces, which represent isothermal sections through the respective ternaries, have not been shown in order to avoid cluttering the diagram. Modification of the miscibility gaps and other features on the faces by the fourth component determines how the boundary lines and surfaces intersect in the

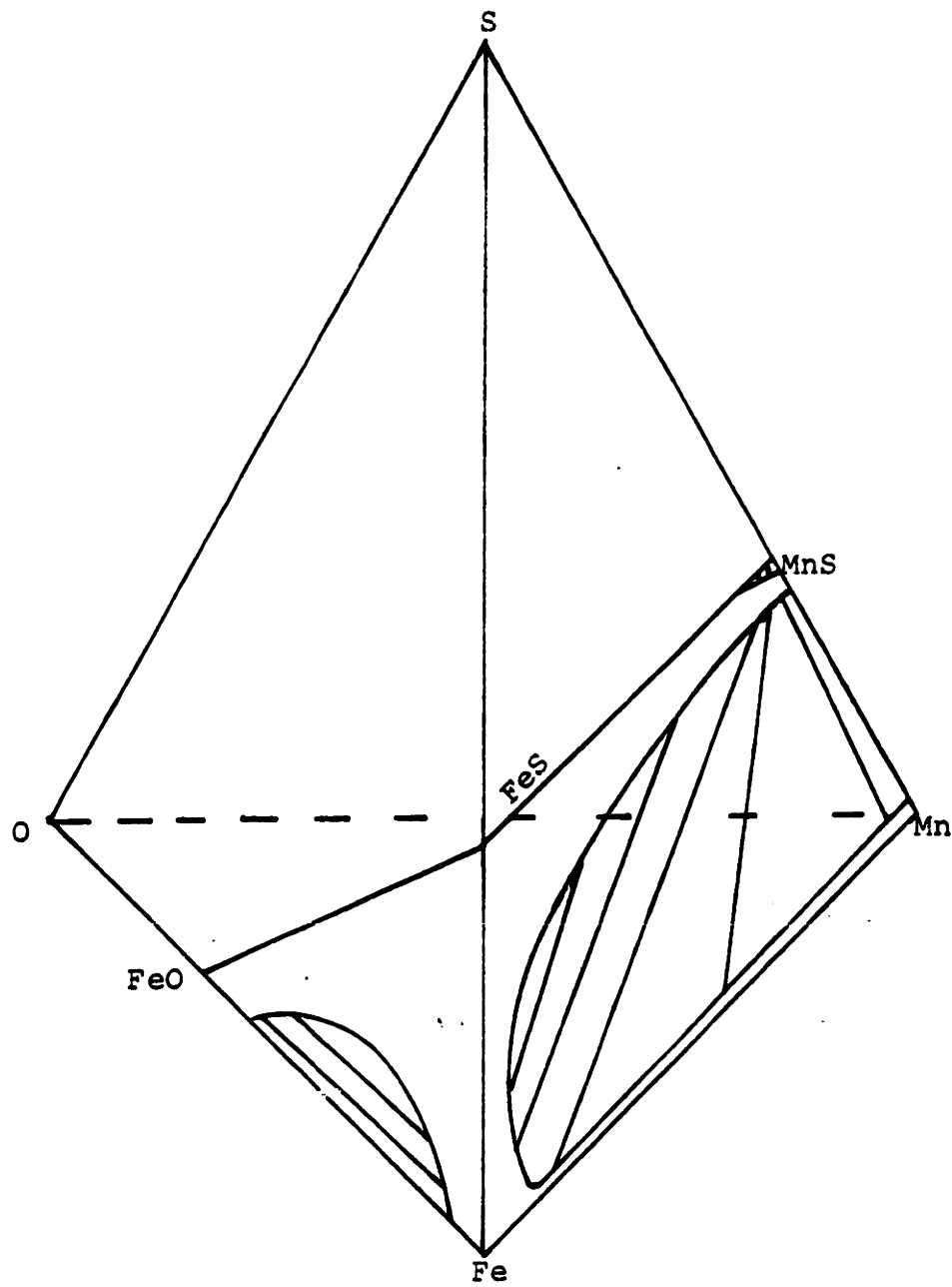


Figure B-1: Fe-Mn-O-S Phase Diagram for 1600°C. Intersection with miscibility gaps in Fe-O-S and Fe-Mn-S systems are shown, along with a few tie-lines. Intersection with Mn-S-O and Fe-Mn-O systems are not shown.

interior of the tetrahedron, and fixes the direction of the tie-lines. A true definition of the system requires experimental data, but a qualitatively correct visualization of the interior of these isothermal tetrahedra can be arrived at using known principles for phase diagram construction, such as the phase rule.

The method just discussed can be used to completely describe a quaternary system. However, this is extremely difficult to represent in either two or three dimensions, and is equally difficult to visualize clearly for practical applications. If the composition of one component is held constant, a somewhat more useful representation of the system can be constructed which makes it easier to visualize the effect of temperature on the phase relations. To determine the phase boundaries in a system containing, for example, 1% manganese, one could proceed as follows. For each temperature of interest an isopleth\* at 1% Mn is taken by sectioning the corresponding isothermal tetrahedron. The intersection of the internal phase boundaries with the isopleth traces the limits of the various phases in terms of the Fe/S/O composition ratio at 1% Mn and the chosen temperature. A series of such isopleths stacked up on a temperature axis erected from the lowest temperature isopleth, generates a pseudo-ternary which shows coexistence regions for the various phases for 1% Mn alloys. Visual-

---

\* Isopleths are planes parallel to one of the faces of the quaternary tetrahedron, and represent constant percentage of one component.

ization of such a construction will be aided by reference to Rhines<sup>67</sup>, p. 231. Such diagrams differ from true ternaries in several ways. Tie-lines cannot be drawn since the diagram makes no provision for representing manganese contents other than the overall value, e.g., 1%. The manganese content of the individual phases, however, is not restricted to 1%. This derives from the fact that the isopleths cut through tie-lines in the original isothermal quaternary tetrahedra which may connect phases with manganese contents lying outside the 1% Mn plane. A pseudo-ternary constructed in this manner can be used to determine which phases coexist at a certain temperature with a particular ratio of Fe/S/O and 1% manganese, but it cannot give any information on the composition of the phases. A true ternary or quaternary could include tie-lines giving such information. Another important difference between the pseudo-ternary representation and true ternaries is that four phases may coexist over a range of temperatures, not just on an isothermal four-phase plane. This derives from the fact that the pseudo-ternary actually represents a four-component system, even though only three are made explicit on the base isopleth.

The 1% manganese composition used above was chosen simply for the sake of discussion. At different manganese contents the isopleths would intersect the internal boundaries of the isothermal quaternaries in different places and therefore would generate a different pseudo-ternary diagram.



Caution should therefore be used in generalizing from one manganese level to another. Another consideration is that non-equilibrium solidification may segregate the manganese in such a way as to change the phase diagram applicable to the remaining liquid.

#### Application to Fe-Mn-O-S System

The ternary diagrams associated with this system are only qualitatively determined for the most part, so that application of the principles described above can only lead to a general discussion of the phase relations. Nevertheless, such a discussion can provide an understanding of the system which is of technical importance.

It is possible to work with the ternary diagrams to construct the sides of the pseudo-ternary and then try to connect the boundary phases which result. This is equivalent to the method of sectioning quaternaries. Since the quaternaries of the Fe-Mn-O-S system have not been constructed, it is also simpler. Bisecting the Fe-Mn-S ternary at a particular level of Mn will generate the metal-sulfide temperature face of the pseudo-ternary of interest. Similarly, the metal-oxide-temperature face of the pseudo-ternary can be deduced by intersecting the Fe-Mn-O ternary with a plane of constant manganese content. The sulfide-oxide-temperature face is determined by an intersection with the Mn-O-S ternary.

We will first consider how the isopleths of the Fe-Mn-S system change with increasing manganese content. At zero percent manganese, the diagram is the simple Fe-FeS binary. Very close to the Fe-FeS face, at lower manganese contents than the ternary eutectic, iron and iron sulfide will continue to be the primary phases above the eutectic temperature. Manganese is slightly soluble in FeS, so we would expect there to be a narrow two phase region in which FeS containing some manganese can coexist with iron. Since experimental evidence indicates that the ternary eutectic lies at the binary eutectic, such a region can only exist at low manganese levels. Figure B-2 shows what happens when the overall manganese content is increased to about 0.2%, which is probably higher than the ternary eutectic but is still less than enough to intersect the miscibility gap. A manganese sulfide phase containing considerable iron, hereafter referred to as the Q-phase, now becomes primary in a composition region near the eutectic. Schurmann's<sup>27</sup> assumption of the existence of a four-phase plane would not affect this diagram since the manganese level is too low to intersect such a plane. If the manganese content is increased to about 1%, the miscibility gap will be intersected, as shown in Figure B-3. Another change is that high-melting Q-phase can now form as the primary phase in the iron corner. A large region exists where iron-rich liquid can reject iron

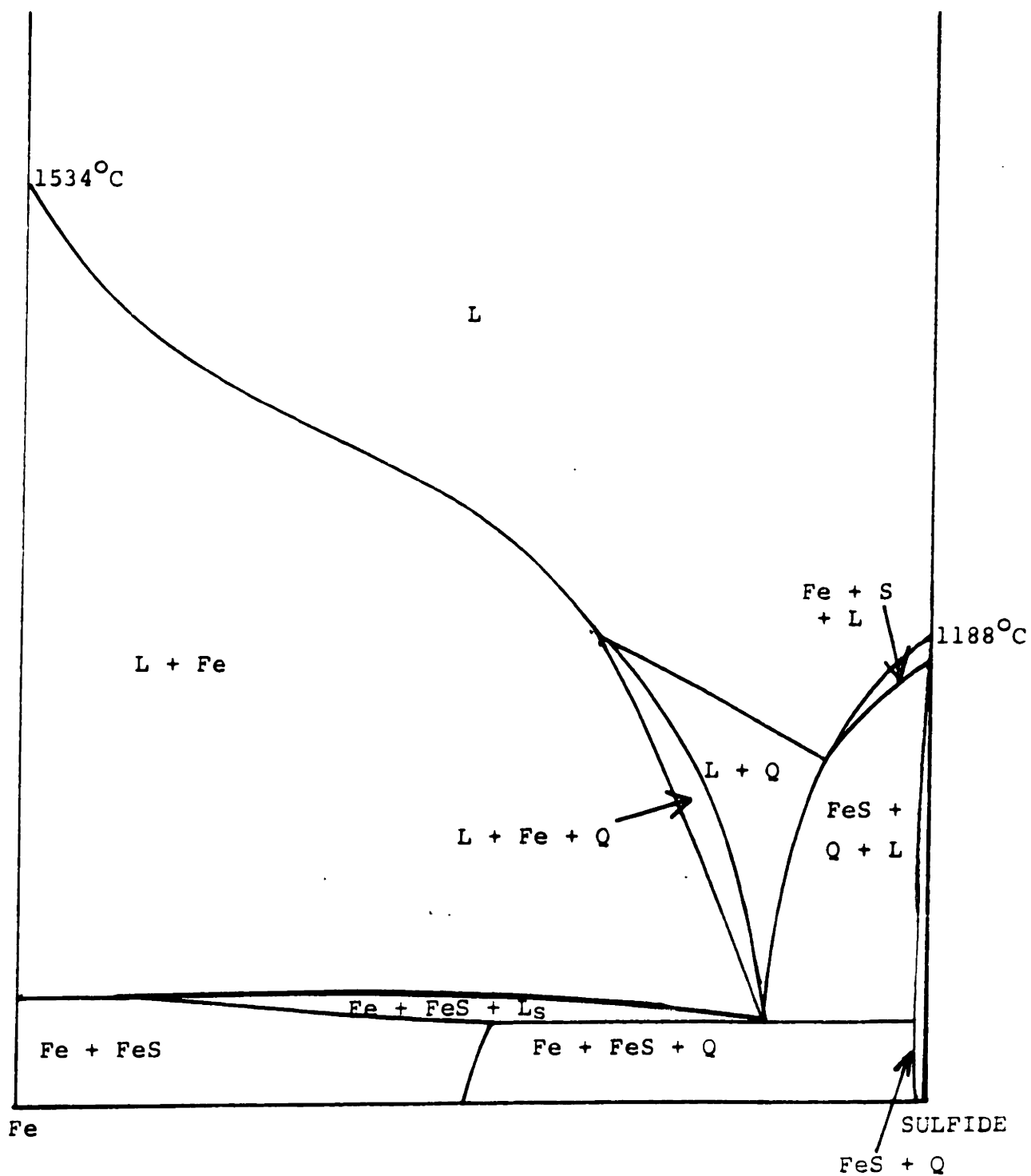


Figure B-2: Qualitative isopleth of the Fe-Mn-S system at 0.2% Mn.

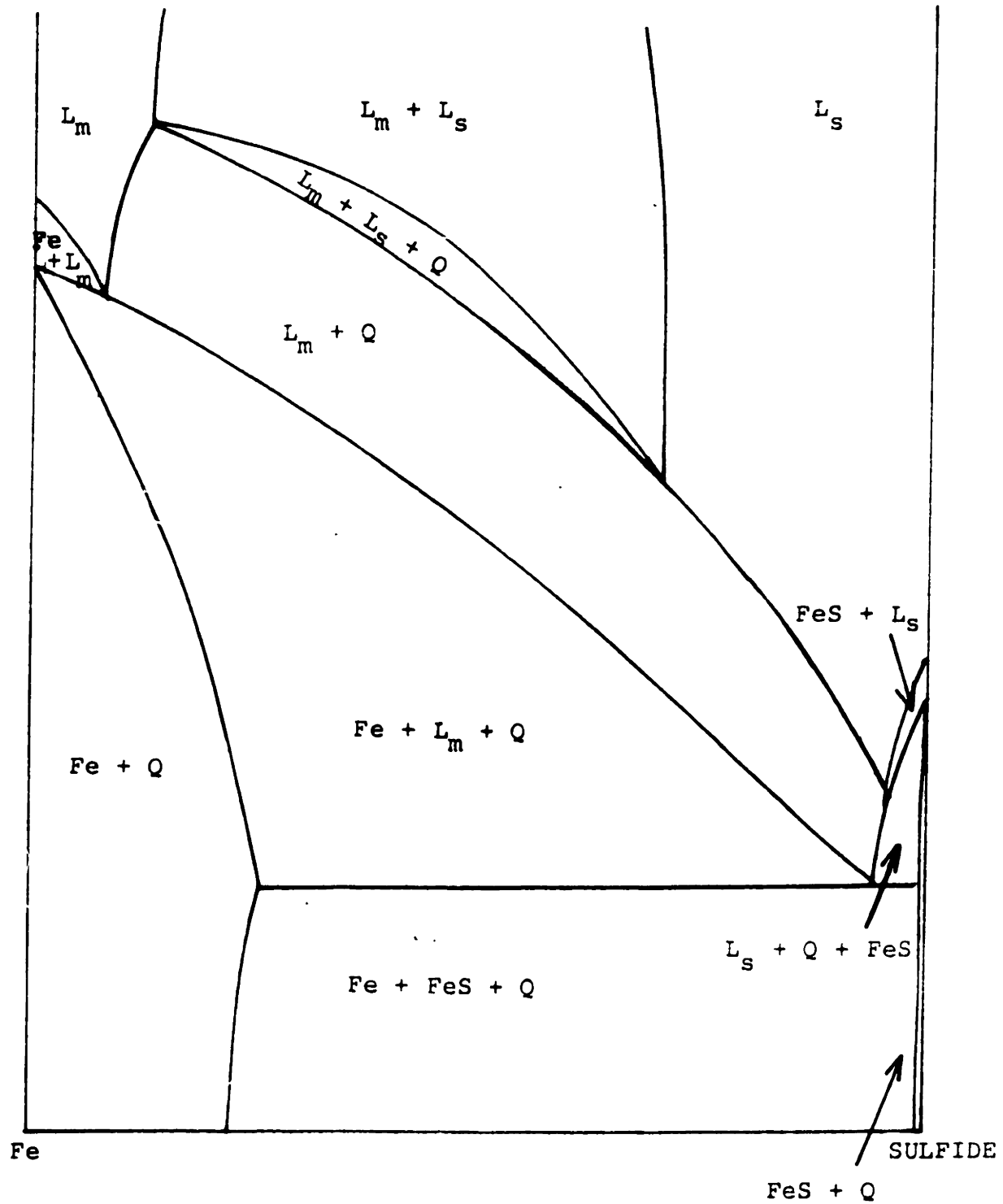


Figure B-3: Qualitative isopleth of Fe-Mn-S system at 1% Mn.

and Q-phase over a temperature range as a eutectic. Of course if such a process occurs under non-equilibrium conditions, the overall composition of the remaining liquid will change, and will no longer be in equilibrium with the phases as represented by this isopleth. However, the general features will remain constant over a reasonable range of manganese content. It may be noted that Vogel's determination of the 97 Fe/3 Mn plane looks very similar to Figure B-3, as would be expected since the planes are nearly parallel in the ternary. If Wentrup's version of the Fe-Mn-S diagram is valid, the 1% Mn isopleth will appear as shown in Figure B-4. The four-phase plane has been assumed to lie at 1420°C. It may be seen that at this temperature the eutectic formation  $Fe + Q + L_M$  changes to an equilibrium between  $Fe + L_M + L_S$  (slag). This indicates that under equilibrium conditions the sulfide phase will remelt and be replaced by slag. At lower sulfur levels (higher Mn/S ratios) the Q phase does not disappear, but instead the metal-rich liquid is replaced by slag ( $Fe + Q + L_M \rightarrow Fe + Q + L_S$ ). This model of the Fe-Mn-S ternary has been investigated elsewhere in this research and has been found to be wrong.

The effect of increasing manganese content on the metal-oxide-temperature face of the pseudo-ternary is to increase the melting point of the oxide phase. With no manganese present, the Fe-FeO binary is applicable. With a

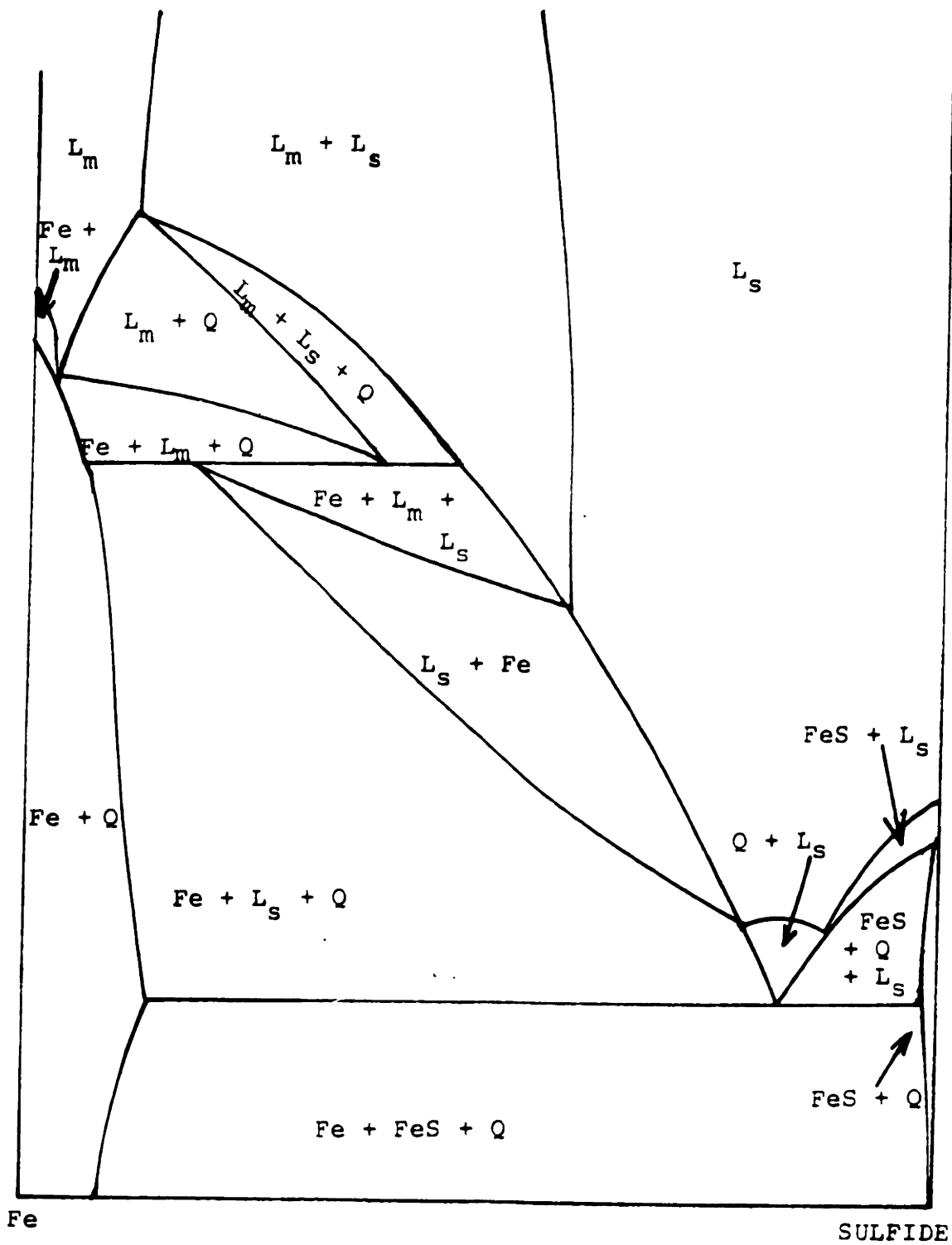


Figure B-4: Qualitative isopleth through the Fe-Mn-S system showing the four-phase plane according to Wentrup's model. Composition: approximately 1% Mn.

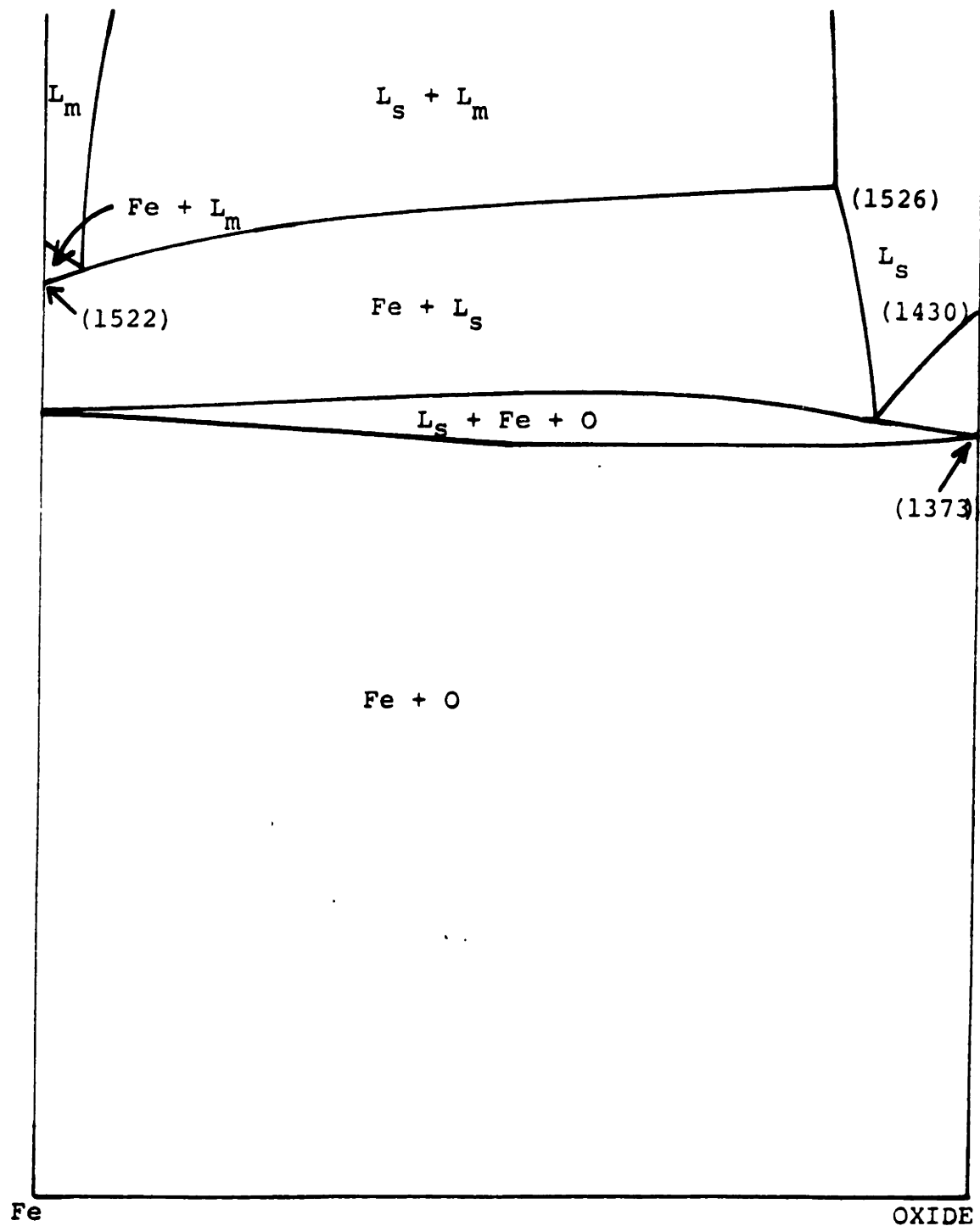


Figure B-5: Qualitative isopleth through Fe-Mn-O system at a level of 0.2% Mn, believed to be less than needed to intersect the four-phase plane. Bracketed temperatures are given to show relative values, and are not quantitatively accurate.

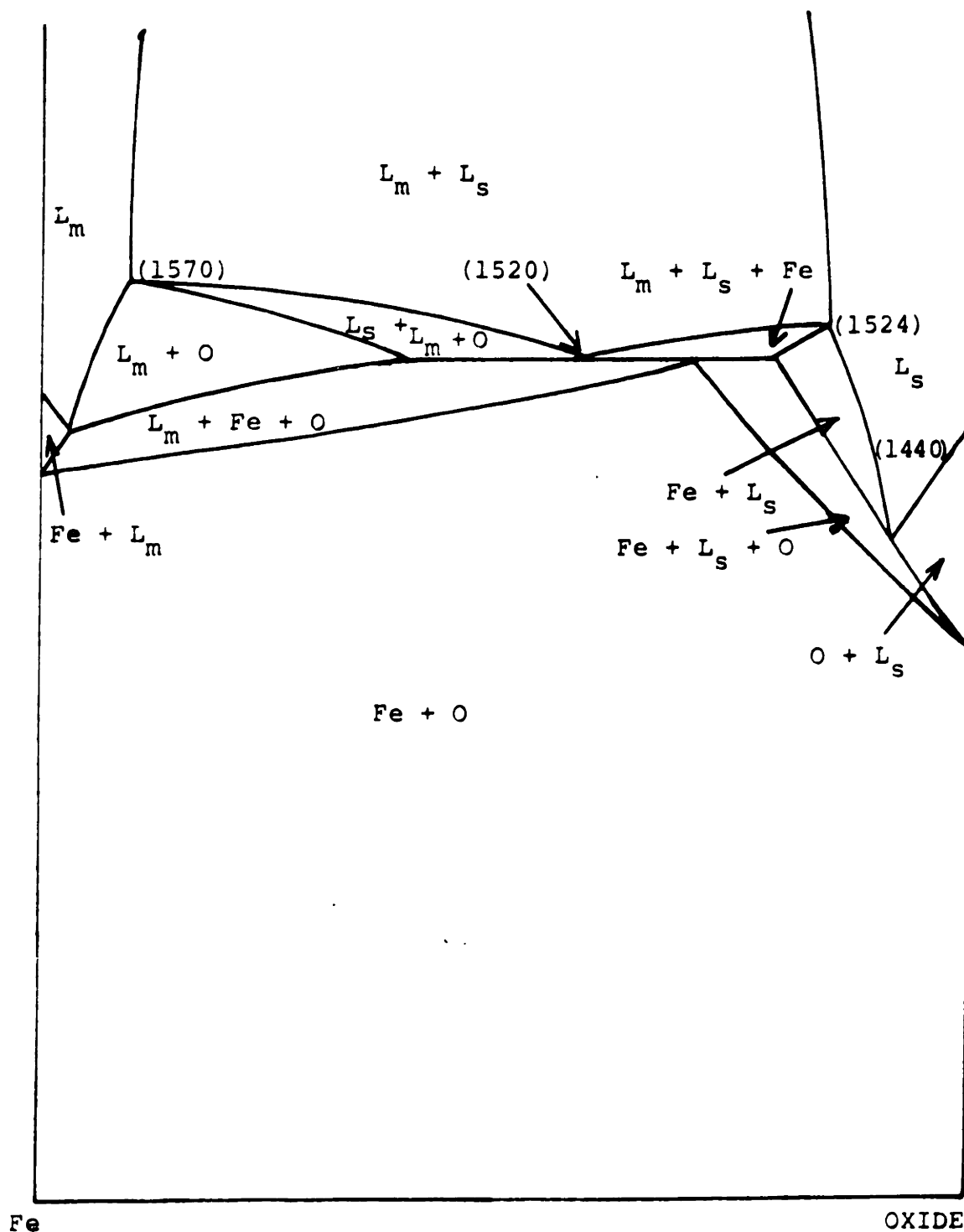


Figure B-6: Qualitative isopleth of the Fe-Mn-O ternary at 1% Mn, showing four-phase plane and approximate temperatures in brackets.



four-phase plane until the manganese level reaches about 20%. However, tie-lines running across the phase diagram from the iron corner connect with high melting oxide at much lower manganese levels.

The oxide and sulfide side of the pseudo-ternary is determined on each edge by its intersection with the other two isopleths. The FeS-FeO and MnS-MnO binaries form simple eutectics, so it seems reasonable to expect that oxide and sulfide phases containing 1% Mn should also do so. Wentrup concluded that a eutectic on the FeO-FeS-MnS-MnO face of the quaternaries should be found about  $910^{\circ}\text{C}$ , approximately in the middle of the FeO-FeS half of the trapezoid. This eutectic would be expected to extend somewhat into quaternary space at a slightly lower temperature to form a quaternary eutectic. An examination of the relevant quaternaries indicates that the five-phase plane of the quaternary eutectic is not intersected by the 1% Mn isopleth. Higher manganese contents created by segregation in the liquid may lead to the formation of small amounts of the quaternary eutectic, but this does not seem likely to be of practical significance. Therefore, this part of the quaternaries and associated pseudo-ternaries has not been investigated in detail.

The significance of the isopleths which have been constructed is that when they are put together to form a pseudo-ternary of an alloy containing a fixed amount of manganese

they can give a picture of the way different O/S ratios can determine which phase will be primary, and at which temperature it should form. An isopleth of the quaternary tetrahedron at the same temperature can also be used to obtain a picture of the way the various phase fields interact as the O/S ratio is varied. Neither construction can give the actual composition of the phases and the tie-lines.

A qualitative 1% Mn isopleth of the 1475°C quaternary is presented in Figure 7. This shows that when the O/S ratio reaches a certain value a four-phase region is entered and slag can form. The necessary ratio is lower when the actual sulfur content increases, as might occur during non-equilibrium solidification. Hilty and Crafts<sup>29</sup> made an experimental determination of this particular isopleth. They found an O/S ratio of about 1/10 in slag from one specimen which had entered the four-phase region. They also observed the three-phase region in the middle of the diagram, and the four-phase region on the oxide side.

The phase diagram section presented in Figure 7 is considerably enlarged and exaggerated in the iron corner. Actually, the four-phase region can be entered at quite low values of O and S, early in solidification. The features of the diagram, which was derived by sectioning a 1475°C quaternary at 1% Mn, may be confirmed by sectioning at 1475°C a 1% Mn pseudo-ternary. The operations

are equivalent. It may be noted that the slag phase extends completely across the oxide-sulfide sides of the diagram, whereas Hilty and Crafts presented a qualitative section in which primary oxide and sulfide could be found in this region. In actuality, any oxide and sulfide phases which could form there would be forming from a melt containing only about 1% Mn. Figures B-3 and B-6 show that they would be above their melting points at 1475°C. Nevertheless, the important conclusion of this discussion is supported by Hilty and Crafts' diagram and experimental results. This is that at relatively low oxygen levels a slag phase can form where, in the absence of oxygen, a eutectic would form.

APPENDIX C

The iron used in this study was Ferrovac-E iron supplied in the form of half-inch rods. The lot analysis is given in Table C-1.

TABLE C-1

## Lot Analysis of Ferrovac-E Iron

	wt. pct.		wt. pct.
C:	0.005 - 0.01	N:	0.0002 - 0.00085
Co:	0.0006 - 0.005	Ni:	0.02 - 0.02
Cr:	0.006 - 0.01	O:	0.0002 - 0.003
Cu:	0.006 - 0.01	P:	0.002 - 0.003
Mn:	0.0005 - 0.001	S:	0.003 - 0.005
Mo:	0.001 - 0.01	Si:	0.006 - 0.006

BIOGRAPHICAL NOTE

The author was born in St. Thomas, Virgin Islands on February 22, 1941. He lived in the British Virgin Islands until 1955, when he entered Brooks School in Massachusetts. He received a Bachelor of Arts degree from Harvard College in 1962 and a Bachelor of Science degree from the same college in 1964. He worked for one year at General Dynamics/Convair in San Diego, California. The author then entered the Graduate School of the Massachusetts Institute of Technology in September, 1965, as a candidate for the degree of Doctor of Science in Metallurgy with a minor in Industrial Management.

The author is a member of the American Society for Metals, and the American Institute of Mining, Metallurgical, and Petroleum Engineers, Inc.

END OF FILM

PLEASE REWIND







